

Modeling Multiphase Flow in Porous Medium Systems at Multiple Scales

by

Huina Li

A dissertation submitted to the faculty of the University of North Carolina at Chapel Hill in partial fulfillment of the requirements for the degree of Doctor of Philosophy in the Department of Environmental Sciences & Engineering.

Chapel Hill

2006

Approved:

Prof. Cass T. Miller, Advisor

Prof. Matthew W. Farthing, Reader

Prof. Marc L. Serre, Reader

Prof. Jingfang Huang, Reader

Prof. Richard L. Smith, Reader

©2006
Huina Li
ALL RIGHTS RESERVED

ABSTRACT

HUINA LI: Modeling Multiphase Flow in Porous Medium Systems at Multiple Scales
(Under the Direction of Cass T. Miller)

Problems involving multiphase flow and transport in porous media arise in a number of scientific and engineering applications including oil reservoir engineering and groundwater remediation. The inherent complexity of multiphase systems and the marked heterogeneity over multiple spatial scales result in significant challenges to the fundamental understanding of the multiphase flow and transport processes. For many decades, multiphase flow has been modeled using the traditional approach based on mass conservation and the generalized Darcy's law. The traditional approach, however, is subject to model errors and numerical errors. The focus of this dissertation research is to improve models of flow and transport in porous medium systems using numerical modeling approaches for a range of scales including pore scale and continuum scale.

A major part of this research examines the deficiency of Darcy's relationship and its extension to multiphase flow using the lattice-Boltzmann (LB) approach. This study investigates the conventional relative permeability saturation relation for systems consisting of water and non-aqueous phase liquid (NAPL). In addition, it also examines the generalized formulation accounting for the interfacial momentum transfer and lends additional support to the hypothesis that interfacial area is a critical variable in multiphase porous medium systems.

Another major part of the research involves developing efficient and robust numerical techniques to improve the solution approach for existing models. In particular, a local discontinuous Galerkin (LDG) spatial discretization method is developed in combination with a robust and established variable order, variable step-size temporal integration approach to solve Richards' equation (RE).

Effective spatial adaptive LDG methods are also developed to further enhance the efficiency. The resulting simulator with both spatial and temporal adaption has demonstrated good performance for a series of problems modeled by RE.

ACKNOWLEDGMENTS

It has been a long, but rewarding journey to complete this extensive research which has helped shape my life. I am eternally grateful to many people who have helped me in many different ways. First and foremost, I would like to take this opportunity to thank my advisor, Prof. Casey Miller, for providing a stimulating research context, for supporting me to carry out this research, and for offering me inspiration and priceless guidance throughout my dissertation research. His passion for subsurface research, his scholarly intelligence and rigor, his academic achievements, and his humor and optimism will extend their influence throughout my career.

I also want to express my gratitude to Dr. Matthew Farthing for being in my dissertation committee and constantly offering his help and support during these many years. His wealth of knowledge, academic rigor, and patience are what made completing this research possible. I also feel extremely fortunate to have Dr. Doris Pan in this research group and to have the opportunity of working closely with her during my graduate study. She has been a wonderful friend and collaborator, who gave me invaluable support during my research work as well as my personal life.

The other members of my dissertation committee — Prof. Jingfang Huang, Prof. Marc Serre, and Prof. Richard Smith — have also been equally supportive and generous with their advice, help, and wisdom. Additionally, I am indebted to Prof. William Gray for his insightful comments and Prof. Clint Dawson at the University of Texas at Austin for his professional guidance. Special thanks are due to all the collaborators I have worked with over the last five years and

colleagues in the groundwater modeling group in UNC.

Last but not least, I would like to thank my parents. Their love, encouragement, and support were undeniably the bedrock that my life has been built around. My appreciation also goes to my fiance, Poh Boon Ung for his love and undying support during this dissertation research.

CONTENTS

	Page
LIST OF FIGURES	xi
LIST OF TABLES	xiv
LIST OF ABBREVIATIONS	xv
Chapter	
I. Introduction	1
1.1 Problem Description	1
1.2 Modeling Flow and Transport in Porous Media - Scale Consideration	3
1.2.1 Microscopic pore scale	4
1.2.2 Macroscopic continuum scale	6
1.2.3 Field scale	7
1.3 Modeling Flow and Transport in Porous Media - Stan- dard Modeling Approach	8
1.3.1 Mathematical formulation of the traditional approach .	10
1.3.2 Numerical methods	13
1.4 Research Objectives	17
1.4.1 Pore-scale lattice Boltzmann approach to ad- vance the traditional continuum modeling approach . .	17
1.4.2 Improved numerical methods - discontinuous Galerkin methods	20
1.5 Organization	22
II. Pore-scale Investigation of Viscous Coupling Effects for Two- phase Flow in Porous Media	24
2.1 Introduction	24

2.2	Background	27
2.2.1	Theoretical developments	27
2.2.2	Experimental investigations	29
2.2.3	Computational simulations	31
2.3	Lattice Boltzmann Model	33
2.3.1	LB-MRT model	33
2.3.2	Two-phase LB model	34
2.4	Model Validation	36
2.4.1	Comparison between BGK and MRT model	36
2.4.2	Two-phase flow in a tube	39
2.5	Two-phase Flow Simulations in Porous Media	41
2.5.1	Setup of the numerical system	41
2.5.2	Results and discussion	44
2.6	Conclusions	57
III.	Local Discontinuous Galerkin Approximations to Richards' Equation	59
3.1	Introduction	59
3.2	Background	61
3.2.1	Overview	61
3.2.2	Approximation of RE	62
3.2.3	Spatial discretization approaches	63
3.2.4	Discontinuous Galerkin methods	63
3.3	Approach	65
3.3.1	Overview	65
3.3.2	Model formulations	65
3.3.3	Spatial approximations	68
3.3.4	Temporal approximation	75
3.4	Results	78
3.4.1	Overview	78
3.4.2	Test problems	78

	3.4.3	LDG schemes	79
	3.4.4	Efficiency Measures	82
	3.4.5	Computational results	84
	3.5	Discussion	97
	3.6	Conclusion	99
IV.		Adaptive Local Discontinuous Galerkin Approximations to Richards' Equation	100
	4.1	Introduction	100
	4.2	Background	102
	4.2.1	Overview	102
	4.2.2	Temporal adaption	103
	4.2.3	Spatial adaption	103
	4.3	Approach	109
	4.3.1	Overview	109
	4.3.2	Model formulations	110
	4.3.3	LDG-MOL approximations	111
	4.3.4	Adaptive solution approaches	115
	4.3.5	K-level adaptive approach	118
	4.3.6	Two-level adaptive approach	124
	4.4	Results	130
	4.4.1	Overview	130
	4.4.2	Test problems	131
	4.4.3	Method summary	132
	4.4.4	Efficiency measures	133
	4.4.5	Numerical results	135
	4.4.6	Discussion	145
	4.4.7	Conclusions	147
V.		Summary and Recommendations	148
	5.1	Summary	148

5.2	Recommendations	150
-----	---------------------------	-----

LIST OF FIGURES

1.1	Hierarchical scales for multiphase systems in porous media. (a) DNAPL/water dissolution and entrapment at the microscale; (b) DNAPL migration pattern at macroscale; (c) A field-scale view, photo taken by Douglas Peebles [151].	5
1.2	Modeling process.	9
1.3	a) van Genuchten p - S relation; b) Mualem S - k relation.	11
1.4	Schematic illustrations of hysteresis phenomena [32]: (a) p - S relation; and (b) S - k relation.	12
1.5	Diagram of the development of a numerical method.	14
2.1	(Color online) Comparison of the measured permeability of a sphere-pack porous medium as a function of fluid viscosities using BGK and MRT models. The permeability results are normalized with respect to the value at $\nu = 0.1$	37
2.2	(Color online) (a) Two-phase flow in a channel with square-shaped cross-section; (b) Cross-sectional velocity profile for a phase viscosity ratio $M = 2$ with 32^2 lattice nodes along the y - z plane; and (c) Error of the simulated velocity v_x profile with respect to the semi-analytical solution versus lattice size N_l for single-phase flow and two-phase flow with a viscosity ratio $M = 2$	42
2.3	(Color online) Snapshots of the non-wetting phase distribution under a higher capillary number [$Ca = 5 \times 10^{-4}$, (a)–(d)] and a lower capillary number [$Ca = 5 \times 10^{-5}$, (e)–(h)]. The NWP region indicated by the arrow in (a) moves through the porous medium driven by momentum transferred from the WP at higher Ca , while it is unable to move at lower Ca	45
2.4	(Color online) Relative permeability vs. WP saturation S_w for co-current two-phase flow with different Ca in a neutrally wet medium at $M = 1$	46
2.5	(Color online) Relative permeabilities as a function of Ca for co-current, two-phase flow with $M = 1$ and $S_w = 0.5$	47

2.6	(Color online) Steady-state distributions of the NWP (a) a neutrally wet medium; and (b) a strongly water-wet medium. Wetting-phase saturation $S_w = 0.509$ in (a) and 0.508 in (b). Dark gray (red online) regions represent the non-wetting fluid, and light gray (yellow online) regions represent the solid phase. For clarity of illustration the wetting fluid is not shown.	48
2.7	(Color online) Relative permeability vs. WP saturation S_w for co-current two-phase flow with different wettability with $M = 1$ and $Ca = 10^{-5}$	49
2.8	(Color online) NWP relative permeability measured by Avraam and Payatakes [18] in a glass pore network with a contact angle of 40° and our simulated results for a NWW system as a function of WP saturation S_w for co-current, two-phase flow with different viscosity ratios at $Ca = 10^{-5}$	50
2.9	(Color online) WP relative permeability measured by Avraam and Payatakes [18] in a glass pore networks with a contact angle of 40° and our simulated results in a NWW system as a function of WP saturation S_w for co-current, two-phase flow with different viscosity ratios at $Ca = 10^{-5}$	51
2.10	(Color online) Generalized relative permeabilities as a function of WP saturation S_w for co-current two-phase flow with $M = 1$ and $Ca = 10^{-5}$	52
2.11	(Color online) Steady-state distributions of NWP with different initial phase configurations: (a) Case 1, (b) Case 2, and (c) Case 3. For all cases, the WP saturation is 0.45–0.46.	55
2.12	(Color online) Conventional relative permeabilities of NWP and WP vs. fluid-fluid interfacial area per unit volume at constant fluid saturations for (a) Case 1, (b) Case 2, and (c) Case 3.	56
3.1	LDG convergence rates for scheme A0-F0 applied Problem I.	85
3.2	Pressure head profiles for Problem III for $t = 0.05, 0.10, 0.15, 0.20$ and 0.25 days.	86
3.3	Comparison of the LDG and FD methods for Problem III.	88
3.4	Computational efficiency for Problem III using the LDG method: (a) temporal error for Runs 8c–17c and 19c–28c, and (b) total error for Runs 8c–17c and 19c–28c.	89
3.5	Pressure head profiles for Problem IV for $t = 0.05, 0.10, 0.15, 0.20,$ and 0.25 days.	92

3.6	Comparison of the LDG method and FD method for Problem IV.	92
3.7	Computational efficiency for Problem IV using the LDG method: (a) temporal error for Runs 37c–46c and 48c–57c, and (b) total error for Runs 37c–46c and 48c–57c.	94
3.8	Comparison of LDG schemes for Problem V at t= 3.0 days.	96
4.1	Flow diagram for operator $\mathcal{M}_{T, hp}$	130
4.2	Pressure head solutions by h K-level method for Problem I	136
4.3	Pressure head solutions by h two-level method for Problem I	137
4.4	Convergence rates of the K-level and two-level methods for Problem I	138
4.5	Convergence rates of the K-level and two-level methods for Problem I	139
4.6	Pressure head solutions by hp two-level method for Problem I	140
4.7	Comparison of the h and hp adaptive methods for Problem I	140
4.8	Comparison of the h and hp adaptive methods for Problem I	141
4.9	Pressure head solutions by h K-level method for Problem II	141
4.10	Pressure head solutions by h two-level method for Problem II	143
4.11	Convergence rates of the K-level and two-level methods for Problem II	143
4.12	Convergence rates of the K-level and two-level methods for Problem II	144

LIST OF TABLES

2.1	Summary of the experimental investigations of viscous coupling effects.	29
3.1	Summary of simulation conditions for Problems I and II	79
3.2	Summary of simulation conditions for Problems III–V	80
3.3	Spatial schemes	81
3.4	Convergence rates for Problem I	85
3.5	Summary of discrete approximation conditions for Problem III	87
3.6	Summary of discrete approximation conditions for Problem IV	91
3.7	Summary of discrete approximation conditions for Problem V	95
4.1	Summary of simulation conditions for Problems I–II	131
4.2	Parameters for the LDG-MOL method	132
4.3	Parameters for the adaptive methods	133
4.4	Summary of adaptive simulation conditions for Problem I	135
4.5	Summary of adaptive simulation conditions for Problem II	142

LIST OF ABBREVIATIONS

BDF	backward difference formula
CFD	computational fluid dynamic
DAE	differential algebraic equation
DAETK	differential algebraic equations' toolkit
DG	discontinuous Galerkin
DNAPL	dense non-aqueous phase liquid
EOS	equations of state
FLC	fixed leading coefficient
IP	interior penalty
LBM	lattice Boltzmann method
LDG	local discontinuous Galerkin
MOL	method of lines
MRT	multiple relaxation time
ODE	ordinary differential equation
PDE	partial differential equation
RE	Richards' equation
REV	representative elementary volume
RK	Runge-Kutta
TCAT	thermodynamically constrained averaging theory

Chapter 1

Introduction

1.1 Problem Description

Groundwater, and thus the entire subsurface hydrosystem, plays an essential role in human life. In the United States, more than 50 percent of the total population relies on groundwater as its drinking water source [248], and groundwater contributed 20 percent of the total water consumption for the last five decades [177]. Unfortunately, recent studies have shown that the quality of groundwater continues to be threatened by many sources of contamination. To date, over 200 organic and inorganic chemicals in excessive amounts, including high levels of dense non-aqueous-phase liquids (DNAPLs) and radioactive isotopes, have been identified in groundwater supply systems [248]. The accumulation of contaminants in subsurface systems poses serious environmental and human health problems. Prevention of the degradation of groundwater quality and remediation of contaminated subsurface systems are significant challenges faced by the water resources community. While there has been a great deal of effort to develop remediation technologies, remediation methods still remain extremely expensive and unpredictable in their success. The design of successful subsurface remediation technologies requires a thorough understanding and accurate prediction of the migration and distribution of contaminants. However, our understanding

of fluid flow and contaminant transport in subsurface systems has not advanced sufficiently enough that most of the major aspects of the fate and transport of contaminants in subsurface systems are well understood, especially when subjected to remediation efforts.

The difficulties that prevent a thorough understanding of subsurface systems are due to their intrinsic complexity and can be summarized in the following aspects.

Multiphase, multispecies systems. Most subsurface systems have multiple fluid phases and multiple chemical species. The system intricacies due to the presence of juxtaposed phases include the existence and dynamics of interfaces between fluid phases, fluid dynamics caused by complicated geometry of pores, pendular rings of a wetting phase, ganglia of the non-wetting phase, and the behavior of films [140]. The species, on the other hand, interact with one another through, e.g., chemical and/or biological reactions, dissolution, volatilization, adsorption and desorption. Moreover, each component can interact with other systems, such as surface water systems, through physical boundaries [262].

Issue of scale. Understanding subsurface systems involves understanding various physical, chemical, and biological processes in a wide range of temporal and spatial scales. The characteristic length of both of these scales can vary by orders of magnitude. Dimensions of the temporal scale range from ten-thousand years in risk-analysis for long-term isolation of radioactive waste [4] – through year-by-year, seasonal, monthly, weekly, daily, and hourly scales for field systems – to minutes and even seconds in certain laboratory experiments [262]. The spatial scales range from nanometers when considering interactions between water molecules and dissolved chemicals to hundreds of kilometers when assessing and managing regional groundwater systems. From a groundwater hydrology perspective, a commonly used hierarchy to describe the spatial scales includes

microscopic pore scale ($10^{-5} - 10^{-3}$ m), macroscopic continuum scale ($10^{-2} - 10^0$ m) and field scale ($10^1 - 10^4$ m) [160, 60, 239]. Measurements of constitutive variables on one scale may appear to have little relevance to other scales [91]; information obtained at scales for which processes are mathematically described has to be incorporated into larger scale formulations amenable to field study.

Heterogeneity. Formation material properties of subsurface systems usually exhibit a high degree of spatial variability at all spatial scales. The intrinsic heterogeneity effects flow and transport processes in the subsurface, yet these processes are extremely difficult to characterize. A good example is that the intrinsic permeability of an aquifer can vary by orders of magnitude even within a given stratigraphic unit. However, monitoring wells can only be placed at a few locations to obtain the permeability data [303]. The combination of significant spatial heterogeneity with a relatively small number of observations results in uncertainty in obtaining sufficient information about subsurface systems and uncertainty in predicting the flow and transport processes in these systems. As a consequence, stochastic concepts have to be used to understand such systems [219].

1.2 Modeling Flow and Transport in Porous Media - Scale Consideration

As groundwater contamination threats continue, increased emphasis is being placed on understanding the various processes operating in subsurface systems. The basic approaches to advance the understanding of subsurface systems include theoretical development, experimental investigations, and computational modeling. Theoretical development provides a framework within which various processes in the subsurface are described. The models that are intended for practical computations necessitate understanding of theories in the context of

numerical approximations over a range of scales. Observations or experiments are necessary in order to test the range of validity of theories and the accuracy of computational approaches [264]. The immaturity of existing theories [147], the high cost associated with the field characterization and experiments, and the dramatic evolution of computer capabilities nowadays combine to make computational modeling approach essential. Mathematical modeling approaches have provided powerful and indispensable tools to advance fundamental understanding, predict the movement and fate of contaminants, and optimize the design of the remediation processes. The success of the majority of groundwater applications, including site investigation and remediation processes, relies upon models that accurately represent the real system of concern and can be efficiently solved.

A groundwater model can be defined as a simplified version of a real-world groundwater system that approximately simulates the relevant excitation-response relations of the real-world system [34]. Due to the fact that a wide range of spatial scales are of concern, the groundwater model components are considered at different scales that cover microscopic pore scale, macroscopic continuum scale, and field scale. Current modeling approaches are scale-dependent and at each scale have their importance and limitations. Evolving the understanding of porous medium systems involves advancing these modeling approaches at each scale. Figure 1.1 illustrates a scale hierarchy associated with flow and transport problems in porous media and the corresponding modeling components at these scales. Brief descriptions of the groundwater models used at different scales are provided next.

1.2.1 Microscopic pore scale

Porous media in a natural system are highly heterogeneous with a complex pore structure. The pore-space provides the operating environment for the physical, chemical and biological processes that occur in porous media; the complex topology of the pore space results in complex moving patterns of fluids, which

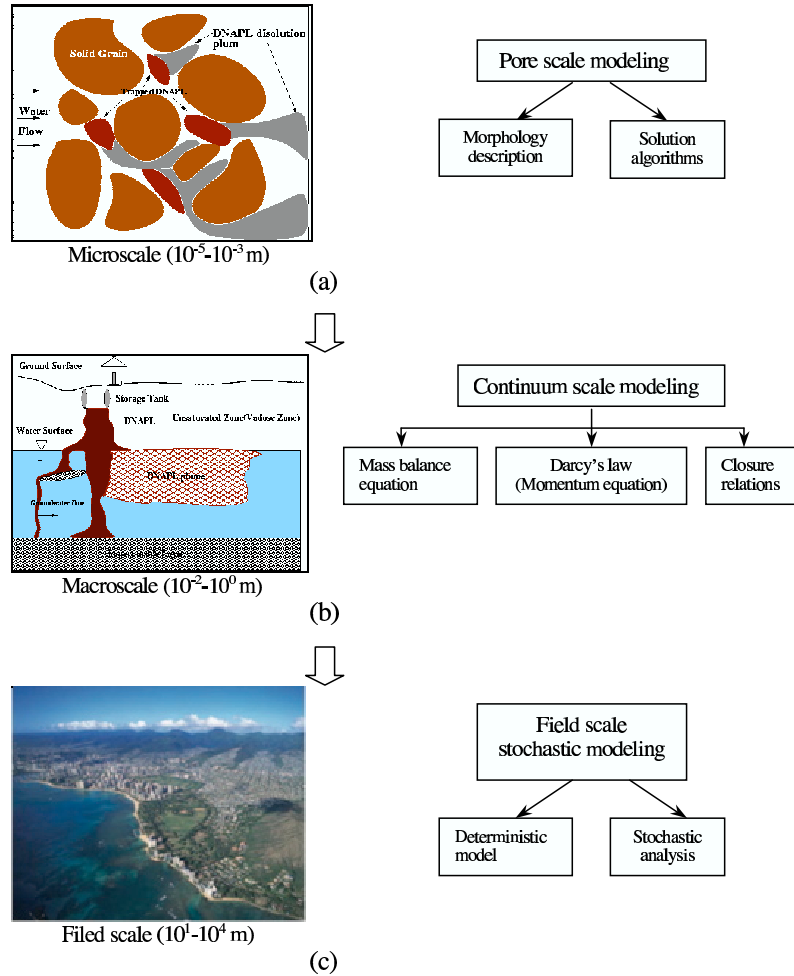


Figure 1.1: Hierarchical scales for multiphase systems in porous media. (a) DNAPL/water dissolution and entrapment at the microscale; (b) DNAPL migration pattern at macroscale; (c) A field-scale view, photo taken by Douglas Peebles [151].

are also influenced by fluid-solid interactions due to wettability, sorption, desorption and reaction, etc. In a multiphase system where, for instance, DNAPL and water are present, each phase exists at its own distinct pressure, with surface tensions along fluid-fluid interfaces supporting pressure differences between the phases [60]. The processes in such systems are further complicated by fluid-fluid interactions through fluid-fluid interfaces due to density difference, viscosity difference and interphase mass transfer.

These mechanisms that dominate the distribution and movement of the flu-

ids exist at the pore scale; thus the complex flow and transport processes in a porous medium need to be resolved at the pore scale, where detailed information, such as the pore morphology and topology, is available. This makes the pore-scale modeling approach fundamental and essential. Pore-scale modeling offers an important tool to understand pore-scale flow and transport processes that influence the macroscopic behavior. In the last decade, the pore-scale modeling approach has been vigorously studied and widely implemented in, but not restricted to, groundwater hydrology and petroleum engineering and has demonstrated its capability to simulate complex behavior of multiphase systems and provide insight into microscopic mechanisms of processes in porous media [209, 252, 159, 200, 68, 241, 187].

In general, pore-scale modeling include two major parts, the description of the porous medium morphology and topology and the solution algorithm [277]. While vigorous work has been done to evolve the characterization of the pore structure [2, 125, 196, 214, 43, 44, 127, 3], increasing emphasis has been placed on developing accurate and efficient solution algorithms. These include pore network modeling approaches and lattice Boltzmann approaches. These methods have shown their capability to simulate complex behavior of multiphase systems, for example, hysteretic saturation-pressure relations [238, 241] and fingering [187].

However, these pore scale modeling approaches are computationally intensive and are not feasible to be used to simulate a system with a characteristic length on the order of meters or longer. Therefore, consistent and appropriate upscaling approaches should be implemented to manifest the microscopic processes at larger scales.

1.2.2 Macroscopic continuum scale

The traditional modeling approach visualizes the porous medium and the fluid phases as continua at a macroscopic level based on the concept of a representative elementary volume (REV) [e.g., 60, 164, 219]. Continuum variables,

such as porosity and fluid saturation, are defined as averages of microscopic variables over an REV. By averaging, the actual pore structure of porous media is ignored and the intricate variations due to the microscopic heterogeneity are smoothed out. In applying the continuum approach to account for experimentally observed phenomena, macroscopic variables and coefficients, such as porosity and permeability, are further introduced.

Continuum modeling approaches are based on mass conservation laws as governing equations, and Darcy's law used as an approximation of momentum conservation. The additional information used to close the conservation equations is known as constitutive relations. These relations serve as a passage to manifest the microscopic mechanism at a macroscopic scale. A detailed introduction of this approach is provided in §1.3.

1.2.3 Field scale

The field scale is the scale of practical concern for hydrologists and petroleum engineers in real-world applications, such as groundwater site characterization, pollution prevention, and monitoring network and remediation design. The traditional modeling approach at this scale is to apply the standard continuum model directly at this scale, assuming the applicability of models for a homogeneous system to a heterogeneous system. This approach, usually based on inconsistent and over-simplified assumptions, is subject to significant errors [219, 91, 92].

Although subsurface systems are intrinsically deterministic, the physical and chemical parameters that characterize them vary substantially in space and time [219, 93, 133]. The impossibility of obtaining complete knowledge due to the complexity of the underlying mechanisms leads to uncertainty in estimating or predicting the flow and transport at the field scale. As a result, natural multiphase porous medium systems can be realistically modeled only by means of stochastic concepts and methods [298, 132, 219, 69, 133]. The existing stochastic models [72, 73, 178, 173, 71, 70, 303] are mostly based on deterministic

continuum models and consequently are subjected to any error existing in the underlying deterministic models. Therefore, an evolution of the models at the field scale involves advancing the traditional deterministic models and advancing the stochastic approaches.

1.3 Modeling Flow and Transport in Porous Media - Standard Modeling Approach

Standard models currently used for practical applications are based on governing equations written at the porous medium continuum scale. A traditional mechanistic modeling process is shown in Figure 1.2. The three basic steps [34, 160] to construct a mathematically based mechanistic model are explained as follows:

- **Conceptual model.** A conceptual model is a high-level, conceptual description of the system involving expert insight to identify the different processes and mechanisms. The degree of abstraction depends upon the purpose of constructing a model for a specific problem. The objective of this step is to provide the simplest possible description of a system necessary for the intended use.
- **Mathematical model.** A mathematical model transfers a conceptual model to a mathematical formulation using conservation laws for mass, momentum and energy and system-dependent closure relations. Appropriate variables to be used in a particular problem must be selected based upon the available data. The number of equations included in the model must be equal to the number of the dependent variables. The mathematical model contains the same information as the conceptual one, but expressed as a set of equations amenable to analytical or numerical solutions [34].
- **Numerical model.** Although an ideal solution for a mathematical model is

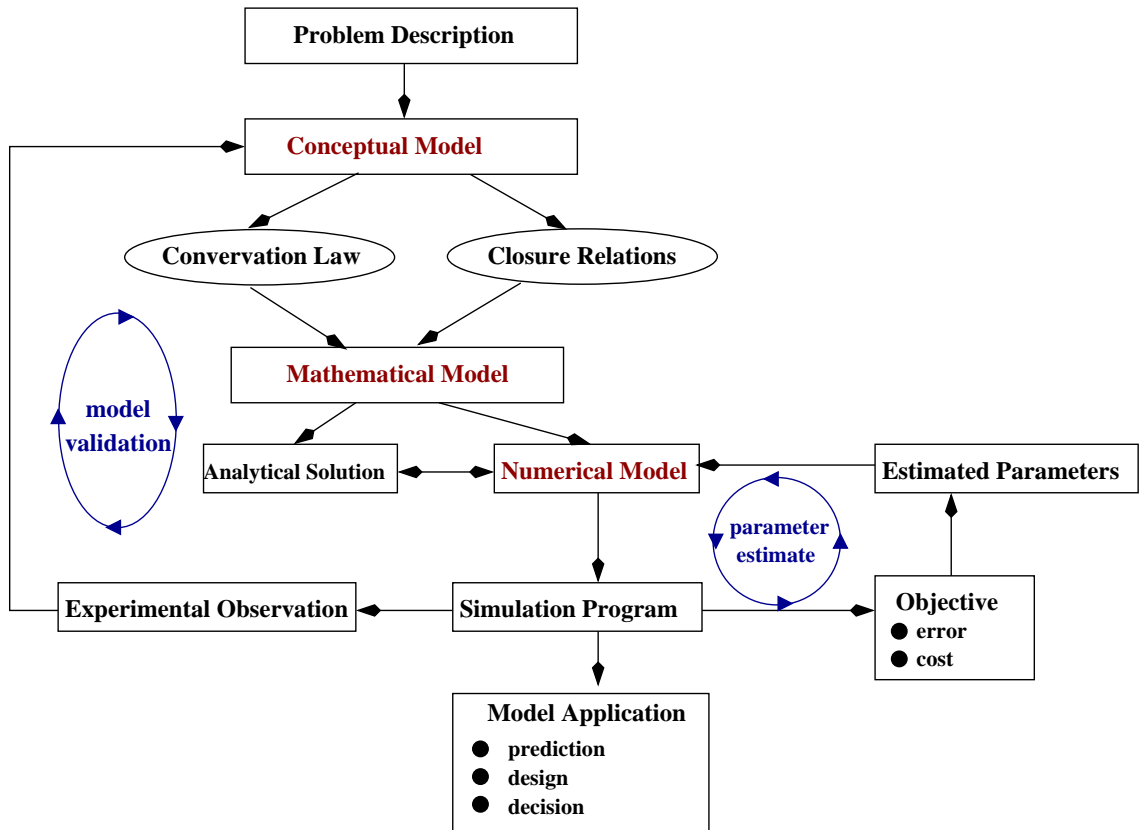


Figure 1.2: Modeling process.

to derive an analytical solution, the complexity of most problems of practical interest requires a solution approach based upon approximate numerical methods. A numerical model transforms a mathematical model to an approximate discrete solution, which is implemented in a computer code.

The difference between the model output and “true” values in the real world can be reflected in two aspects, the model error and the numerical error [122]. The model error is known as the disagreement between a real system and the mathematical simplification or idealization. The numerical error measures the difference between the model output and the true mathematical solution to the model, which is arrived at using numerical approximations. Improving modeling capabilities involves minimizing both the model error and the numerical error. The following summarizes the traditional modeling approach from these two

aspects.

1.3.1 Mathematical formulation of the traditional approach

1.3.1.1 Mathematical framework

The traditional approaches to model flow and transport in porous media are based on continuum theory, which consists of two basis elements, the fundamental conservation law and the functional forms of closure relations (equations of state (EOS) and other constitutive relations).

The governing equations for multiphase flow are the following mass balance equations for the individual phases

$$\frac{\partial}{\partial t}(\phi\rho_\alpha S_\alpha) + \nabla \cdot (\rho_\alpha \mathbf{q}_\alpha) = \mathcal{I}_\alpha + \mathcal{S}_\alpha \quad (1.1)$$

where ϕ is porosity; the subscript α specifies the fluid phase; ρ_α is the density of phase α ; S_α is the saturation, defined as the fraction of the pore volume occupied by the phase α ; \mathbf{q}_α is a vector of the volumetric flow rate per unit area for the α phase; and \mathcal{I}_α and \mathcal{S}_α denote the interface mass transfer function and source/sink function for α phase, respectively.

Momentum balance equations are not typically included in the standard multiphase flow formulations. Instead, the multiphase extension of the empirical Darcy's law introduced by Wyckoff and Botset [296] and Leverett [203] has been used to relate the flux vector \mathbf{q}_α to the pressure gradient of the individual phase. The extension of Darcy's law is written as

$$\mathbf{q}_\alpha = -\frac{\kappa\kappa_{r\alpha}}{\mu_\alpha}(\nabla P_\alpha - \rho_\alpha \mathbf{g}) \quad (1.2)$$

where κ is the intrinsic permeability along the flow direction; $\kappa_{r\alpha}$ is the relative permeability function accounting for the reduction of κ of the medium due to the incomplete saturation by fluid phase α ; μ_α is the dynamic viscosity of fluid α ; P_α denotes the pressure of fluid phase α ; and \mathbf{g} is the gravitational acceleration vector.

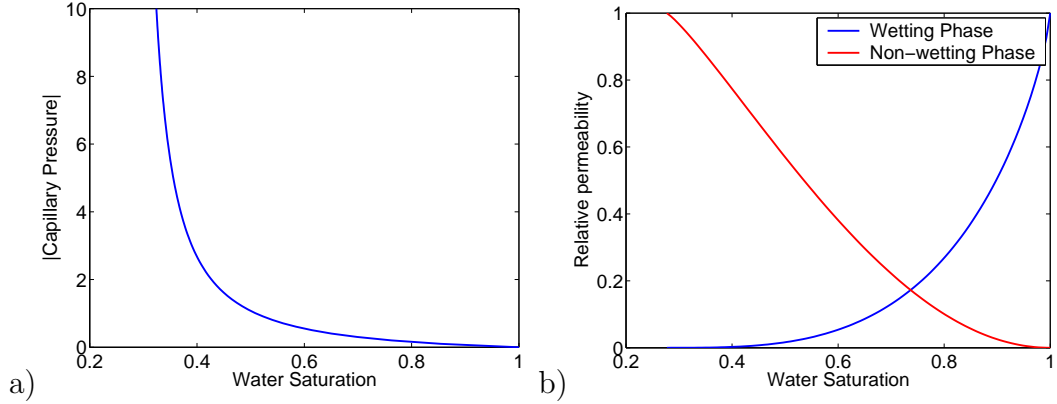


Figure 1.3: a) van Genuchten p - S relation; b) Mualem S - k relation.

Closure relations are necessary to make the system solvable. The relations include equations of state, which are typically based on thermodynamic models [219], and constitutive relations that are empirical and system-dependent. Typical and important constitutive relations are p - S - k relations, which describe the relations among capillary pressure, fluid saturations, and relative permeabilities. The p - S - k relations serve as projection operators to pass the microscopic information to the macroscopic continuous level, while ignoring the detailed and assumed unnecessary information, such as pore morphology.

Two of the most widely used p - S and S - k relations are the van Genuchten [286] and Mualem [226] relations, whose functional forms are written as

$$S_e = \frac{\theta_\alpha - \theta_r}{\theta_s - \theta_r} = \begin{cases} (1 + |\alpha_v P_c|^{n_v})^{-m_v}, & \text{for } P_c < 0 \\ 1, & \text{for } P_c \geq 0 \end{cases} \quad (1.3)$$

$$\kappa_{rw} = S_e^{1/2} [1 - (1 - S_e^{1/m_v})^2] \quad (1.4)$$

$$\kappa_{rn} = (1 - S_e)^{1/2} [1 - S_e^{1/m_v}]^{2m_v} \quad (1.5)$$

where S_e is the effective saturation, θ_r is the residual volumetric water content, θ_s is the saturated volumetric water content, P_c is the capillary pressure defined as $P_n - P_w$, α_v and n_v are experimental parameters, $m_v = 1 - 1/n_v$, and κ_{rw} and κ_{rn} are the relative permeabilities for the wetting phase and the non-wetting phase, respectively. These functional forms are shown in Figure 1.3.

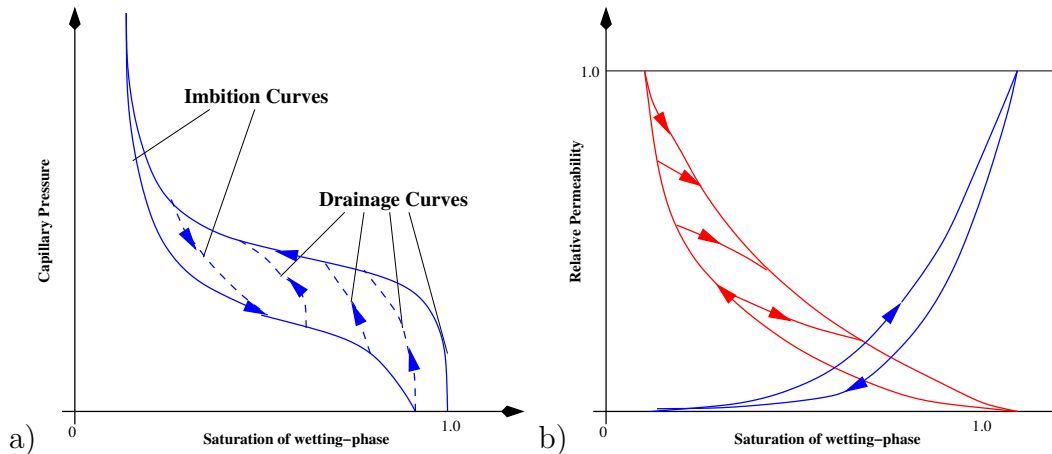


Figure 1.4: Schematic illustrations of hysteresis phenomena [32]: (a) p - S relation; and (b) S - k relation.

1.3.1.2 Limitations

Instead of solving a formal momentum conservation equation, the traditional modeling approach relies upon Darcy’s law and its common extension to multiphase systems. The approach has been questioned in many theoretical [156, 183, 184, 144, 147], experimental [111, 17] and computational investigations [113, 200, 284]. Limitations are reflected in many aspects, including the hysteresis in both p - S and S - k relations and interfacial effects.

Hysteresis in p - S and S - k relations means that the value of capillary pressure and relative permeability have infinitely many different values between an upper and a lower bound, depending on the history of the system and the path along which the particular state was reached [110]. This phenomenon is widespread in nature and was observed by many researchers, for example, Killins et al. [194], Brooks and Corey [52], Botset [49], and Hilpert et al. [162]. Two schematic illustrations of hysteresis phenomena in p - S and S - k relations are shown in Figure 1.4.

Another aspect of multiphase systems that the traditional modeling approach neglects is interfacial effects. It is clear that the existence of interfaces provides

a means for the storage and exchange of mass, momentum and energy [142] and controls many important properties of multiphase systems. However, interfacial physics have not been explicitly accounted for in traditional modeling approaches. An example of the interfacial effects would be the effect of the momentum transfer caused by a viscous force across a fluid-fluid interface, which is referred to as viscous coupling. Recent studies have shown that viscous coupling effects are important over a broad range of porous media flow problems. Those include the theoretical work by Hassanizadeh and Gray [154, 155, 156], Bachmat and Bear [24], Gray [140], Kalaydjian [183], and Kalaydjian [184] and the experimental work by Kalaydjian [184], Bourbiaux and Kalayjian [50], Bentsen and Manai [40], Dullien and Dong [111], Avraam and Payatakes [17, 18, 19], Dana and Skoczylas [95], and Liang and Lohrenz [206].

The existence of the above phenomena indicates that the simple extension of Darcy’s law for multiphase flow is not capable of capturing microscale physics. For example, in the extension of Darcy’s law, saturation is introduced as an indicator of the presence of multiple phases in a macroscale continuum. However, configurations of the fluids can be different under a prescribed saturation, which leads to different flow paths and mechanisms, and thus different values of macroscale variables, such as the relative permeability of each fluid [252]. In the last three decades, there has been vigorous theoretical work attempting to develop a rigorous and consistent framework for formulating macroscale models that better account for pore-scale physics [154, 156, 24, 33, 145, 140, 147, 221]. The development of these improved models requires improved theoretical, computational and experimental investigations and justification, which must involve a high-resolution description of the operative physical mechanism, at microscale.

1.3.2 Numerical methods

The resulting mathematical models are typically in forms of a set of partial differential equations (PDE’s) with boundary conditions and initial conditions.

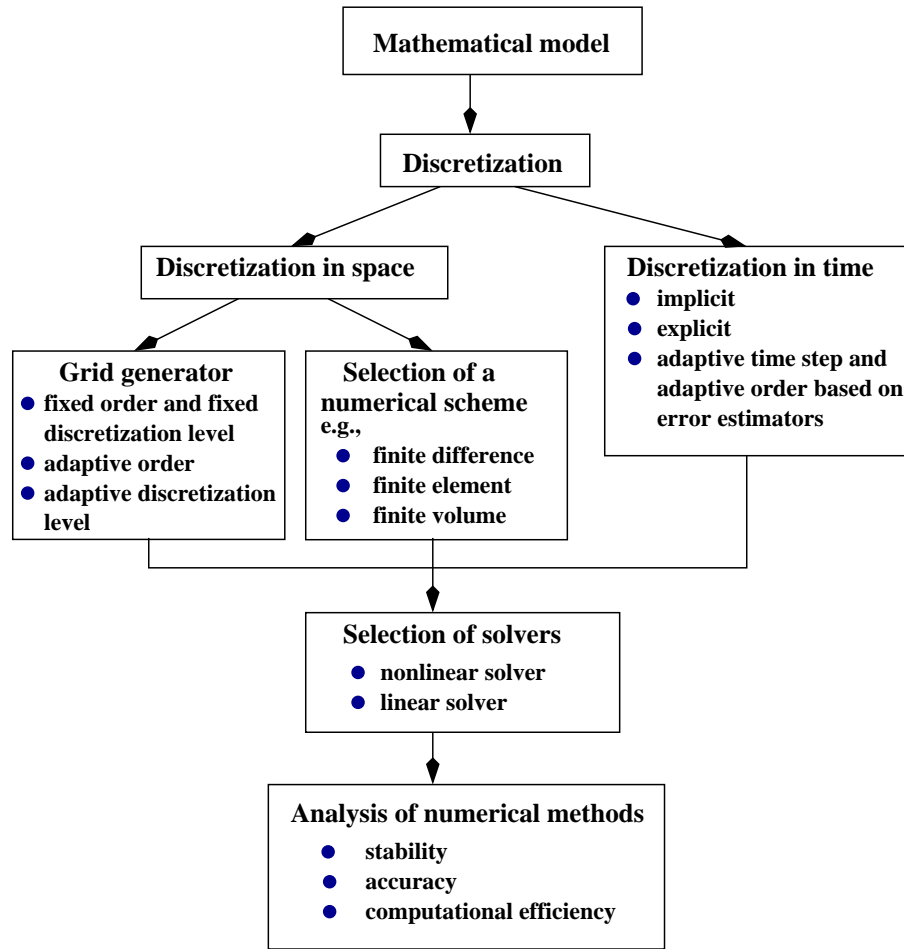


Figure 1.5: Diagram of the development of a numerical method.

Usually, the solution of these PDE's cannot be achieved without the use of numerical methods, which are normally implemented in a computer program. From an applied mathematics perspective, numerical methods are evaluated in terms of numerical bench-marks, such as stability, convergence, and accuracy of the scheme; from a computational science perspective the concern regarding a numerical scheme involves computational efficiency and memory usage. Figure 1.5 shows steps involved in developing a numerical method. While certain standard numerical approaches exist to treat different PDE's according to their classification as hyperbolic, parabolic, or elliptic PDE's, special properties of multiphase flow and transport equations require special attention in order to develop accu-

rate and efficient numerical schemes. These special properties of PDE's used to model multiphase systems include their nonlinearity, regularity, coupling, sharp fronts, and heterogeneity in parameters, which will likely continue to play a major role in the evolution of multiphase modeling.

Numerical modeling of a subsurface system requires choosing spatial discretization, temporal discretization, a nonlinear solver and a linear solver. Particular interest has been focused on developing accurate and efficient schemes in terms of spatial and temporal discretizations, as summarized below.

1.3.2.1 Spatial discretization

The most popular numerical methods to discretize PDE's are finite difference methods. These methods express the solution in terms of nodal points and replaces the derivatives by differences taken between those nodal points. They provide solutions that conserve mass discretely over each cell, which is a desirable property. However, finite difference methods are not as easily applied to irregular domains [201]. In addition, finite difference methods generate numerical dispersion when applied to problems with sharp fronts [35].

Finite element methods and finite volume methods are both based on a conservative weighted residual integration, known as a weak formulation. Standard conforming finite element techniques can give high-order approximations in space. However, when applied to flow problems, the resulting velocities are discontinuous across element interfaces and do not conserve mass over an element [42, 300]. Other disadvantages of the standard finite element methods include numerical oscillations (known as the Gibbs effect) when applied to problems with discontinuities [62, 59, 88, 107] and complexity in dealing with hanging nodes. Finite volume methods, on the other hand, are known to be mass-conservative and non-oscillatory [120], but unfortunately, they are low-order approximations.

A series of approaches has been considered over the years in hopes of combining the flexibility and high order approximation of the finite element methods

with the local conservation properties of finite difference discretizations. These include control volume finite element discretizations [128, 288], mixed finite element methods [63, 11, 66, 65, 101, 41, 300], and post-processing of pressure fields obtained from conforming methods [90, 112]. It has been shown that control volume finite element method provides significant improvements in accuracy over the classical finite element technique. In several works, mixed finite element discretizations have shown a number of benefits in comparison to conforming finite element methods [225, 175], control volume finite element discretizations [112] and the post-processing method [225]. Recent investigations have also shown several advantages for combinations of mixed finite element methods and higher order adaptive time integration via the method of lines [123, 220]. The disadvantages of control volume finite element and mixed finite element methods, however, are the extra effort needed for constructing auxiliary meshes and for hybridization, respectively.

1.3.2.2 Temporal discretization

The time discretization of the PDE's describing multiphase systems is traditionally dominated by low-order time-marching methods. These include implicit backward Euler, implicit Crank-Nicholson, explicit forward Euler and explicit Runge-Kutta algorithms. However, there exist adaptive high-order time integration packages, for example, DASPK, for systems of ordinary differential equations (ODE's) and differential algebraic equations (DAE's). These time integration packages implement sophisticated variable-order, variable-step-size time discretization with formal error control. A method of lines (MOL) procedure allows us to reduce the PDE's to a systems of ODE's by applying the spatial discretization to the spatial parts of PDE's so that the existing robust and mature time integration methods can be used to perform the time integration.

In the most popular ODE/DAE solver DASPK, a fixed leading coefficient backward difference formula (FLC-BDF) with complex variable-order, variable-

step-size and error-controlled procedure is adopted. This approach advances the approximate solution in time for less computational effort than a lower-order method [281]. Recently, an object-oriented DAE's toolkit (DAETK) was developed by Kees and Miller [190] based on DASPK. The object-oriented techniques used to design the large and complex code make this time integrator extensible, flexible and easy to use. The ODE/DAE solvers, combined with various spatial discretization, such as finite difference and mixed finite elements, have been applied successfully for simulating various multiphase flow problems [191, 123, 124] and advantages over low-order time integration methods have been demonstrated.

1.4 Research Objectives

The overall goal of this work is to improve models of flow and transport in porous medium systems using numerical modeling approaches for a range of scales. This objective is being pursued along two lines: (1) using a pore-scale LB approach to investigate viscous coupling phenomena and advance the traditional continuum modeling approach; and (2) developing robust numerical methods (discontinuous Galerkin methods) for existing continuum model formulations to improve numerical accuracy and efficiency.

1.4.1 Pore-scale lattice Boltzmann approach to advance the traditional continuum modeling approach

The deficiency of Darcy's relationship and its extension to multiphase flow motivated researchers to pursue a better model to account for the interfacial viscous coupling phenomena. This led to a generalized formulation [154, 155,

156, 24, 183, 184, 140] written as

$$\begin{bmatrix} \mathbf{v}_w \\ \mathbf{v}_n \end{bmatrix} = - \begin{bmatrix} \kappa\kappa_{r,ww}/\mu_w & \kappa\kappa_{r,wn}/\mu_n \\ \kappa\kappa_{r,nw}/\mu_w & \kappa\kappa_{r,nn}/\mu_n \end{bmatrix} \begin{bmatrix} (\nabla P_w - \rho_w \mathbf{g}) \\ (\nabla P_n - \rho_n \mathbf{g}) \end{bmatrix}. \quad (1.6)$$

where \mathbf{v}_i ($i=w,n$) is the Darcy velocity for the wetting phase and non-wetting phase, P_i is the fluid pressure, and $\rho_i \mathbf{g}$ is the body force. The generalized relative permeability coefficients include two conventional coefficients, $\kappa_{r,nn}$ and $\kappa_{r,ww}$, and two off-diagonal coefficients, $\kappa_{r,nw}$ and $\kappa_{r,wn}$, indicating that for two-phase flow systems, fluid flow will depend not only on the corresponding thermodynamic forces of the fluid, but also on the influences of other irreversible processes. In this formulation, the Onsager's fundamental reciprocity relation [236, 237] was applied at the macroscale so that the cross coefficients $\kappa_{r,nw}$ and $\kappa_{r,wn}$ are thought to be equal. However, this model has not succeeded in resolving the complexity of two-phase flow through porous media. The generalized flow theory fails in two counts. First, the theory is of the Onsager type [184]; however, the controversial issue regarding whether or not the two cross coefficients are equal has not been settled [36, 37, 140, 20]. Second, the generalized relative permeabilities, as the conventional relative permeabilities do, turn out to be strongly dependent on many system parameters, including capillary number, equilibrium contact angle and history of saturation [17, 18, 257].

Recently, a consistent and systematic approach, referred to as the thermodynamically constrained averaging theory (TCAT) approach, has been proposed [147, 221] for modeling multiphase flow. The approach is based upon a complete and rigorous set of conservation equations that are closed with a set of relations that account for the effects of interfaces formed at the junction of two phases, rather than *ad hoc* empirical relations [140]. While there have been active research efforts devoted to test this theory [223, 249, 89, 252, 148, 157, 158, 304], the evolving theory still requires improved experimental and computational approaches for investigation and justification.

We believe that the viscous coupling phenomenon is essentially caused by

many pore-scale intricacies in a multiphase system, such as the configuration of wetting phase and non-wetting phase, fluid viscosities, the interfacial tension and the fluid-solid interactions due to wettability, etc. These phenomena must be understood at a microscopic pore scale, where detailed information, such as the pore morphology and topology, are available and the interfacial physics of fluids are explicitly accounted for.

The lattice Boltzmann method (LBM), an evolving and powerful pore-scale modeling approach, has received increasing attention in computational fluid dynamics (CFD). In the LBM, fluid is represented by a distribution of particles moving on a regular lattice. Upon collision at a node, the particles conserve mass and momentum according to pre-specified mathematical rules given by the discrete Boltzmann equation. Several nonlinear PDE's in CFD, including the Navier-Stokes equations, can be recovered using the LB approach. The LBM is extremely appealing in porous medium simulation because: (1) it is well-suited to simulate complex geometries [241]; (2) the multicomponent version of the LBM is available, allowing the simulation of multiphase systems [263, 268, 269]; and (3) it is straightforward to implement on parallel machines since LB algorithms require information about the distribution function at only nearby points in space [186, 239].

A multicomponent fluids version of the LBM has been derived by Shan and Chen [269, 268] and Shan and Doolen [271]. In this model, a nonlocal interaction force between particles at neighboring lattice sites is introduced so that the global momentum conservation is satisfied when boundary effects are excluded [271, 165]. This formulation has been implemented by Pan et al. [240, 241] to calculate the intrinsic permeability for the single-phase flow and investigate hysteresis of p - S curve in two-phase flow in a 3D porous medium. The code was then parallelized for higher efficiency [243]. This provides a good tool to further investigate the S - k relations and the viscous coupling effects in two-phase porous medium flow. The specific objectives of this work are to:

- review the research conducted to date on viscous coupling effects in two-phase porous media flow systems from theoretical, experimental and computational aspects;
- implement a multiple-relaxation time (MRT) LB model capable of simulating two-phase flow in a 3D porous medium system;
- validate the LB model by simulating two-phase flow where an analytical solution that explicitly accounts for the interfacial stress is available;
- investigate the effect of capillary number, wettability and viscosity ratio on the conventional relative permeabilities in co-current two-phase flow through a sphere-pack porous medium;
- develop strategy for calculating the coupling coefficients and address questions related to their magnitudes and equality; and
- investigate the hypothesis advanced in the TCAT approach that interfacial area is a critical variable in multiphase porous medium systems.

1.4.2 Improved numerical methods - discontinuous Galerkin methods

Over the last decade, discontinuous Galerkin (DG) finite element methods have received widespread and significant attention in CFD applications because of their inherent robustness and many other computational advantages. These CFD applications include a number of fields for hyperbolic PDE's [86, 87, 14] and more recently elliptic and parabolic problems [233, 254, 254, 14, 28, 135]. The first DG method was introduced in 1973 by Reed and Hill [251] for hyperbolic problems and later the Runge-Kutta DG (RKDG) method was developed for hyperbolic problems [86]. Recently, these methods have been applied to elliptic and parabolic equations; the examples include the method of Bassi and Rebay [26] and more importantly, the local discontinuous Galerkin (LDG) method [87, 75, 58]. Simultaneously, but independently, various discontinuous Galerkin

methods using interior penalty (IP) terms for elliptic and parabolic equations were proposed and studied by Douglas and Dupont [109], Wheeler [289], Oden and Baumann [233], Rivière et al. [254], and Rivière et al. [254]. An *a priori* error estimates have been derived for most of the DG methods [255, 58] and some numerical comparisons have shown the advantages of RKDG for multiple-dimensional nonlinear hyperbolic PDE's [88] and advantages of LDG over other DG methods for a linear elliptic PDE [56].

The advantages of DG methods over the traditional counterparts are that:

- DG methods enforce the non-linear conservation laws locally on each element, which results in locally mass-conserving velocity fields. DG methods, however, achieve this without the use of auxiliary variables or the need for hybridization.
- DG discretizations are inherently local and so well-suited for unstructured, even non-conforming meshes. They easily allow for the order of approximation to vary from element to element [230, 25], so that higher order approximations may be used where the solution is locally smooth. This flexibility in handling general meshes and varying approximation orders makes DG methods promising candidates for *hp* adaptive strategies [21, 254].
- DG methods are highly parallelizable. The mass matrix from a DG method is block diagonal and becomes diagonal when orthogonal basis functions are adopted. The stiffness matrix for an element only involves the element itself and the elements sharing a face; the communication between processors is thus minimized.

These features of DG methods are especially appealing for modeling sub-surface problems and have been applied and studied in this field. For simple problems that can be fit into the classification of PDE's (hyperbolic, elliptic and parabolic) and behave like the model problems used in developing these methods, we expect that DG methods can be directly applied with success. However,

some special properties of subsurface systems, for example, heterogeneity, the nonlinear nature, and coupling, require more attention and effort. While some work has been done to solve various PDE's that appear routinely in subsurface systems [28, 254, 7, 121], there are a range of issues still remaining. For groundwater flow problems, an example would be that the performance of various DG methods for highly nonlinear parabolic problems like Richards' equation have not been fully investigated.

Richards' equation has been used routinely to model air-water systems. The challenge to solve Richards' equation comes from the fact that it is parabolic(diffusive) mathematically, yet can generate a sharp advective front that propagates through the domain. This makes the standard treatment of hyperbolic shocks a poor solution scheme. Moreover, the difficulty of solving RE is only exacerbated by highly nonlinear p - S - k relations and the heterogeneous intrinsic permeability that can vary by orders of magnitude. In this work, we attempt to apply the LDG spatial approximation combined with high-order time integration to solve some benchmark RE problems. In addition, we evaluate the performance of various DG methods. The specific goals of this work are:

- to formulate a numerical solution for RE with LDG spatial discretization combined with a robust, higher order temporal approximation in 1D;
- to develop robust and efficient spatially adaptive methods capable of accommodating both h and p type adaption;
- to evaluate the robustness and efficiency of the proposed methods for a range of common RE problems.

1.5 Organization

The dissertation consists of three major components to meet the research objectives. Chapter 2 investigates the viscous coupling effects for two-phase flow in porous media using a three-dimensional parallel processing version of a two-fluid-

phase LB model. Chapter 3 solves RE on a continuum scale using a combination of a robust and established variable order, variable step-size backward difference method for time integration with an evolving spatial discretization approach based upon the LDG method. Chapter 4 develops adaptive LDG methods in combination with sophisticated time integration, resulting in an improved numerical simulator capable of adapting in both time and space. Each of these chapters is similar to manuscripts for individual papers which have been either published, or submitted for publication. Chapter 5 concludes the dissertation with a summary of the results of this work and recommendations for further research. A bibliography of the manuscripts associated with Chapter 2 through Chapter 4 is listed below.

Chapter 2:

Li, H., C. Pan and C. T. Miller, Viscous coupling effects for two-phase flow in porous media, *Physical Review E*, Volume 72, Number 2, 026705, page 1-14, 2005.

Chapter 3:

Li, H., M. W. Farthing, C. N. Dawson, C. T. Miller, Local discontinuous Galerkin approximations to Richards' equation, *Advances in Water Resources*, in press, 2006.

Chapter 4:

Li, H., M. W. Farthing, C. T. Miller, Adaptive local discontinuous Galerkin approximations to Richards' equation, *Advances in Water Resources*, to submit, 2006.

Chapter 2

Pore-scale Investigation of Viscous Coupling Effects for Two-phase Flow in Porous Media

2.1 Introduction

Simultaneous two-fluid-phase (hereinafter two-phase) flow in porous medium systems occurs routinely in nature and is of significant interest in many environmental and industrial processes, including enhanced oil recovery and remediation of hazardous waste sites by non-aqueous phase liquid (NAPL) spills. While the use of the conservation of mass equation to represent the flow systems are fundamental, the closure relations employed to complement the balance are empirical. The conventional closure of the system relies upon the use of relative permeabilities of each of two fluids from an extension of Darcy's law for single-phase flow, instead of a formal conservation of momentum. However, Darcy's law is strictly valid only for creeping single-phase flow [259]. For two-fluid-phase systems, the conventional view implies that the flows of the two fluids are essentially uncoupled and that the pressure gradient and gravity are the only driving forces for each individual fluid. The existence of viscous coupling between the two

immiscible fluids, due to the momentum stress being transferred across the fluid-fluid interfaces [37, 38, 20], makes the simple extension of Darcy's law highly questionable. Another assumption of the conventional Darcy's law under serious challenge is that the relative permeability is a function of the corresponding fluid saturation only. It has been posited that two-phase flow depends upon many flow parameters, such as fluid saturations, capillary number, wettability, and the viscosity ratio between the non-wetting and wetting phases. Viscous coupling of the fluids is affected by each of these factors [114, 17, 18, 19].

The majority of theoretical approaches [102, 290, 154, 155, 156, 24, 140, 183, 184] intended to improve upon the traditional two-phase flow model have led to a similar generalized model for two-phase flow that accounts for interfacial viscous coupling effects. In the generalized model, the flow of each fluid phase is a linear function of gradients of both phases, indicating that in two-phase flow systems, fluid flow will depend not only on the corresponding pressure gradient and body forces for the fluid of concern, but also on the corresponding terms for the companion fluid. This model results in four generalized coefficients, which are commonly referred to as generalized relative permeability coefficients. While there have been various experimental studies showing that the coupling coefficients are important for a range of porous medium flow problems [17, 18, 19, 111], measurement techniques of the generalized coefficients are highly distinctive and the validity and reliability of the obtained results are in many cases questionable [257, 95]. In addition, the model has not succeeded in resolving the complexity of two-phase flow through porous media. The generalized flow theory fails on two counts. First, the theory is of the Onsager type; however, the controversial issue regarding whether or not the two cross coefficients are equal has not been settled [20]. Second, the generalized relative permeability coefficients depend strongly on capillary number, equilibrium contact angle, and the fluid saturation history [17, 257], which is also the case with the traditional two-phase flow model.

Recently, a consistent and systematic approach, referred to as the thermody-

namically constrained averaging theory (TCAT) approach, has been proposed for modeling multiphase flow [147, 221]. The approach is based upon a complete and rigorous set of conservation equations that are closed with a set of relations that account for the effects of interfaces formed at the junction of two phases, rather than ad hoc empirical relations [140]. One of the conclusions from this approach is that the interfacial area between phases is an important variable that must be incorporated into a complete two-phase flow model. While there have been active research efforts devoted to test this theory [223, 249, 89, 252, 148, 157, 158, 304], the evolving theory still requires improved experimental and small-scale computational approaches to determine the appropriate microscale processes and closure relations.

The overall goal of this work is to investigate quantitatively the viscous coupling phenomenon of two-phase flow in a porous medium from a microscopic pore-scale perspective, where detailed information, such as the pore morphology and topology, is available. The specific objectives of this work are to

- review the research conducted to date on viscous coupling effects for two-phase flow in porous medium systems from theoretical, experimental, and computational efforts;
- advance a multiple-relaxation time (MRT) LB model capable of simulating two-phase flow in three-dimensional porous medium systems;
- validate our model by simulating a simple case of two-phase flow in which a theoretical solution that explicitly accounts for the interfacial coupling is available;
- investigate the effect of capillary number, wettability, and viscosity ratio on the conventional relative permeabilities in co-current two-phase flow through a sphere-pack porous medium;
- develop and execute a strategy to calculate the coupling coefficients in the generalized model; and

- investigate the hypothesis advanced in the TCAT approach that interfacial area is a critical variable in multiphase porous medium systems.

2.2 Background

2.2.1 Theoretical developments

The traditional model describing the flow of two immiscible fluid phases under steady-state conditions relies upon an extension of Darcy’s law, written as

$$\mathbf{v}_i = -\frac{\kappa\kappa_{r,i}}{\mu_i}(\nabla p_i - \rho_i\mathbf{g}) \quad (2.1)$$

where $\mathbf{v}_{i(i=w,n)}$ is the Darcy velocity for the wetting phase and non-wetting phase, p_i is the fluid pressure, $\rho_i\mathbf{g}$ is the body force, μ_i is the dynamic viscosity of the fluid, κ is the intrinsic permeability determined by the pore structure of the porous medium alone, and $\kappa_{r,i}$ is the relative permeability that depends upon fluid saturations, or fraction of the pore space occupied by each fluid, and potentially other factors.

As viscous coupling effects have been increasingly recognized, several theoretical approaches have been adopted to describe viscously coupled multiphase flow in porous medium systems. de la Cruz and Spanos [102], Hassanizadeh and Gray [154, 155, 156], Bachmat and Bear [24], Gray [140], and Whitaker [290] applied a volume averaging method to Stokes equation to arrive at a modified theory that includes viscous coupling effects between two fluid phases. Kalaydjian [183, 184], on the other hand, used the ideas of irreversible thermodynamics to develop analogous transport equations describing immiscible two-phase flow in isotropic media.

These different theoretical approaches produced a similar final formulation that we will refer to as the generalized two-phase flow model, which may be

written as

$$\begin{bmatrix} \mathbf{v}_w \\ \mathbf{v}_n \end{bmatrix} = - \begin{bmatrix} \kappa\kappa_{r,ww}/\mu_w & \kappa\kappa_{r,wn}/\mu_n \\ \kappa\kappa_{r,nw}/\mu_w & \kappa\kappa_{r,nn}/\mu_n \end{bmatrix} \begin{bmatrix} (\nabla p_w - \rho_w \mathbf{g}) \\ (\nabla p_n - \rho_n \mathbf{g}) \end{bmatrix}. \quad (2.2)$$

The generalized relative permeability coefficients include two conventional coefficients, $\kappa_{r,nn}$ and $\kappa_{r,ww}$, and two off-diagonal coefficients, $\kappa_{r,nw}$ and $\kappa_{r,wn}$.

One view of Eqn. (2.2) is that this expression is a macroscale application of Onsager's fundamental reciprocity relation [236, 237], which is the basis of the thermodynamics of irreversible processes at the microscopic level. According to Onsager's theorem, the cross coefficients, $\kappa_{r,nw}$ and $\kappa_{r,wn}$ in this case, are symmetric given a linear relationship between the forces and fluxes for an irreversible process. However, there has been diversity in opinions regarding whether or not Onsager's reciprocity relations of irreversible thermodynamics for microscopic systems are applicable to macroscopic viscous coupling phenomena. Among those who argue in favor of the applicability of Onsager's theory to coupled flows in porous media are Rose [258, 256], Kalaydjian [183, 184], Gunstensen and Rothman [149], and Auriault and Lewandowska [15]. Opposing views, however, are to be found in Bentsen and Manai [40], Goode and Ramakrishnan [137], Bentsen [36], Avraam and Payatakes [17, 18, 19], Dullien and Dong [111], and Bentsen [37]. They argue that the nature of two-phase porous medium flow is not amenable to the Onsager-type relation, due to the fact that the coupling permeability coefficients are complex functions of the characteristics of the flow systems and are dependent on many nonlinear pore-scale flow processes.

Recently, the TCAT approach has been advanced as a rigorous basis for the development of models of flow and transport phenomena in porous medium systems [147, 221], which is the evolution of formal constrained averaging theory work that has been ongoing for many years [146, 154, 139, 143, 145, 140, 141]. This approach starts from microscopic balance equations of mass, momentum, and energy for two fluid phases, a solid phase, and the interfaces between the phases. Averaging theorems and geometric constraints are used to simplify the

Table 2.1: Summary of the experimental investigations of viscous coupling effects.

Investigators	Dim.	Medium	Experimental method	$\max(\frac{\kappa_{r,nw}}{\kappa_{r,nn}})$	$\frac{\kappa_{r,nw}}{\kappa_{r,wn}} = 1$
Kalaydjian [184]	3	Capillary tube	Co-current steady-state	70 %	Yes
Bentsen and Manai [39]	1	Sandpack	Co-current and counter-current steady-state	>15%	No
Liang and Lohrenz [206]	1	Sandpack	Combination of steady-state and unsteady-state	70%	Yes
Dullien and Dong [111]	1	Sandpack	Co-current steady-state	35 %	No
Avraam and Payatakes [17, 18, 19]	2	Pore network	Co-current steady-state	120 %	No

entropy inequality and guide the development of closure relations needed to yield well-posed models. As a result of this work, the importance of fluid-fluid interfaces in multiphase systems has been distinguished and incorporated in model formulations. Interfacial areas are considered as additional averaged macroscale variables that represent additional information related to the microscopic state of the system, such as the evolution of the distribution of fluids in the pore space. The importance of taking interfacial areas into account, including the potential to remove hysteresis from capillary pressure-saturation closure relations, has been demonstrated by several studies [252, 94, 159]. However, interfacial areas are not explicitly a part of either the traditional multiphase flow model or the generalized flow model.

2.2.2 Experimental investigations

Standard methods for measuring conventional relative permeabilities rely upon steady-state, uniform flow and constant capillary pressure gradients for both phases without gravitational effects. However, these approaches are unable to discern the values of the diagonal coupling coefficients. Seeking a suitable method to measure all four relative permeabilities in the general model is diffi-

cult. Limited numbers of experimental studies have attempted to do so, and a summary of these studies is reported in TABLE I.

Generally, three types of experiments are conducted to measure the permeability coefficients: steady-state [184, 50, 40, 111, 17, 18, 19, 95], unsteady-state (so-called immiscible displacement) [12, 185], and a combination of steady-state and unsteady-state [206]. The immiscible displacement experiments are the least time-consuming, allowing values of relative permeability and capillary pressure to be determined dynamically. However, these approaches are subject to uncertainties and measurement errors, which are caused by varying capillary pressure gradients and saturation gradients.

Steady-state experiments, on the other hand, are more popular among experimental investigators because the fluid saturations, flow rates, and pressure gradients in the system can be directly measured, making them seem more reliable. Several experiments, such as those by Dullien and Dong [111] and Zarcone and Lenormand [302] on sand packs, were performed by applying external force to only one fluid, so that the first two coefficients were determined and then alternately the other two coefficients were determined. Another approach, in which co-current flow is first applied by adding equal external forces to both fluids and then counter-current flow by adding the opposite forces, were explored in, for example, Bentsen and Manai [40].

A more systematic and complete set of experimental work was pursued by Payatakes' group [16, 17, 18, 283, 19, 284], who performed experiments on a two-dimensional glass pore network model on a square lattice. Fluids with constant flow rates were injected through the medium co-currently until steady-state conditions were achieved. By varying the ratio of flow rates and pairs of fluids, relative permeability coefficients as a function of capillary number, wettability, viscosity ratio, and ratio of injecting flow rates were investigated, and a strong correlation between the macroscopic permeabilities and the steady-state pore-scale flow mechanisms was reported based on the capillary number in the flow

system.

As the importance of interfacial area has been increasingly recognized, experimental measurement techniques have been developed to measure such quantities [223, 265, 266]. However, due to the difficulty in determining the four relative permeability coefficients in the generalized model and measuring the interfacial area, to the best of our knowledge no experimental study has appeared that has investigated the relationship between viscous coupling in two-phase flow and interfacial area.

2.2.3 Computational simulations

Since experimental work that aims to explore all the related flow characteristics is difficult to perform, current experimental studies on viscous coupling effects are all limited to one- and two-dimensional systems. On the other hand, numerical simulations, having benefited from the dramatic evolution of computational capabilities and new algorithms, have significant promise for helping advance fundamental understanding of viscous coupling theory and for guiding the design and interpretation of experimental studies. However, compared to laboratory experimental approaches, investigative studies to investigate viscous coupling using numerical means are extremely limited. Conventional numerical investigations using, for example, finite-difference and finite-element methods are even more scarce [258, 136] because of difficulties associated with pore-scale simulation of multiphase flow using such techniques.

Recently, the lattice Boltzmann (LB) method [216, 161], a relatively new method derived from its precursor, the lattice-gas cellular automata method [130, 129], has grown in popularity in the field of computational fluid dynamics, because it provides a means of simulating true flow mechanisms with a realistic pore geometry for multiphase flow. It also allows more versatility in the choice of parameters than can be had in experiments and provides detailed information about flow processes at the microscale. However, only a few published stud-

ies have investigated viscous coupling effects using these methods. Olson and Rothman [235] attempted to estimate the coupling coefficient using a lattice-gas model in a digitized rock geometry obtained by X-ray microtomography [195]. Langaas and Papatzacos [200] simulated co-current and counter-current steady-state flows at different wettabilities, viscosity ratios, and driving forces using a Bhatnagar-Gross-Krook (BGK), single-relaxation-time lattice Boltzmann model for a two-dimensional, uniform pore space.

Gunstensen and Rothman [149] used a BGK color-gradient lattice Boltzmann model to simulate two-phase flow in a three-dimensional porous medium. They delineated regions of linearity and nonlinearity between Darcy velocities and forcing as a function of fluid saturations, and they observed Onsager reciprocity in the linear region where a relatively high body force was applied. However, some significant issues still remain unresolved: (1) the applicability of Onsager theory in the nonlinear regime, which represents flow in the majority of hydrological applications; (2) the consideration of porous medium systems with more realistic pore structure than those considered to date; and (3) application of modern, high-resolution LB methods. The studies mentioned above, although limited in number, provide motivation for a more complete study.

Another important aspect of viscous coupling is to elucidate the role of interfacial effects, as several researchers have realized [149, 17, 18]. By applying the LB model at the microscopic pore scale, the interfacial area between fluid phases can be readily determined. A marching cubes algorithm has been used extensively as a tool to resolve graphical interfaces [305, 208, 103]. Recently, a modified marching cubes (MMC) algorithm has been successfully implemented and used to compute interfacial area using data sets obtained directly from LB simulations [215]. This approach provides a means to investigate the dependence of relative permeabilities on the interfacial area and to evaluate the validity of evolving theories.

2.3 Lattice Boltzmann Model

2.3.1 LB-MRT model

The LB method involves solving the microscopic Boltzmann equation, which can be viewed as a discrete approximation of the incompressible Navier-Stokes equations based on kinetic theory [182]. In the LB method, fluid flow is represented by the distribution functions of fluid particles moving on a regular lattice. The so-called D3Q19 lattice was used in this work, where “D3” indicates three dimensions, and “Q19” indicates a 19-dimensional space with corresponding velocity vectors $\mathbf{e}_{\sigma,i}$ ($i = 0, 1, \dots, 18$).

The evolution of the fluid particle distributions is governed by the discrete Boltzmann equation [106]:

$$\mathbf{f}(\mathbf{x} + \mathbf{e}, t + 1) - \mathbf{f}(\mathbf{x}, t) = \mathbf{S} \left[\mathbf{f}^{(\text{eq})}(\mathbf{x}, t) - \mathbf{f}(\mathbf{x}, t) \right], \quad (2.3)$$

where the bold-face symbols denote Q -dimensional column vectors, e.g.,

$$\mathbf{f}(\mathbf{x}, t) = [f_0(\mathbf{x}, t), f_1(\mathbf{x}, t), \dots, f_{18}(\mathbf{x}, t)]^T$$

is a vector of the distribution functions at lattice location \mathbf{x} and time t . The left-hand side of Eqn. (2.3) represents the advection term, denoting that the fluid particles $\mathbf{f}(\mathbf{x}, t)$ simply propagate in space according to the velocity \mathbf{e} . The right-hand side of Eqn. (2.3) represents the collision term, accomplished by a multiple-relaxation-time (MRT) approximation of the particle distribution functions towards their equilibria via a $Q \times Q$ full collision matrix \mathbf{S} .

Equivalently, one can consider the collision process being carried out in moment space, instead of discrete velocity space. Given a set of discrete velocity vectors \mathbf{e} and corresponding distribution functions $\mathbf{f}(\mathbf{x}, t)$, a vector of moments \mathbf{m}_i ($i = 0, 1, \dots, 18$) can be constructed by a projection of the distributions \mathbf{f} through a linear transformation, i.e.,

$$\mathbf{m} = \mathbf{M} \mathbf{f}; \quad \mathbf{f} = \mathbf{M}^{-1} \mathbf{m},$$

where \mathbf{M} is an integer transformation tensor, constructed via the Gram-Schmidt orthogonalization procedure [197, 106, 198]. The moments are related to the conserved (hydrodynamic) and non-conserved (kinetic) physical properties, including the density, the momentum, the kinetic energy, the energy flux, and the viscous stress tensor. Hence, Eqn. (2.3) can be written as

$$\mathbf{f}(\mathbf{x} + \mathbf{e}, t + 1) - \mathbf{f}(\mathbf{x}, t) = \mathbf{M}^{-1} \widehat{\mathbf{S}} [\mathbf{m}^{(eq)}(\mathbf{x}, t) - \mathbf{m}(\mathbf{x}, t)]. \quad (2.4)$$

The corresponding collision matrix $\widehat{\mathbf{S}} = \mathbf{M} \cdot \mathbf{S} \cdot \mathbf{M}^{-1}$ in moment space is a diagonal matrix:

$$\begin{aligned} \widehat{\mathbf{S}} = \text{diag}(0, s_1, s_2, 0, s_3, 0, s_3, 0, s_3, s_4, s_5, s_4, s_5, \\ s_6, s_6, s_6, s_7, s_7, s_7) \end{aligned} \quad (2.5)$$

where s_i are the collision (or relaxation) parameters, indicating that the collision process for each moment m_i is accomplished by a linear relaxation towards its equilibrium $m_i^{(eq)}$. The transformation tensor \mathbf{M} and the functional forms of the equilibrium moments $\mathbf{m}^{(eq)}$ for the D3Q19 lattice are given in [197, 106].

The values of the collision parameters s_i that correspond to the conserved moments are irrelevant because $m^{(eq)}(\mathbf{x}, t) = m(\mathbf{x}, t)$ for the conserved moments; here we set them to be zero. Also, some of the collision parameters are set to be identical values to preserve symmetry on the chosen lattice. The kinematic viscosity ν is then defined as

$$\nu = \frac{1}{3} \left(\frac{1}{s_4} - \frac{1}{2} \right) = \frac{1}{3} \left(\frac{1}{s_6} - \frac{1}{2} \right). \quad (2.6)$$

Note that the conventional BGK single-relaxation-time model is a special case of the generalized LB-MRT model, where the collision matrix is $\mathbf{S} = (1/\tau) \mathbf{I}$. Here $\tau = 1/s_4$ is the single relaxation time and \mathbf{I} is the identity matrix.

2.3.2 Two-phase LB model

A Shan-Chen multi-component LB model [268] was used in this work. We provide a short description of the model below, and we refer readers to our

previous work [241] for additional details. The evolution equation for fluid k (wetting or nonwetting fluid) is

$$\mathbf{f}_k(\mathbf{x} + \mathbf{e}, t + 1) - \mathbf{f}_k(\mathbf{x}, t) = \mathbf{M}^{-1} \widehat{\mathbf{S}}_k \left[\mathbf{m}_k^{(eq)}(\mathbf{x}, t) - \mathbf{m}_k(\mathbf{x}, t) \right]. \quad (2.7)$$

The macroscopic fluid density ρ_k , fluid velocity \mathbf{v}_k and common velocity \mathbf{v} are obtained by

$$\begin{aligned} \rho_k(\mathbf{x}, t) &= \sum_i f_{\sigma,i}^k(\mathbf{x}, t), \\ \mathbf{v}_k(\mathbf{x}, t) &= \sum_i f_{\sigma,i}^k(\mathbf{x}, t) \mathbf{e}_{\sigma,i} / \rho_k(\mathbf{x}, t), \\ \mathbf{v}(\mathbf{x}, t) &= \sum_k (\rho_k \mathbf{v}_k s_{4,k}) / \sum_k (\rho_k s_{4,k}). \end{aligned}$$

To simulate multiphase flow in porous media, long-range interactions of the form

$$\mathbf{F}_k = \mathbf{F}_{k,f-f} + \mathbf{F}_{k,f-s} + \rho_k \mathbf{g}_k \quad (2.8)$$

are included, where $\mathbf{F}_{k,f-f}$ is the fluid-fluid interaction force, $\mathbf{F}_{k,f-s}$ is the fluid-solid interaction force, and $\rho_k \mathbf{g}_k$ is the gravitational force for fluid k . Note that one can choose arbitrary values for the gravitational coefficient \mathbf{g}_k to replace the desired fluid pressure gradient, which simplifies the handling of boundary conditions.

The change in momentum due to interaction forces \mathbf{F}_k is included in the equilibrium function $\mathbf{m}_{i,k}^{(eq)}(\rho_k, \mathbf{v}_k^{eq})$, where $\rho_k \mathbf{v}_k^{eq} = \rho_k \mathbf{v} + \mathbf{F}_k / s_{4,k}$ [213]. In the model, nearest neighbor interactions are used to define the inter-particle forces. The fluid-fluid interaction force $\mathbf{F}_{k,f-f}$ on fluid k at site \mathbf{x} is the sum of the forces between the fluid k particle at \mathbf{x} , and the fluid k' particles at neighboring sites \mathbf{x}' , given as

$$\mathbf{F}_{k,f-f}(\mathbf{x}) = -\psi_k(\mathbf{x}) \sum_{\mathbf{x}'} G(\mathbf{x}, \mathbf{x}') \psi_{k'}(\mathbf{x}') (\mathbf{x}' - \mathbf{x}) \quad (2.9)$$

where $\psi_k(\rho_k)$ is a function of local density and for simplicity $\psi_k(\rho_k) = \rho_k$ is used in this study. In Eqn. (2.9), G represents the strength of the interpartical force. By choosing G properly, fluids can separate so that immiscible multiphase flow behavior motivated by interfacial tension can be produced [271].

The interaction force $\mathbf{F}_{k,f-s}$ between the fluid k at site \mathbf{x} and the solid at site \mathbf{x}' is defined as

$$\mathbf{F}_{k,f-s}(\mathbf{x}) = -\rho_k(\mathbf{x}) \sum_{\mathbf{x}'} G_{ks}(\mathbf{x}, \mathbf{x}')(\mathbf{x}' - \mathbf{x}). \quad (2.10)$$

Again, one can choose the sign and the magnitude of coefficient G_{ks} to distinguish the different wetting preferences of pure fluids. Detailed descriptions for choosing these coefficients for the fluid-fluid and fluid-solid interaction forces in the multiphase LB model were discussed in our previous work [241]. The overall fluid momentum is defined as [270]:

$$\rho \mathbf{u} = \sum_k \sum_i f_{\sigma,i}^k \mathbf{e}_{\sigma,i} + \frac{1}{2} \sum_k \mathbf{F}_k, \quad (2.11)$$

where \mathbf{u} is the overall fluid velocity, and $\rho = \sum_k \rho_k$ is the total density of the fluids.

The LB method is a computationally intensive approach. As a result, an efficient parallel algorithm and implementation are critical for large-scale multiphase LB simulations. In this work, we adapted a LB implementation approach proposed by Pan et al. [243], which utilizes an orthogonal recursive bisection (ORB) decomposition that leads to excellent parallel efficiency by maintaining an efficient workload balance among subdomains.

2.4 Model Validation

2.4.1 Comparison between BGK and MRT model

In the LB method, no-slip velocity boundary conditions are usually approximated using the bounce-back scheme, which mimics the phenomenon that a particle reflects its momentum in some way when colliding with a solid surface. However, the actual position of a boundary is viscosity dependent when applying the BGK model [134, 242]. While in the MRT model, the viscosity dependence can be eliminated by individually adjusting the collision parameters.

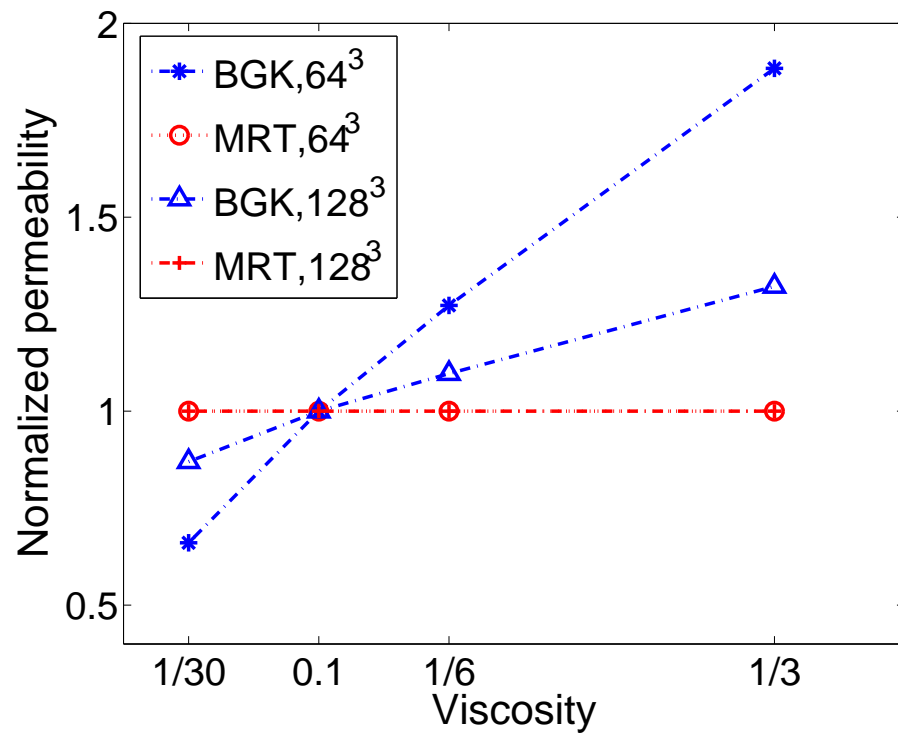


Figure 2.1: (Color online) Comparison of the measured permeability of a sphere-pack porous medium as a function of fluid viscosities using BGK and MRT models. The permeability results are normalized with respect to the value at $\nu = 0.1$.

In order to illustrate the benefit of the MRT model over its BGK counterpart, we performed a test for single-phase flow through a homogeneous sphere-pack porous medium, labeled as GB1b. The porosity of the GB1b medium was 0.36 and the relative standard deviation of the spherical grain size was 10.1%; more properties of the GB1b medium were given in [241]. We used a subset of the entire GB1b sphere pack and discretized it using a $64 \times 64 \times 32$ lattice. A mirror image was created along the flow direction to enforce periodic boundary condition. The resulting medium contained about 150 spheres with 64^3 lattice nodes, corresponding to 13 lattice nodes per average sphere diameter. This discretization level was chosen based upon our previous investigations [241], which showed that for the same sphere-pack porous medium, the simulated relation curve between capillary-pressure and saturation in a NAPL-water flow system approaches convergence if the number of lattice nodes per average sphere diameter $\zeta \geq 13.0$.

In the MRT model, s_4 and s_6 were determined based on Eqn. (2.6), and following the analysis by Ginzburg and d’Humières [134], we used

$$s_1 = s_2 = s_5 = s_4, \quad s_3 = s_7 = 8(2 - s_4)/(8 - s_4) \quad (2.12)$$

in order to minimize the permeability dependence on viscosity. By applying a constant body force to the flow through the medium, we calculated the steady-state Darcy velocity and estimated the saturated permeability of the medium with respect to different fluid viscosities (i.e., $\tau = 0.6, 0.8, 1.0, 1.5$) using both the MRT and BGK models. As shown in Figure 2.1, the simulated permeability obtained by the BGK model increases significantly with increasing viscosities, although refining the discretization to 128^3 mitigated the level of dependence. We observed that the permeabilities obtained by the MRT model remained essentially constant for both the 64^3 and 128^3 discretization levels when the viscosity changed by a factor of 10. Therefore, compared to BGK models, MRT models are more suitable for application to multiphase flow systems, where fluids of varying viscosities are present simultaneously, and where applying fine enough discretiza-

tion of pore geometries to achieve the desired accuracy is often computationally impractical.

2.4.2 Two-phase flow in a tube

We further validated the LB multiphase model by considering flows in a simple geometry for which a theoretical solution is available. Our simulation was performed in a three-dimensional tube with a square cross-section, filled with a non-wetting phase (NWP) of viscosity ν_n and a wetting phase (WP) of viscosity ν_w , as shown in Figure 2.2(a). The configuration of the interface between the NWP and WP depends upon the radius of interface R , which is defined by the pressure difference between the fluids.

Semi-analytical approximations of the solution that account for the interfacial stress balance between the NWP and WP were given by Ehrlich [114], who exploited the solution to investigate viscous coupling effects on a bundle of capillary tubes. Axial velocities for the NWP and WP are represented in polar coordinates by the series

$$\begin{aligned} \mathbf{v}_n(r, \theta) &= -\frac{\nabla p_n - \rho_n g_n}{\mu_n} \left(-\frac{r^2}{4} + a_0 + \sum_{j=1}^{\infty} [a_j r^{sj} \cos(sj\theta)] \right), \\ \mathbf{v}_w(r, \theta) &= -\frac{\nabla p_w - \rho_w g_w}{\mu_w} \left(-\frac{r^2}{4} + b_0 + \sum_{j=1}^{\infty} [(b_j r^{sj} + c_j r^{-sj}) \cos(sj\theta)] \right) \end{aligned} \quad (2.13)$$

where $\mathbf{v}_{i,(i=n,w)}$ is the fluid velocity of the NWP/WP phases along the flow direction, μ_i is the dynamic viscosity, s is the number of the sides of the cross section in polygon tubes (which is 4 for square cross-sections), and a_j , b_j , and c_j are the undetermined parameters. The series in Eqn. (2.13) have to be truncated to a finite number at $j = N$ so that a total number of $3N + 2$ unknown parameters ($a_{j,j=0,N}$, $b_{j,j=0,N}$ and $c_{j,j=1,N}$) need to be determined. We truncated the series at $N = 15$, which led to a sufficiently small convergence error, according to the results reported in Ehrlich [114]. Hence, we solved for 32 unknown a 's, b 's, and

c 's from 32 equations constructed by applying a zero velocity boundary condition at the tube wall, and continuity of velocity and a stress balance across the NWP-WP interface. We compared the velocity field obtained at $N = 15$ with that obtained at $N = 20$, and found that the L_2 norm of the difference between the two solutions was less than 6×10^{-8} , which confirmed the convergence of the velocity field.

In the LB simulation performed to compare to this analytical solution, the fluid-fluid interaction coefficient $G_{k'k}$ was set to 0.001, determined from a simple bubble test (see details in [241]) such that the desired phase separation was produced. The fluid-solid interaction coefficients G_{ks} were set to zero because the interactions between both fluids and the wall were neglected in the analytical solution. Initially, both the NWP and WP were placed within the tube as shown in Figure 2.2(a); the system was allowed to reach steady state after the body forces were imposed for both fluids. Periodic boundary conditions were applied in the x direction along the channel length, and steady state was considered to be achieved when the following criterion was satisfied:

$$\frac{\sqrt{\sum_{\mathbf{x}} [u_x(\mathbf{x}, t) - u_x(\mathbf{x}, t - 50)]^2}}{\sqrt{\sum_{\mathbf{x}} u_x(\mathbf{x})^2}} < 10^{-5} \quad (2.14)$$

where u_x is the overall fluid velocity [defined in Eqn. (2.11)] along the flow direction x .

Figure 2.2(b) plots the steady-state profile of v_x in the middle plane of the channel with a radius of interface $R = 10$, body forces $g_n = g_w = 10^{-4}$, and a viscosity ratio $M = \nu_n/\nu_w = 2$. A good agreement between the LB simulation and the analytical solution is illustrated in Figure 2.2(b) using 32^2 lattice nodes in the y - z cross-section. To further evaluate the difference between the numerical LB solution and the semi-analytical solution, we calculated the L_2 norm error of velocity field, defined as

$$E_2 = \sqrt{\frac{\sum_{\mathbf{x}} [v_x(\mathbf{x}) - v_x^*(\mathbf{x})]^2}{N_l^3}}, \quad (2.15)$$

where v_x^* is the Ehrlich’s semi-analytical solution defined in Eqn. (2.13), and N_l^2 is the number of lattice nodes in the y - z cross-section. We observed a second-order rate of convergence for single-phase flow, whereas for coupled two-phase flow at $M = 2$, we obtained an order of convergence of 1.4, which we calculated using linear regression to fit E_2 with respect to N_l in log space. The lower order of convergence for the coupled two-phase flow case was expected because of the interfacial effect caused by the steep gradient in density across the fluid-fluid interface [228, 68]. We have observed similar rates of convergence for two-phase flow in a tube with M up to 5.

2.5 Two-phase Flow Simulations in Porous Media

2.5.1 Setup of the numerical system

We used the identical porous medium and discretization approach detailed in §2.4.1. To determine if our simulations were adequately resolved, we made spot checks by comparing the simulated relative permeabilities with 64^3 lattice nodes to a finer discretization with 96^3 lattice nodes and found that at the same saturation level the variation of the relative permeabilities between the two discretization levels for both fluid phases in the conventional model was within 5% in all cases.

We first determined the saturated permeability κ of the medium, which was calculated from a steady-state Darcy’s velocity after applying a constant body force for one phase and setting the density of the other fluid equal to zero at all locations. It is important to note that the MRT model yields more accurate predictions of both saturated and relative permeabilities than the standard BGK model, which inherently has a relaxation-time dependent location of the no-slip boundary and thus leads to a viscosity dependent permeability.

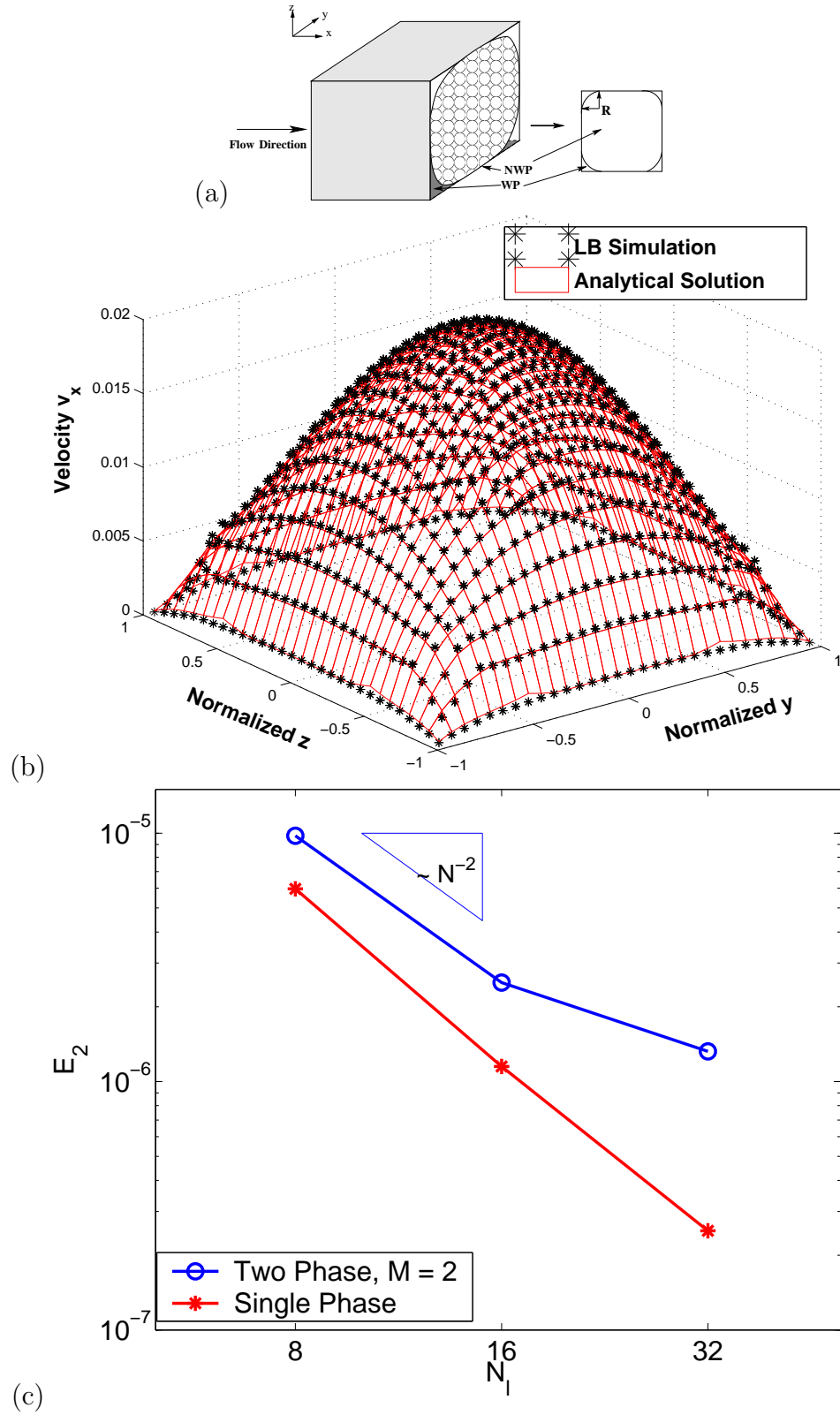


Figure 2.2: (Color online) (a) Two-phase flow in a channel with square-shaped cross-section; (b) Cross-sectional velocity profile for a phase viscosity ratio $M = 2$ with 32^2 lattice nodes along the y - z plane; and (c) Error of the simulated velocity v_x profile with respect to the semi-analytical solution versus lattice size N_l for single-phase flow and two-phase flow with a viscosity ratio $M = 2$.

Simulation of immiscible two-fluid-phase flow was performed as follows:

- Initially, both a NWP and WP of equivalent density were uniformly-distributed throughout the medium such that the desired WP saturation (denoted as S_w) was obtained;
- The medium was bounded by walls along the y and z directions and a periodic boundary condition was applied along the x direction;
- Co-current flow was simulated by adding body forces, as defined in Eqn. (2.8), for both fluids along the flow direction. The reasons for using body forces instead of imposing a pressure gradient as a driving force are that: (1) using body forces can avoid capillary pressure gradients and thus saturation gradients along the flow direction; and (2) body forces are convenient to implement, since periodic boundary conditions can then be applied along the flow direction; and
- The fluid-fluid interaction coefficient G and fluid-solid coefficients G_{ks} were chosen such that the fluids with an assigned viscosity ratio were separated and the desired wettabilities were achieved [241]. For example, in a neutrally water-wet (NWW) system, the WP-solid and NWP-solid interaction coefficients were set to be -0.01 and 0.01, corresponding to a contact angle of approximately 65° , while in the strongly water-wet (SWW) system, those coefficients were set to be -0.02 and 0.02, corresponding to a contact angle of approximately 25° .

The conventional permeabilities for the NWP and WP were calculated following the extension of Darcy's law defined in Eqn. (2.1). In order to calculate the four generalized permeability coefficients, one set of steady-state data is insufficient. Therefore, a second set of steady-state simulations was performed by perturbing the body force of the NWP by 20% of that used in the first set, while keeping the same body force for the WP. These conditions were important to provide similar flow conditions, yet sufficiently different conditions to allow

determination of the four generalized permeability coefficients with sufficient accuracy.

In the following section, we first investigate the effects of capillary number, wettability, and viscosity ratio on the conventional permeabilities of fluids. We also calculate the generalized coefficients and investigate whether the generalized coefficient matrix is symmetric or non-symmetric. Lastly, we investigate the correlation of the relative permeabilities as a function of the interfacial area.

2.5.2 Results and discussion

2.5.2.1 Effect of capillary number

We first show the dependence of the relative permeability on capillary number Ca , which describes the ratio of viscous forces to capillary forces:

$$Ca = v_w \mu_w / \gamma. \quad (2.16)$$

The non-dimensional interfacial tension γ can be obtained using Laplace's law by means of a bubble simulation [241]. Figure 2.3 compares a series of snapshots of the NWP motion under two capillary numbers 5×10^{-4} [Figure 2.3(a)–(d)] and 5×10^{-5} [Figure 2.3(e)–(h)]. The corresponding Reynolds numbers of the WP

$$Re = \rho_w v_w D / \mu_w \quad (2.17)$$

were 0.17 and 0.017, respectively, indicating a Darcy flow regime. In Eqn. (2.17), D is the average diameter of solid grain in the medium.

For both cases, the driving force for the NWP was kept constant while the force for the WP in Figure 2.3(a)–(d) was one order of magnitude larger than that in Figure 2.3(e)–(h). The saturation of the NWP for both cases was 6%, which allowed us to track dynamically the movement of individual NWP regions. As illustrated in Figure 2.3, the NWP was in the form of disconnected ganglia and trapped in big pores due to the resistance of capillary forces. At higher Ca ,

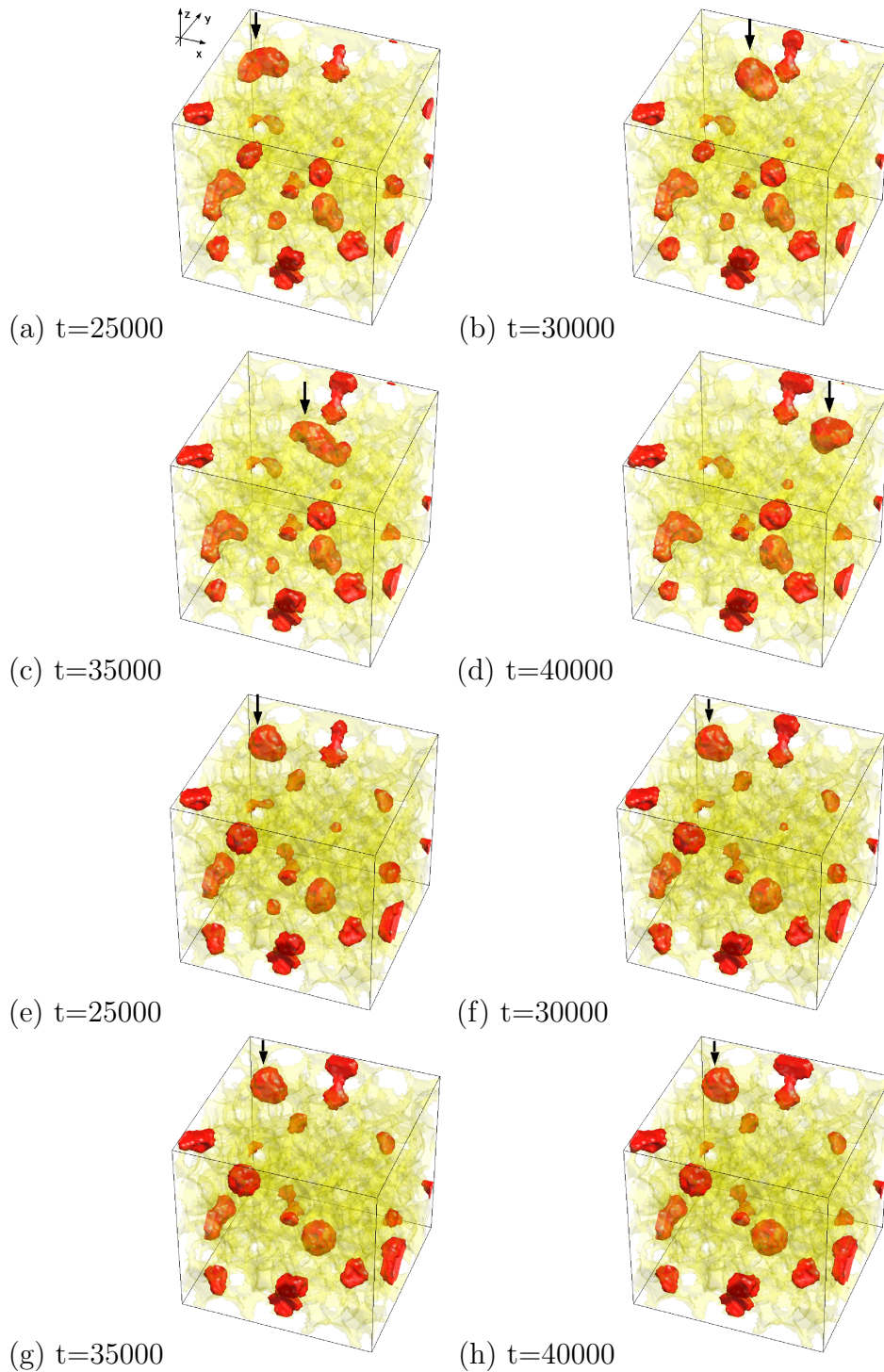


Figure 2.3: (Color online) Snapshots of the non-wetting phase distribution under a higher capillary number [$Ca = 5 \times 10^{-4}$, (a)–(d)] and a lower capillary number [$Ca = 5 \times 10^{-5}$, (e)–(h)]. The NWP region indicated by the arrow in (a) moves through the porous medium driven by momentum transferred from the WP at higher Ca , while it is unable to move at lower Ca .

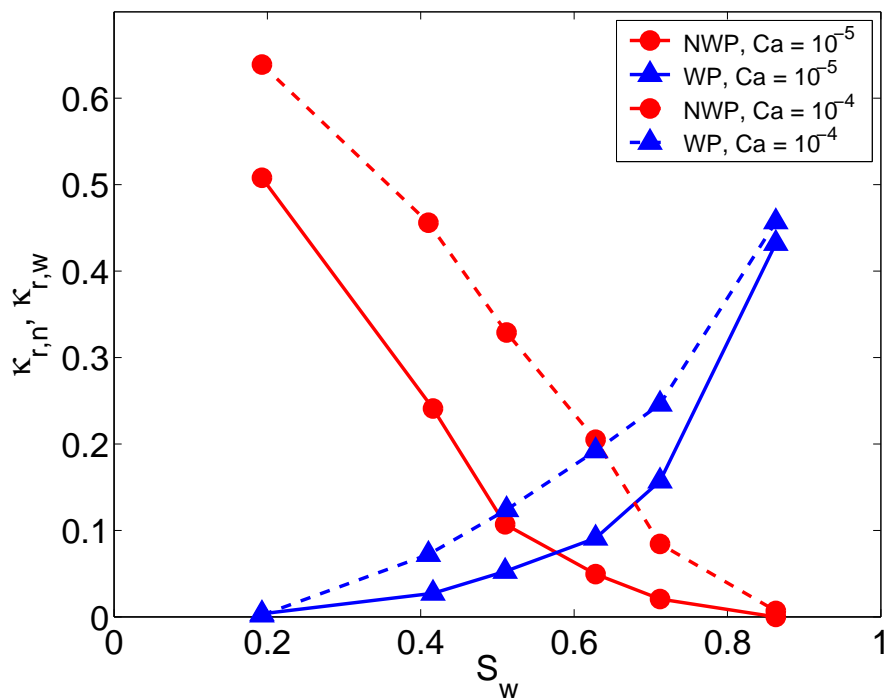


Figure 2.4: (Color online) Relative permeability vs. WP saturation S_w for co-current two-phase flow with different Ca in a neutrally wet medium at $M = 1$.

we observed the motion of disconnected NWP regions that had overcome the capillary resistance to movement. For example, the movement of a NWP region initially in the upper left of Figure 2.3(a) was observed. However, this motion was undetectable in case of a lower Ca [see Figure 2.3(e)–(h)], although in both cases the driving body forces applied to the NWP were the same.

Strictly speaking, this is not a conventional steady-state scenario, although the macroscopic saturation and flow rates of both phases remain constant. The dynamic equilibrium of a moving disconnected NWP phase in “steady state” was first observed by Avraam et al. [16]. It is obvious that there is an interfacial momentum transfer from the WP, engulfing the disconnected NWP, to the NWP, which results in the mobilization of the disconnected NWP at higher Ca .

The influence of Ca on the conventional relative permeabilities is shown in Figure 2.4, in which two levels of Ca ’s ($Ca = 10^{-4}$ and $Ca = 10^{-5}$) were com-

pared in a neutrally wet porous medium. The body forces of the WP and NWP were kept equal ($g_n = g_w$) and were adjusted according to the WP velocity in order to achieve the desired Ca . This is similar to the way that the experiment by Avraam and Payatakes [19] was performed in glass pore networks. We found that both the NWP and WP permeability coefficients were increasing functions of Ca for the fluid system. This trend was also observed by Avraam and Payatakes [19] experimentally and by Langaas and Papatzacos [200] numerically.

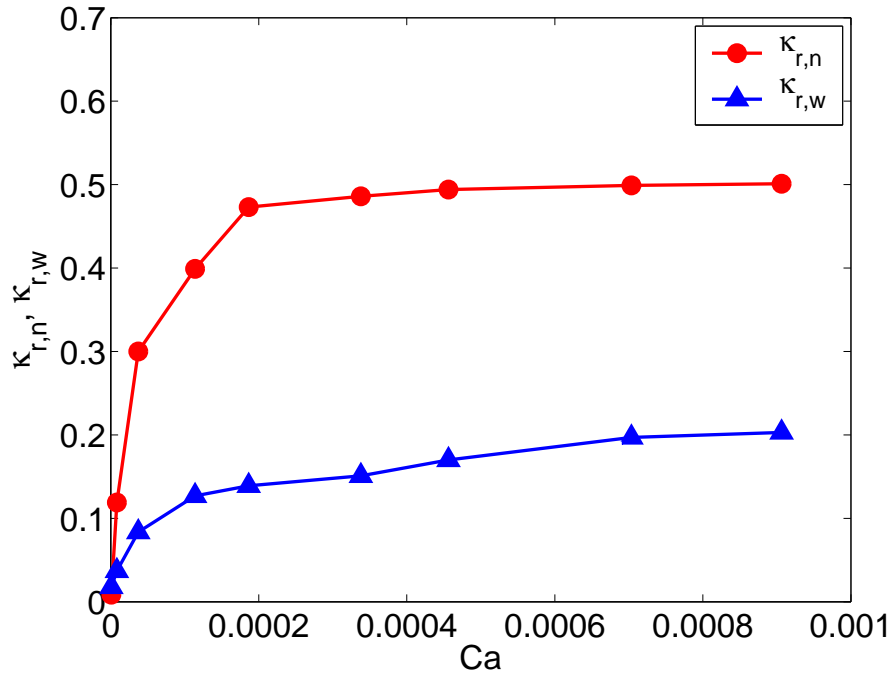


Figure 2.5: (Color online) Relative permeabilities as a function of Ca for co-current, two-phase flow with $M = 1$ and $S_w = 0.5$.

In order to further investigate the effect of capillary number, we performed simulations at $S_w = 0.5$ with different level of forcing and hence different Ca . Figure 2.5 shows that when Ca is 10^{-4} or smaller, the flow rate and the driving force exhibit highly nonlinear relations for both phases; while when Ca approaches 10^{-3} , the relative permeabilities are almost constant, indicating linear flows at high levels of forcing. This finding agrees with Gunstensen and Rothman [149], despite differences between the porous media investigated and the LB

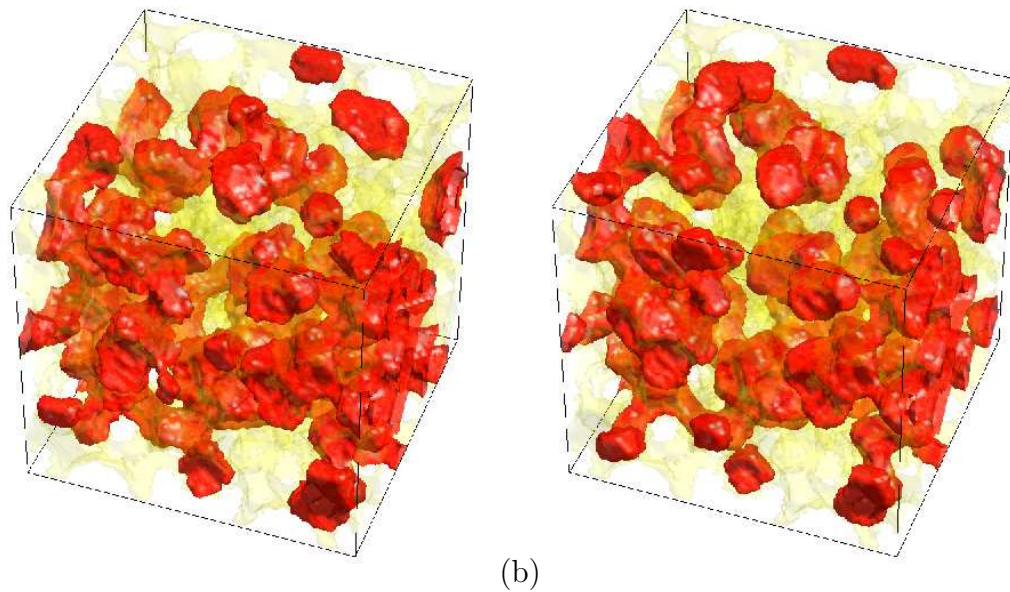


Figure 2.6: (Color online) Steady-state distributions of the NWP (a) a neutrally wet medium; and (b) a strongly water-wet medium. Wetting-phase saturation $S_w = 0.509$ in (a) and 0.508 in (b). Dark gray (red online) regions represent the non-wetting fluid, and light gray (yellow online) regions represent the solid phase. For clarity of illustration the wetting fluid is not shown.

simulators used. We note natural hydrologic two-phase flow systems are almost universally in the nonlinear regime because typically $Ca \ll 10^{-4}$.

2.5.2.2 Effect of wettability

Next, we studied the dependence of the relative permeability on wettability. Steady-state NWP distributions are illustrated in Figure 2.6 for cases of neutrally water wet (NWW) and strongly water wet (SWW) media. For the case of a SWW medium, the NWP displaces the WP in the largest pores. Thus for the same saturation conditions, the NWP correspondingly occupies a set of larger pores on average for the SWW medium compared to the NWW medium. As a corollary to this observation, the NWP has a larger specific interfacial area with the solid phase, hence greater resistance to flow, in the NWW case than in the SWW case, which is consistent with previous observations [111]. On the other hand, the NWP becomes more disconnected in the SWW medium, as shown

in Figure 2.6. The former mechanism appears to be dominant because the total effect of these factors leads to a higher apparent NWP relative permeability in the SWW system than in the NWW system, as shown in Figure 2.7. In particular, a substantially higher NWP relative permeability was observed in the SWW system than in NWW system at high NWP saturations, where the resistance effect of the solid phase boundary to the movement of NWP clearly outweighs the connectivity effect of the NWP in a SWW medium. This was also observed in experimental work reported in Dullien [110] for dolomite media and Avraam and Payatakes [18] for glass pore networks.

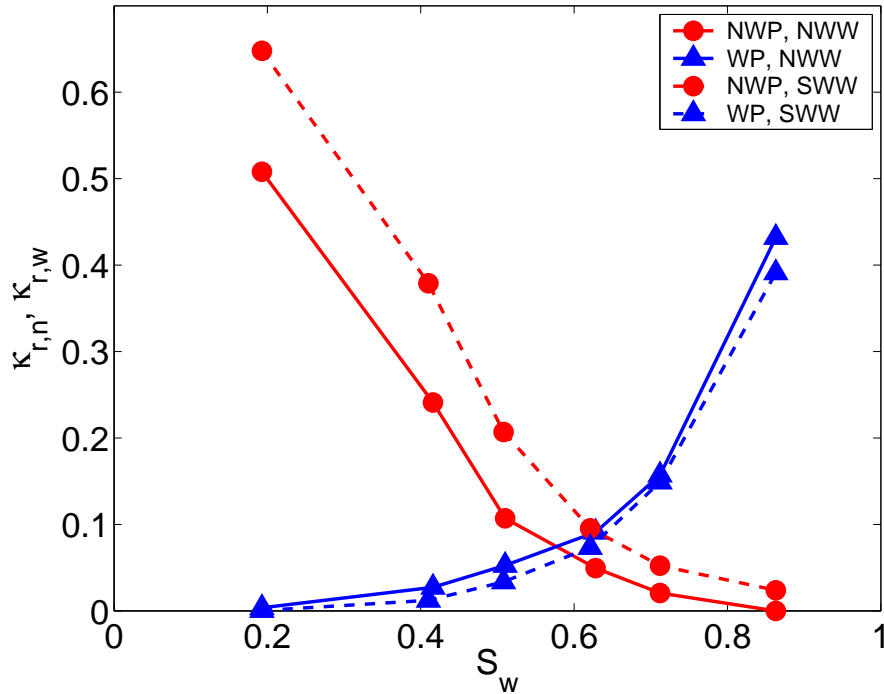


Figure 2.7: (Color online) Relative permeability vs. WP saturation S_w for co-current two-phase flow with different wettability with $M = 1$ and $Ca = 10^{-5}$.

On the other hand, in a SWW system, due to the fact that NWP tends to occupy larger pores, the average size of pore space occupied by the WP is smaller for the SWW system compared to the NWW systems at a given saturation level. This would suggest that the WP relative permeability for a SWW system would be lower than the WP relative permeability in a corresponding NWW system.

However, the WP is more connected in SWW media than in corresponding NWW media. Based upon our observations, the net effect of these two off-setting mechanisms is a relatively small difference in the relative permeability of WP as a function of changes in wettability for the two conditions that we analyzed. This finding is in agreement with the experimental results reported in Avraam and Payatakes [19].

2.5.2.3 Effect of viscosity ratio

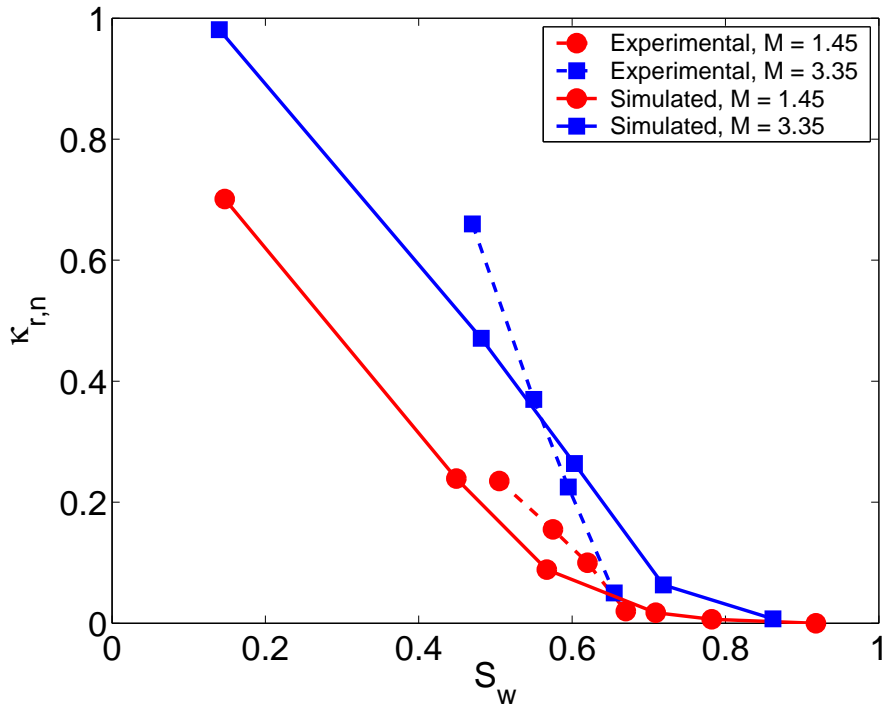


Figure 2.8: (Color online) NWP relative permeability measured by Avraam and Payatakes [18] in a glass pore network with a contact angle of 40° and our simulated results for a NWW system as a function of WP saturation S_w for co-current, two-phase flow with different viscosity ratios at $Ca = 10^{-5}$.

We further studied the dependence of the conventional relative permeabilities on the viscosity ratio between fluid phases. As experimental measurements of relative permeability data on three-dimensional porous medium systems are unavailable, we compared our simulations with Avraam and Payatakes [18]’s work,

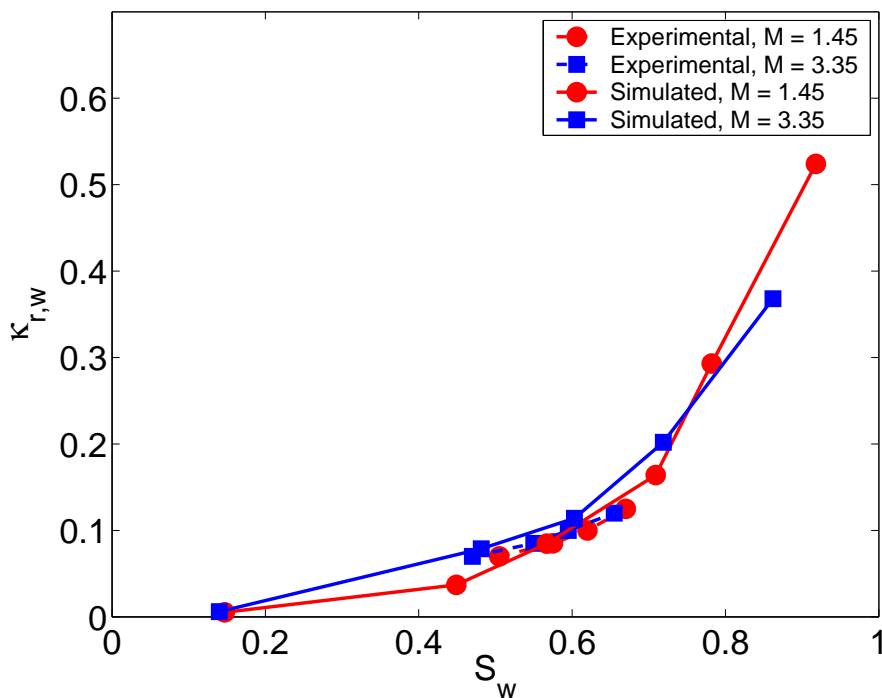


Figure 2.9: (Color online) WP relative permeability measured by Avraam and Payatakes [18] in a glass pore networks with a contact angle of 40° and our simulated results in a NWW system as a function of WP saturation S_w for co-current, two-phase flow with different viscosity ratios at $Ca = 10^{-5}$.

which was performed in a two-dimensional glass pore network. Figure 2.8 and Figure 2.9 show these experimental data along with results of three-dimensional LB simulations used to measure conventional relative permeabilities as a function of WP saturation for two viscosity ratios, $M = 1.45$ and $M = 3.35$. From Figure 2.8, we observe that an increased viscosity ratio M leads to a significantly increased NWP apparent relative permeability, especially when the saturation is in the intermediate range. This is because the WP, which is flowing in relatively small pore size connected paths and edges of the pore space, is strongly coupled to the NWP, which is flowing in the larger regions of the pore structure. As a result, the NWP experiences an apparent hydraulic slip, a so-called “lubricating” effect on the flow of the NWP due to the WP film [110]. The greater the viscosity of the NWP, or the ratio M , the greater the hydraulic slip becomes.

This macroscopic trend in relative permeability can also be due to changes in the NWP distribution as a function of M , as observed experimentally by Avraam and Payatakes [18] in their two-dimensional glass network, in which they found that a higher viscosity ratio favors a more connected NWP pathway and hence greater NWP permeability. It is also consistent with the numerical study done by Langaas and Papatzacos [200]. The different permeability values among investigators are due to differences in capillary numbers among the systems, medium morphology, fluid properties, or dimensionality effects.

On the other hand, the flow of a less viscous WP is effected less by the viscosity of the NWP, therefore the WP relative permeability is relatively insensitive to changes in M . This trend was clearly confirmed by our simulations and the experimental work of Avraam and Payatakes [18], as shown in Figure 2.9.

2.5.2.4 Generalized permeability coefficients

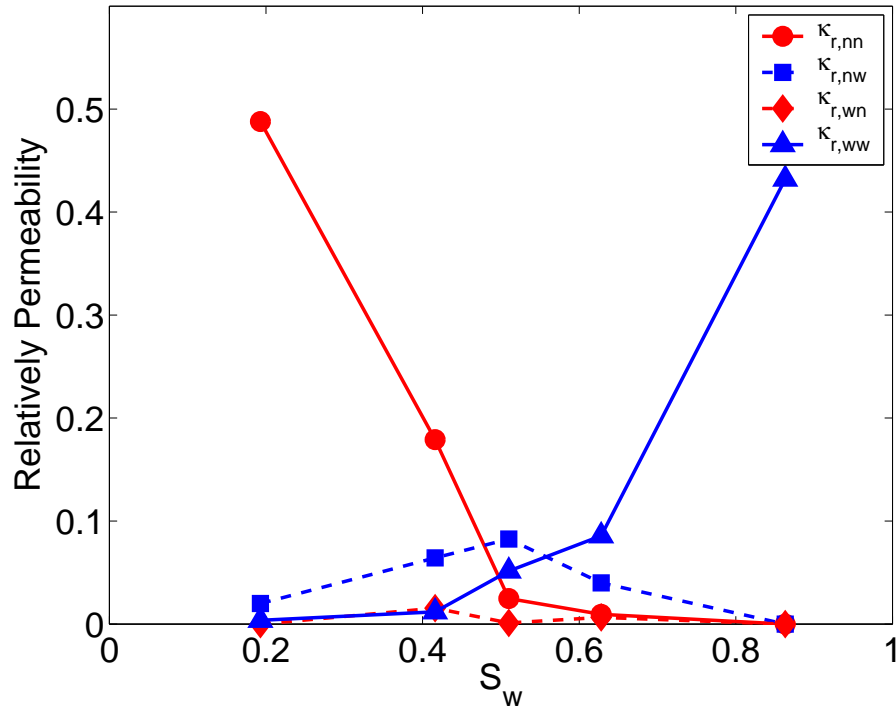


Figure 2.10: (Color online) Generalized relative permeabilities as a function of WP saturation S_w for co-current two-phase flow with $M = 1$ and $Ca = 10^{-5}$.

The generalized permeability coefficients for the NWP and WP were calculated and are shown in Figure 2.10. The magnitude of the $\kappa_{r,nw}$ coupling coefficient is comparable to the diagonal coefficient at intermediate saturations, which indicates that the interfacial viscous coupling in two-phase flow is an important phenomenon. Interestingly, $\kappa_{r,nw} > \kappa_{r,nn}$ for $S_w \geq 0.5$, which we attribute to the disconnected nature of the NWP in this region. This indicates that in such an instance the movement of the NWP phase is assisted by the WP. Since $\kappa_{r,wn} > 0$, this coupling also assists the flow of the WP, but to a significantly lesser extent. We hypothesize that these results are influenced by the distribution of interfacial areas for each of the fluid phases.

We found that the cross coefficients are nonequal and $\kappa_{r,nw}$ is generally greater than $\kappa_{r,wn}$. This provides evidence against the applicability of the Onsager’s theory in two-phase porous medium flow at macroscale. This observation is consistent with the majority of the findings from recent investigations of viscous coupling effects [111, 18, 19]. The non-symmetric cross coefficients are essentially caused by the difference in microscopic morphology and topology of the two fluids. In a SWW system with intermediate saturation, WP predominantly fills the thin channels and small pores that the NWP is not able to enter, while the rest of WP coexists with NWP in wider channels and larger pore spaces. Since the coupling effects only occur at the interfaces between the fluids, the influence of coupling on WP is smaller than that on NWP.

Our results, however, seemingly disagree with the computational study by Gunstensen and Rothman [149], who found that the Onsager reciprocity holds. However, Gunstensen’s numerical experiments were conducted in the linear flow regime (i.e., where $\mathbf{v}_{w/n}$ is a linear function of the forcing) by enforcing high body forces, while our study was performed at $Ca = 10^{-5}$. For this Ca the flow rate and the driving force exhibit nonlinear relations for both phases, as discussed earlier in §2.5.2.1. We verified this by spot-checking the four generalized permeability coefficients at $S_w = 0.5$ with $Ca = 10^{-3}$ using the same approach

outlined in §2.5.1. We found that the coupling coefficients $\kappa_{r,nw}$ and $\kappa_{r,wn}$ differed by only 10% and they were both significant compared to the diagonal coefficients. This suggests that when capillary number is large, the generalized model is a reasonable model and is superior to the conventional Darcy’s law.

The identification of the linear and nonlinear regimes and the dependence of Onsager’s reciprocity on these regimes also indicates that there might be different flow mechanisms dominating the flow phenomena when fluid velocities change significantly. While some studies have attempted to explain these flow mechanisms based on experimental [18, 19] or computational [149] observations, distinction of these mechanisms was based on many flow parameters in the specific media used in these studies and no unified indicator or potential variable has been suggested. We believe further study along this line is important to fully understand the complicated flow phenomena in multiphase porous medium systems.

2.5.2.5 Effect of fluid-fluid interfacial area

We explored the effect of fluid-fluid interfacial area on relative permeabilities. Unlike previous simulations, we removed the solid walls that bound the medium along the y and z directions in order to eliminate the influence of the additional solid-fluid interfaces. Thus, periodic boundary conditions were used in all three directions, although the body force acted only in the x direction. Different spatial distributions of both fluids at a fixed saturation were achieved by initially distributing the fluids in different portions of the medium.

The resulting steady-state distributions of NWP are illustrated in Figure 2.11. In Case 1 (Figure 2.11a), the WP occupied primarily the top half of the medium and the NWP occupied primarily the bottom half; in Case 2 (Figure 2.11b), the NWP was placed in the middle of the medium; while in Case 3 (Figure 2.11c), the NWP was distributed uniformly throughout the medium. At steady state in each configuration, the interfacial area for each configuration was calculated

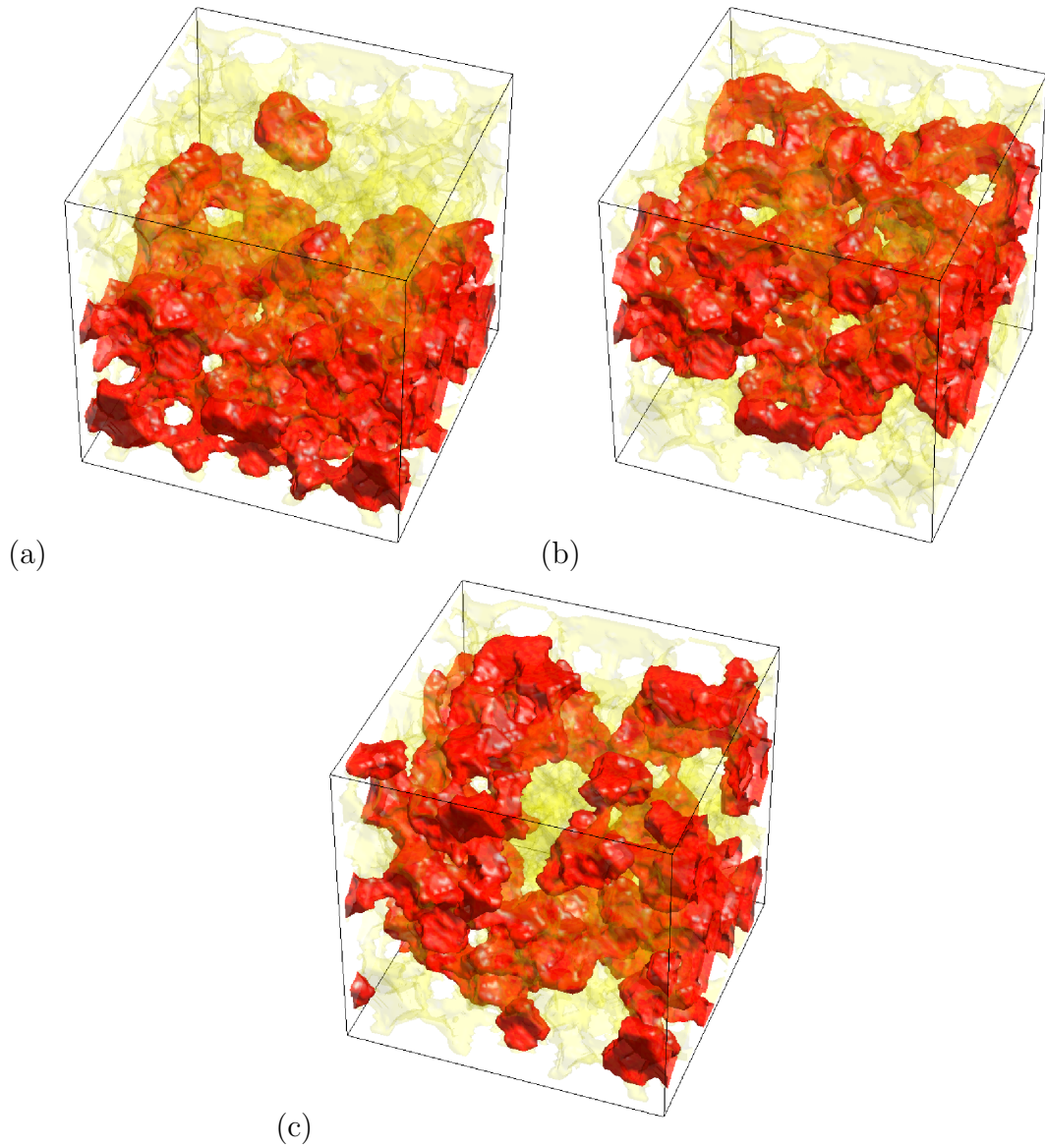


Figure 2.11: (Color online) Steady-state distributions of NWP with different initial phase configurations: (a) Case 1, (b) Case 2, and (c) Case 3. For all cases, the WP saturation is 0.45–0.46.

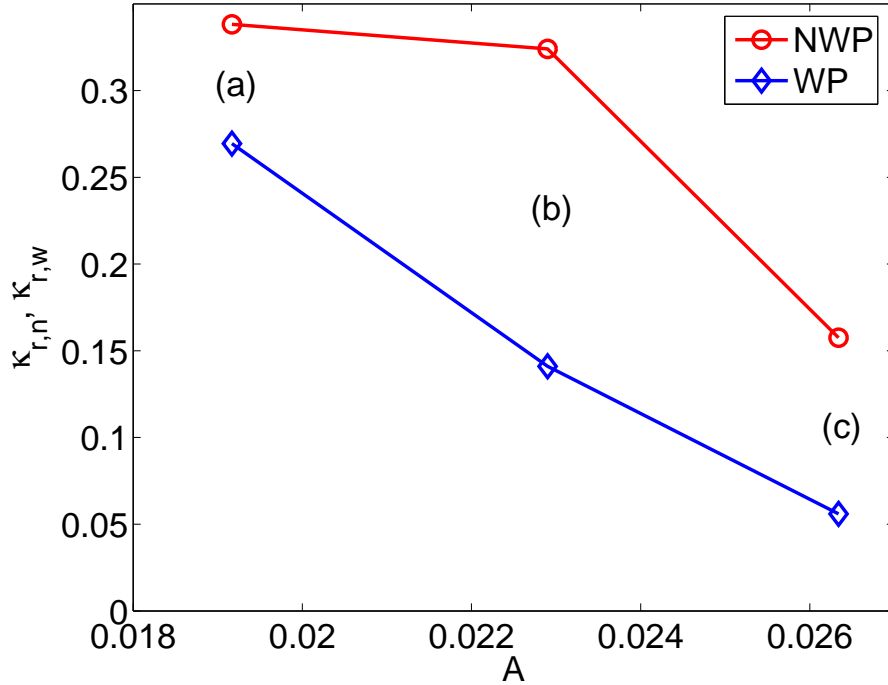


Figure 2.12: (Color online) Conventional relative permeabilities of NWP and WP vs. fluid-fluid interfacial area per unit volume at constant fluid saturations for (a) Case 1, (b) Case 2, and (c) Case 3.

using an MMC algorithm implemented by McClure et al. [215].

As a first attempt to investigate the effects of interfacial area, we evaluated the relation between the conventional relative permeability and interfacial area, holding fluid saturations essentially constant. Figure 2.12 indicates strong correlations between the relative permeabilities for NWP and WP and the fluid-fluid interfacial areas under the same saturation level. In Case 1, WP occupied the top half of the medium and NWP occupied the bottom half; thus generally, each phase flowed as a continuous phase and the interfacial area between the phases was smaller than that in other cases. Therefore, the relative permeability for each phase was higher in Case 1 than that in other cases. In Case 2, NWP still flowed as a continuous but slightly more scattered phase, while WP was divided into top and bottom parts, which led to a larger interfacial area between fluids and hence slightly decreased NWP and significantly decreased WP permeability.

ties. In Case 3, both the NWP and WP were the most disconnected. This was reflected by an increase in the interfacial area. As a result, the NWP and WP relative permeabilities decreased by 50% and 40% compared to Case (b), respectively. The sensitivity of the WP relative permeability with respect to changes in interfacial areas is especially striking. Based on the above results, we believe that interfacial area is an important measure of the morphology and topology of fluid distributions in macroscale porous medium systems, which is not accounted for in either the conventional or generalized relative permeability models. This provides additional evidence for the evolving TCAT approaches, which include interfacial areas as natural quantities in macroscale models [147, 221].

2.6 Conclusions

The LB method is a useful approach for studying the complex behavior of two-fluid-phase flow in porous media. Particularly, the ease of obtaining the local parameters, such as permeability, saturation, and flux, makes it suitable for use in exploring pore-scale physics within porous medium systems. In addition, we believe that the multiple-relaxation-time (MRT) LB models are superior to the BGK models for multiphase flow simulations, due to the fact that the MRT models improve the numerical stability and yield a viscosity-independent velocity field, which is impossible to achieve using the standard BGK models. The investigations of two-phase flow in a channel with a square-shaped cross-section show good agreement with the analytical solution of axial fluid velocities using the LB-MRT model.

Three-dimensional investigations of viscous coupling effects were carried out for two-fluid-phase flow through a sphere-pack porous medium. Viscous coupling effects were found to be important over a broad range of conditions, including capillary number, wettability, and viscosity ratio. Qualitative trends in the change of conventional permeability with the above parameters compare favor-

ably with the experimental results obtained by Avraam and Payatakes [18, 19]. The motion of disconnected NWP regions under higher Ca was captured, which indicates that the prevailing assumption that disconnected parts of a non-wetting fluid phase remain static is invalid under certain conditions.

The dependence of the permeability-saturation curve on the capillary number, wettability, and viscosity ratio provides evidence against the sole dependence of permeability on the corresponding fluid saturation posed in the conventional extended form of Darcy’s law. An attempt to calculate the coupling coefficients in the generalized formulation showed that viscous coupling effects contribute significantly to fluid flow. In addition, those coupling coefficients were found to be unequal, which implies that the Onsager’s reciprocity relation is not applicable for describing multiphase flow in macroscale porous medium systems. We also note that most of our studies were performed for $Ca < 10^{-4}$, as Ca at this range is of practical concern in subsurface systems. Other work found that Onsager theory was valid at higher Ca (still sufficiently low to fall into Darcy flow regime), which was confirmed by our study as well.

The evolving TCAT approach motivated us to further investigate the role of interfacial area for two-phase flow in porous media. A strong dependence of relative permeabilities on fluid-fluid interfacial area was found. For a fixed saturation level, different flow topologies resulted in significantly different relative permeabilities. This suggests that the distinguishing feature of multiphase flow systems—the existence of fluid-fluid interfaces, should be accounted for explicitly in a more complete model formulation. New models that overcome the deficiencies of the conventional and generalized theories deserve further study.

Chapter 3

Local Discontinuous Galerkin Approximations to Richards' Equation

3.1 Introduction

RE is the most common model used to describe water flow in the vadose zone and perhaps the most popular model used to describe flow in multiphase porous medium systems in general. RE is also of interest because while formally a parabolic partial differential algebraic equation (PDAE) model, it can yield solutions with sharp fronts in space and time under certain auxiliary conditions. In such cases, traditional solution methods often fail to converge and exhibit a general lack of efficiency. For this reason, RE serves as an excellent example problem, which can be used to advance numerical solution approaches for difficult systems of PDAE's that arise from nonlinear conservation equations.

Because of the importance of RE, it has been the focus of considerable attention over the last decade with the aim of developing more robust—meaning reliable—and more efficient—meaning reduced computational work to achieve a fixed level of accuracy—solution schemes. Advances have proceeded on reliable

and efficient time integration techniques [281, 222, 188, 191], spatial discretization methods [41, 120, 294, 123], and nonlinear and linear solvers [245, 202, 282, 124]. Through this work, the method of lines (MOL) has emerged as a standard technique for approximating RE [281]. The MOL approach formally decouples the spatial and temporal approximations, which facilitates the application of mature, adaptive time integration methods. Solution approaches based upon variable order, variable step-size time integration have been developed for various spatial discretization approaches, resulting in substantial improvements in robustness and efficiency compared to standard, low-order temporal approximations [191, 124, 217]. Recently, the reduction in computational effort for solving RE due to the combination of these and other algorithmic and method advancements was found to be on par with advancements due to improved computational resources over the last decade [218].

Time integration, along with nonlinear and linear solver aspects of solving RE are more mature than spatial discretization methods. On the other hand, the coupling of advanced spatial and temporal discretization approaches seems to be fertile ground for advancement. In particular, the efficient resolution of sharp fronts in space is important because time integration methods have matured to the point where it is common for spatial error to dominate temporal error. Because of the very sharp fronts that can exist with RE, reducing spatial error requires resolution of the spatial discretization in the vicinity of such features. Concomitantly, smooth regions of the spatial domain may be most economically approximated using relatively coarse discretization and higher order methods.

Discontinuous Galerkin (DG) methods are an evolving class of spatial discretization approaches that have significant promise for improving the efficiency of spatial approximations for difficult nonlinear problems, such as RE. This is so because DG methods are locally conservative, easily support local refinement of both h and p types, and are readily extensible to multiple spatial dimensions. Among DG methods for elliptic and parabolic problems, the local DG (LDG)

method [87] has received considerable attention, including analysis of consistency and stability [87, 14], and application to a wide range of physical problems including compressible flow [26], incompressible flow [82], contaminant transport in porous media [7, 98, 75, 76], and the Korteweg-deVries equations [297, 274].

The significant work accomplished on LDG methods notwithstanding, these efforts have not focused on difficult, highly nonlinear parabolic equations; RE has not been solved with LDG methods to the best of our knowledge. Furthermore, the implicit temporal approximations that have been combined with DG spatial discretizations have typically been backward Euler [254]. The combination of the LDG method with higher order methods in time appears promising territory for additional advances.

Our primary goal is to develop robust and efficient numerical approximations to RE and, more generally, nonlinear parabolic systems of PDAE's arising from conservation equations. The specific objectives of this work are (1) to formulate a mass conservative LDG-MOL approximation to RE based upon a higher order temporal discretization; (2) to derive an efficient solution algorithm for the discrete approximation; (3) to examine a set of alternative LDG-MOL solution approaches; (4) to evaluate the accuracy and robustness of the approximate solutions for a range of test problems; (5) to recommend a solution approach based upon the analysis performed; and (6) to recommend additional steps that might yield further improvements for solving RE.

3.2 Background

3.2.1 Overview

We seek an approach for the solution of RE that faithfully produces an approximation with the desired accuracy for the minimum computational effort necessary. This computational effort is often assumed to scale linearly with the

size of the spatial and temporal domain, although most approaches fall far short of this goal. However, if the number of unknowns required grows sub-linearly with the size of the domain, then so too will the optimal scaling. For numerical solutions to RE, several sources of error exist: spatial truncation, temporal truncation, nonlinear solver, linear solver, and roundoff error. To advance toward the optimal solution strategy, the dominant source of error should be reduced. The dominant source of error for solutions to RE problems that involve sharp fronts is frequently spatial truncation error, if state-of-the-art methods are used for all solution components [281, 31, 124, 217]. With this focus in mind, we first consider current approaches for solving RE, and then address spatial discretization approaches that have the promise of supporting the advances we desire.

3.2.2 Approximation of RE

Attractive methods for solving RE must be robust, which means the approaches used should converge reliably across a broad range of discretizations. While robustness is a prerequisite for an effective RE solution approach, efficiency — meaning the computational effort required to achieve a given level of accuracy — is often the focus of modern research. Robustness and efficiency have proven to be surprisingly elusive for RE. The difficulties experienced have a number of causes, including highly nonlinear, non-smooth closure relations, and corresponding ill-conditioned Jacobians for some formulations. Several strategies for addressing these difficulties and improving robustness and efficiency include model formulation approaches [59, 191, 152], improved time integration methods [281, 188, 191, 124, 217], variable transformations [293], spline approximation of closure relations [260, 222], robust nonlinear solvers [202, 282, 276, 189], scalable linear solvers [282], and local spatial grid refinement approaches [1, 261, 138]. As a result of these advancements, it is currently expected that a solution to RE can be attained for very coarse spatial discretizations. Moreover, a subset of these advancements was shown to have dramatically improved efficiency over the last

decade [218].

3.2.3 Spatial discretization approaches

Improved spatial discretizations are a key component needed to advance more efficient approximations of RE. The spatial discretizations commonly used for RE are low-order finite difference [e.g., 282, 188, 295] or finite element methods [e.g., 59, 275, 181, 202]. However, finite difference methods are not well suited to irregular grids, and standard conforming finite element methods can exhibit significant local mass-balance error [59, 181, 123, 273]. Standard conforming finite element methods also produce non-physical oscillations when applied to problems with sharp fronts without lumping/diagonalization of the mass matrix [59, 244, 181]. In addition, when used for spatially adaptive discretizations, standard conforming finite element methods can result in hanging nodes.

In response to the shortcomings associated with these standard approaches, control volume finite elements [128], mixed finite element methods (MFEMs) [63, 11, 66, 65, 101, 41, 299, 294], and post-processing of pressure fields obtained from conforming finite element methods [90, 112] have been investigated. MFEMs have shown benefits in comparison with both conforming finite element based approximations [225, 175] and control volume finite elements [112], and have been combined with higher order adaptive time integration [123, 220]. However, standard MFEMs require hybridization to avoid indefinite linear systems [230], and higher order mixed spaces can be difficult to construct [13].

3.2.4 Discontinuous Galerkin methods

Over the last 15 years, DG finite element methods have received increasing attention in many fields for hyperbolic PDE's [85, 84, 77, 86] as well as elliptic and parabolic problems [29, 30, 233, 255, 254, 87, 81, 121]. The term discontinuous Galerkin covers a wide range of finite element methods based on discontinuous

approximations. While DG methods have been applied in either space or time [180, 115, 116, 119], we here focus on DG spatial discretizations. In the scope of elliptic or parabolic problems, this rich class of methods includes the method proposed by Bassi and Rebay [26], the LDG method [87], the method of Baumann and Oden [29, 30], and the so-called non-symmetric interior penalty Galerkin method [255, 254].

The evolution of these methods has followed two major themes: methods inspired by the original interior penalty method and those inspired by finite volume techniques for hyperbolic problems, including the LDG method. Since the LDG method for second-order elliptic and parabolic problem rewrites the original problem as a system of first-order equations by introducing an auxiliary variable, it can be thought of as an MFEM approach. Not surprisingly, it shares desirable properties of mixed methods, such as producing locally mass-conservative velocity fields. However, unlike standard MFEMs, the auxiliary variable can be eliminated from the system by suitably choosing the traces of the fluxes across the element interfaces. Moreover, unlike control volume finite element approaches, no alternative meshes are needed. The LDG discretization is also inherently local without the interelement continuity requirement, so it can easily handle complicated geometries, is well-suited for unstructured, non-conforming meshes, and can readily support *hp*-adaptation strategies [83]. However since the LDG method does not enforce interelement continuity, it requires more degrees of freedom to compute a solution than a conforming finite element method for equivalently discretized domains [97].

Time integration methods used with DG spatial discretization approaches for hyperbolic or near hyperbolic problems have been primarily forward Euler [64, 61] or TVD Runge-Kutta discretizations [85, 84, 86, 9, 150, 87, 88], with the exception of diagonally implicit Runge-Kutta methods [27]. Implicit time discretizations have been restricted to backward Euler [254]. To our knowledge, higher order MOL approaches for temporal integration have not otherwise been

investigated.

The LDG method has been applied to a wide range of problems of practical concern in porous media. These include pure diffusion problems [58, 78], convection-diffusion problems [87], and Stokes equation [26, 81]. Notwithstanding the good performance of the LDG method in these applications, open issues for certain classes of problems still remain. For example, the performance of the LDG method for nonlinear parabolic problems has not been fully investigated.

3.3 Approach

3.3.1 Overview

To meet the objectives of this work, we wish to advance and evaluate local discontinuous Galerkin approximations to RE that are also higher order in time using the method of lines (LDG-MOL). Both the LDG solution to RE and the general LDG-MOL approach for nonlinear systems of PDAE's are novel to the best of our knowledge. Because of the unique, and somewhat subtle, aspects of the formulation needed to produce a robust, efficient method, we present the approach used in detail, including the model formulations, spatial approximation, and temporal approximation.

3.3.2 Model formulations

Consider a general model of the form

$$\frac{\partial G}{\partial t} = \frac{\partial H}{\partial z} + f^s, \quad \text{in } \Omega \times [0, T] \quad (3.1)$$

where G and H are potentially nonlinear functions of the dependent variable ϕ , the spatial coordinate z , and time $t \in [0, T]$; f^s is a source; $\Omega \in [0, z_l] \subset \mathbb{R}^1$ is the spatial domain with boundary Γ ; and z_l is the length of the domain. While we restrict the systems of concern to \mathbb{R}^1 , straightforward extension to \mathbb{R}^2 or \mathbb{R}^3 is an advantage of the methods being considered [87].

Three specific forms of Eqn. (3.1) were used in this work. Two of these models were used to investigate convergence characteristics in detail for smooth, linear problems, and the third model is RE, which was the focus of this work. Model I is a transient diffusion equation, which we get by setting $G = \phi$, $H = D\partial\phi/\partial z$, and $f^s = 0$

$$\frac{\partial\phi}{\partial t} = D\frac{\partial^2\phi}{\partial z^2}, \quad \text{in } \Omega \times [0, T] \quad (3.2)$$

Equation (3.2) is used to describe saturated groundwater flow, species diffusion, and heat transport for a wide a variety of systems under certain assumptions, which can be described by continuum mechanics.

Model II is Poisson's equation, which we get from Eqn. (3.1) by setting $G = 0$, and $H = d\phi/dz$

$$0 = \frac{d^2\phi}{dz^2} + f^s, \quad \text{in } \Omega \quad (3.3)$$

This equation is used to describe a variety of steady-state problems in science and engineering, especially those originating from potential flow.

Model III is RE, which is a PDAE generalization of Eqn. (3.1) and which has widespread applicability even in one spatial dimension [126, 285]. Although other choices exist [281, 188, 59], we formulate a mass conservative form of RE [32, 191, 124] as

$$\frac{\partial(\varrho\theta)}{\partial t} + \frac{\partial(\varrho q)}{\partial z} = f^s, \quad \text{in } \Omega \times [0, T] \quad (3.4)$$

where ϱ is the density of water, θ is the volumetric water content in the porous medium, and q is the Darcy velocity of the water phase.

Darcy's law was used to relate q to the pressure head ψ

$$q = -K \left(\frac{\partial\psi}{\partial z} + \rho d \right) \quad (3.5)$$

where

$$\psi = \frac{p}{\varrho_0 g} \quad (3.6)$$

$$\varrho = \varrho_0 e^{\gamma(\psi - \psi_0)} \quad (3.7)$$

$$\rho = \frac{\varrho(\psi)}{\varrho_0} \quad (3.8)$$

$$K = k_r(\psi) K_s \quad (3.9)$$

$$K_s = \frac{\varrho_0 g k_s}{\mu} \quad (3.10)$$

ψ is the water pressure head, p is the water pressure, ψ_0 is a reference water pressure head, ϱ_0 is a reference density of water corresponding to ψ_0 , γ is a compressibility coefficient for water, g is the gravitational acceleration constant, $d \in [-1, 1]$ accounts for the orientation of gravity relative to the spatial coordinate z , K is the effective hydraulic conductivity, K_s is the saturated hydraulic conductivity, k_r is the relative permeability, k_s is the intrinsic permeability of the porous medium, and μ is the dynamic viscosity of water.

Closure of Equations (3.4) and (3.5) requires constitutive relations to express θ and k_r in terms of ψ . We chose the common van Genuchten [286] relation to express θ , or effective saturation S_e , as a function of ψ :

$$S_e = \frac{\theta - \theta_r}{\theta_s - \theta_r} = \begin{cases} (1 + |\alpha_v \psi|^{n_v})^{-m_v}, & \text{for } \psi < 0 \\ 1, & \text{for } \psi \geq 0 \end{cases} \quad (3.11)$$

where θ_r is the residual volumetric water content, θ_s is the saturated volumetric water content, α_v is a parameter related to the mean pore-size, n_v is a parameter related to the uniformity of the pore-size distribution, and $m_v = 1 - 1/n_v$.

The Mualem [226] relation was used to represent k_r in terms of S_e , and hence ψ via Eqn. (3.11), as

$$k_r(S_e) = \begin{cases} S_e^{1/2} \left\{ 1 - \left(1 - S_e^{1/m_v} \right)^{m_v} \right\}^2, & \text{for } \psi < 0 \\ 1, & \text{for } \psi \geq 0 \end{cases} \quad (3.12)$$

Combining Eqns (3.4) and (3.5), we write

$$\frac{\partial(\rho\theta)}{\partial t} = -\frac{\partial u}{\partial z} + f, \quad \text{in } \Omega, t \in [0, T] \quad (3.13)$$

$$u = -\rho K \left(\frac{\partial \psi}{\partial z} + \rho d \right) \quad (3.14)$$

where u is the mass flux, and $f = f^s/\varrho_0$.

The initial and boundary conditions for the RE model are

$$\begin{aligned} \psi &= \psi^0 && \text{in } \Omega, t = 0 \\ \psi &= \psi^b && \text{on } \Gamma_D, t \in [0, T] \\ u &= u^b && \text{on } \Gamma_N, t \in [0, T] \end{aligned}$$

where ψ^0 is the initial condition, $\Gamma = \Gamma_D \cup \Gamma_N$ with $\Gamma_D \cap \Gamma_N = \emptyset$, ψ^b is a Dirichlet boundary condition on the boundary Γ_D , and u^b is the mass flux specified on the Neumann boundary, Γ_N .

3.3.3 Spatial approximations

The LDG spatial approximations of focus in this work share some similarities with standard Bubnov-Galerkin methods but also some notable differences. The discontinuous nature of the methods leads to multiple values of the dependent variable at element boundaries or interfaces and allows for straightforward spatial adaption including the use of higher order elements and local resolution. The multi-valued nature of the interfaces leads to more unknowns than a standard Bubnov-Galerkin or low-order finite difference (FD) solution for an equivalent discretization, but an appropriate weak formulation ensures local conservation properties on the same mesh, which is a property lacking from standard conforming finite element methods.

While three models were used in this work, we only consider the detailed formulation of the RE model, since all models follow as subsets of Eqn. (3.1) and RE is the most complicated case considered. The detailed formulation of Models I and II are simple subsets of the approach taken to approximate RE.

For the spatial approximations, we detail the weak formulation, element interface conditions, nonlinear approximations, and integration methods used in turn in the sections that follow.

3.3.3.1 Weak formulation

We write Eqns (3.13) and (3.14) in an expanded form [10, 7]

$$\frac{\partial m}{\partial t} = -\frac{\partial u}{\partial z} + f, \quad \Omega \times [0, T] \quad (3.15)$$

$$m = \rho\theta \quad (3.16)$$

$$v = \frac{\partial \psi}{\partial z} + \rho d \quad (3.17)$$

$$u = -\rho K v \quad (3.18)$$

where v accounts for the driving force due to pressure gradients and gravitational forces.

We discretize Ω into n_e non-overlapping intervals $\Omega_j = [z_{j-1/2}, z_{j+1/2}]$, $j = 1, \dots, n_e$, with centers $z_j = (z_{j-1/2} + z_{j+1/2})/2$, and length $\Delta z_j = z_{j+1/2} - z_{j-1/2}$.

We construct a weak formulation using trial and test functions from the broken Sobolev space $H^1(\Omega_j)$ of the form

$$W(\Omega_j) = \{w \in L^2(\Omega) : w|_{\Omega_j} \in P^{k_j}(\Omega_j) \subset H^1(\Omega_j), \forall j\} \quad (3.19)$$

where $P^{k_j}(\Omega_j)$ is the set of polynomials of degree at most k_j on Ω_j . Note that the degree k_j may vary from element to element. We fix the degree $k_j = k$ for all quantities approximated, however this is not necessary [96, 97].

We use upper case letters M , Ψ , V , and U to denote trial solutions for m , ψ , v , and u . We choose our trial and test functions to be Legendre polynomials, which are denoted by N_j^l , where l is a function index and j is an element index.

We formulate a weak form of RE by multiplying Eqns (3.15)–(3.18) by test functions N_j^l and integrating Eqn. (3.15) and Eqn. (3.17) by parts over each

element to obtain

$$\int_{\Omega_j} N_j^l \frac{\partial M}{\partial t} dz = \int_{\Omega_j} \frac{\partial N_j^l}{\partial z} U dz - N_j^l U|_{j+1/2}^- + N_j^l U|_{j-1/2}^+ + \int_{\Omega_j} N_j^l f dz \quad (3.20)$$

$$\int_{\Omega_j} N_j^l M dz = \int_{\Omega_j} N_j^l \rho \theta dz \quad (3.21)$$

$$\int_{\Omega_j} N_j^l V dz = - \int_{\Omega_j} \left(\frac{\partial N_j^l}{\partial z} \Psi + N_j^l \rho d \right) dz + N_j^l \Psi|_{j+1/2}^- - N_j^l \Psi|_{j-1/2}^+ \quad (3.22)$$

$$\int_{\Omega_j} N_j^l U dz = - \int_{\Omega_j} N_j^l \rho KV dz \quad (3.23)$$

where the superscript + denotes a limit from the right side of the element boundary and a superscript - denotes a limit from the left side of the element boundary. This distinction is necessary because of the discontinuous nature of the LDG spatial discretization, which results in multiple values of the dependent variables at element boundaries.

The trial solutions over an element are of the form

$$\Psi = \sum_{l=0}^k N_j^l \Psi_j^l \quad (3.24)$$

$$M = \sum_{l=0}^k N_j^l M_j^l \quad (3.25)$$

$$V = \sum_{l=0}^k N_j^l V_j^l \quad (3.26)$$

$$U = \sum_{l=0}^k N_j^l U_j^l \quad (3.27)$$

where Ψ_j^l , M_j^l , V_j^l , and U_j^l are the solution variables sought.

3.3.3.2 Element interface conditions

To account for the fact that space W allows discontinuities across elements, the LDG approach requires special consideration of multiple-valued boundary conditions to ensure local conservation properties and to enforce boundary conditions appropriately. We term the treatment at these discontinuous boundaries

element interface conditions, while we note that these conditions have also been referred to as numerical fluxes in the hyperbolic conservation law literature [87]. Introducing singly defined values \hat{U} and $\hat{\Psi}$ at element boundaries allows Eqns (3.20)–(3.23) to be written as

$$\begin{aligned} \int_{\Omega_j} N_j^l \frac{\partial M}{\partial t} dz &= \int_{\Omega_j} \frac{\partial N_j^l}{\partial z} U dz - N_j^l|_{j+1/2}^- \hat{U}_{j+1/2} \\ &\quad + N_j^l|_{j-1/2}^+ \hat{U}_{j-1/2} + \int_{\Omega_j} N_j^l f dz \end{aligned} \quad (3.28)$$

$$\int_{\Omega_j} N_j^l M dz = \int_{\Omega_j} N_j^l \rho \theta dz \quad (3.29)$$

$$\begin{aligned} \int_{\Omega_j} N_j^l V dz &= - \int_{\Omega_j} \left(\frac{\partial N_j^l}{\partial z} \Psi + N_j^l \rho d \right) dz \\ &\quad + N_j^l|_{j+1/2}^- \hat{\Psi}_{j+1/2} - N_j^l|_{j-1/2}^+ \hat{\Psi}_{j-1/2} \end{aligned} \quad (3.30)$$

$$\int_{\Omega_j} N_j^l U dz = - \int_{\Omega_j} N_j^l \rho K V dz \quad (3.31)$$

The element interface conditions are of the general form

$$\hat{\Psi}_{j+1/2} = \langle \Psi \rangle_{j+1/2} + C_{12} [\Psi]_{j+1/2} \quad (3.32)$$

$$\hat{U}_{j+1/2} = \langle U \rangle_{j+1/2} + C_{11} [\Psi]_{j+1/2} - C_{12} [U]_{j+1/2} \quad (3.33)$$

where the interface operators are defined as

$$\langle \Psi \rangle_{j+1/2} = \frac{\Psi_{j+1/2}^+ + \Psi_{j+1/2}^-}{2} \quad (3.34)$$

$$[\Psi]_{j+1/2} = \Psi_{j+1/2}^- - \Psi_{j+1/2}^+ \quad (3.35)$$

$$\langle U \rangle_{j+1/2} = \frac{U_{j+1/2}^+ + U_{j+1/2}^-}{2} \quad (3.36)$$

$$[U]_{j+1/2} = U_{j+1/2}^- - U_{j+1/2}^+ \quad (3.37)$$

C_{11} in Eqn. (3.33) is a nonnegative penalty term that can be used to enhance stability, accuracy, and enforce Dirichlet boundary conditions [58]. The choice of C_{12} influences both the accuracy of the solution and compactness of the discrete approximation [78, 97].

For instance, choosing $C_{12} = 0$ leads to average fluxes at element interfaces

$$\hat{\Psi}_{j+1/2} = \frac{\Psi_{j+1/2}^+ + \Psi_{j+1/2}^-}{2} \quad (3.38)$$

$$\hat{U}_{j+1/2} = \frac{U_{j+1/2}^+ + U_{j+1/2}^-}{2} + C_{11}[\Psi]_{j+1/2} \quad (3.39)$$

while $C_{12} = -1/2$ gives

$$\hat{\Psi}_{j+1/2} = \Psi_{j+1/2}^+ \quad (3.40)$$

$$\hat{U}_{j+1/2} = U_{j+1/2}^- + C_{11}[\Psi]_{j+1/2} \quad (3.41)$$

On physical boundaries, we have

$$\hat{\Psi} = \psi^b, \quad \text{on } \Gamma_D \quad (3.42)$$

$$\hat{\Psi} = \Psi, \quad \text{on } \Gamma_N \quad (3.43)$$

$$\hat{U} = U + C_{11}(\Psi - \psi^b), \quad \text{on } \Gamma_D, \quad (3.44)$$

$$\hat{U} = u^b, \quad \text{on } \Gamma_N \quad (3.45)$$

where U and Ψ are the values taken from the interior of the domain and evaluated at the boundary. From this formulation, it can be observed that C_{11} plays an important role in enforcing first-kind boundary conditions for Ψ .

3.3.3.3 Nonlinear approximations

Both K and ρ are nonlinear functions of ψ and are components of u , which must be evaluated on element boundaries where the approximation Ψ is multiple valued. The highly nonlinear nature of RE can lead to sharp spatial gradients in θ , hence S_e and K , in some cases. If the sharp gradients are adequately resolved in space, approximating these nonlinearities is a straightforward matter. However, this so-called adequate spatial resolution may lead to prohibitively small element sizes and thus costly solves, which may not even be feasible for some multidimensional domains. These difficulties are not unique to LDG methods. Inadequate spatial resolution is known to produce approximate solutions for

which the rate of movement of a sharp front differs significantly from the solution to the real problem. In an effort to extend the spatial discretization needed to produce useful results, at least for application purposes, a variety of schemes can be used to estimate K [222, 301, 131]. We detail four approximations that we investigated to deal with this expected resolution problem.

Taking the arithmetic mean values of the conductivities at the element interfaces (KAI) is a straightforward approach, which can be written as

$$K_{j+1/2} = \frac{(K_{j+1/2}^+ + K_{j+1/2}^-)}{2} \quad (3.46)$$

We also consider a spatial integration approach (KINT), which integrates K over two adjacent elements. The integration was carried out on each of the two neighboring elements using Simpson's rule, which is of the form

$$K_{j+1/2} = \frac{\int_{z_{j-1/2}}^{z_{j+1/2}} K dz + \int_{z_{j+1/2}}^{z_{j+3/2}} K dz}{\Delta z_j + \Delta z_{j+1}} \quad (3.47)$$

Another common approach is to upwind the conductivity using the upstream value chosen from either the conductivity values at the element interfaces (KUI)

$$K_{j+1/2} = \begin{cases} K_{j+1/2}^-, & \text{if } \hat{U}_{j+1/2} \geq 0 \\ K_{j+1/2}^+, & \text{if } \hat{U}_{j+1/2} < 0 \end{cases} \quad (3.48)$$

or the upstream value based on element means obtained from Simpson integration (KUINT)

$$K_{j+1/2} = \begin{cases} \frac{1}{\Delta z_j} \int_{z_{j-1/2}}^{z_{j+1/2}} K dz, & \text{if } \hat{U}_{j+1/2} \geq 0 \\ \frac{1}{\Delta z_{j+1}} \int_{z_{j+1/2}}^{z_{j+3/2}} K dz, & \text{if } \hat{U}_{j+1/2} < 0 \end{cases} \quad (3.49)$$

Given values of K at element interfaces computed using one of the strategies summarized above, trapezoidal rule integration of the weak-form equation for U can be accomplished. However, higher order integration of this weak form equation requires approximations for K within an element. For such cases we evaluated two approaches for computing K at the element interior. One is a

linear approximation (LIN) based upon a Lagrange polynomial approximation, which is commonly used by standard finite element approaches [59, 244]

$$K_j(z) = \sum_{l=0}^1 L_j^l K_j^l \quad (3.50)$$

where $K_j^0 = K_{j-1/2}$, $K_j^1 = K_{j+1/2}$, and L_j^l is the l^{th} Lagrange polynomial on Ω_j . We also considered a more expensive, but potentially more accurate, direct (DIR) evaluation, $K_j(z) = K[\Psi(z)]$, where Ψ is approximated using the standard Legendre polynomial trial solution.

It is also necessary to evaluate the nonlinear terms ρ and θ , which also depend upon ψ . Because spatial gradients in ρ are generally small, this term is straightforward to resolve. We evaluated ρ on element boundaries as

$$\rho_{j+1/2} = \frac{\rho_{j+1/2}^+ + \rho_{j+1/2}^-}{2} \quad (3.51)$$

and when necessary on the interior of an element as $\rho_j(z) = \rho[\Psi(z)]$. Since only local evaluations of θ are needed, we used a direct approach $\theta_j(z) = \theta[\Psi(z)]$.

3.3.3.4 Integration methods

Solution of the LDG approximation to RE involves integration of Eqns (3.28)–(3.31). Computation of the integrals over an element can be accomplished by converting the trial solution to a natural spatial coordinate \tilde{z} , such that $\tilde{\Omega}_j \in [-1, 1]$. Transformed polynomial functions are of the general form

$$N_j^l(z) = \tilde{N}_j^l[F^{-1}(z)] \quad (3.52)$$

where the affine mapping F from $\tilde{\Omega}_j$ to Ω_j is described by

$$F(\tilde{z}) = \frac{\tilde{z}\Delta z_j}{2} + z_j \quad (3.53)$$

$$F^{-1}(z) = \frac{2(z - z_j)}{\Delta z_j} \quad (3.54)$$

The resulting transformed integrals can then be computed for each element using analytical or numerical means. The left-hand side of Eqns (3.28)–(3.31)

and the right-hand side of Eqn. (3.28) can be easily integrated analytically. For Models I and II and some approximations of RE, the remaining right hand side integrals can also be integrated analytically. For cases in which analytical integration was not convenient, we used Gauss-Lobatto quadrature up to 10 points. For Eqns (3.30) and (3.31) for RE, we computed the integrals on both sides of these equations using the same quadrature scheme. Two-point Gauss-Lobatto quadrature corresponds to the trapezoidal integration rule, which yields simple forms of the integrals involving only values at element boundaries, while higher point quadrature schemes may increase accuracy. These effects were investigated.

3.3.4 Temporal approximation

We used an adaptive step-size, variable order, fixed leading coefficient backward difference formula (FLC-BDF) method [51, 191] to meet the objectives of this work and to produce a robust and efficient simulator based upon the LDG spatial discretization method. The DAE integrator used estimates and controls local truncation error. It has been applied to solutions based upon various spatial approximations and shown to be advantageous compared to low-order or non-adaptive counterparts in other cases [191, 123, 124]. We detail this approach in the sections that follow.

3.3.4.1 Discrete form

The semi-discrete systems obtained from using LDG approximations for the spatial derivatives can be written abstractly as a set of DAE's

$$\{\mathbf{F}(t, \mathbf{y}, \mathbf{y}')\} = \{\mathbf{0}\} \quad (3.55)$$

where \mathbf{F} represents a set of equations that depend on time t , a set of dependent variables \mathbf{y} , and a set of first-order derivatives with respect to time of these dependent variables, \mathbf{y}' . At time level $n + 1$, an i^{th} order FLC-BDF converts

Eqn. (3.55) to the fully discrete system

$$\{\mathbf{R}(t^{n+1}, \mathbf{y}^{n+1}, \alpha^{n+1} \mathbf{y}^{n+1} + \boldsymbol{\beta}^{n+1})\} = \{\mathbf{0}\} \quad (3.56)$$

where α^{n+1} depends on i and the step-size, $\boldsymbol{\beta}^{n+1}$ is a function of the solution at the i previous time levels [124], and \mathbf{R} is referred to as the residual function. Following this notation, we can identify the solution variable \mathbf{y} for RE as $\mathbf{y} = \{\boldsymbol{\Psi} \mathbf{M}\}^T$ and rewrite Eqns (3.28)–(3.31) as

$$\{\mathbf{R}_{s,j}\} = [A_j]\{\alpha \mathbf{M}_j + \boldsymbol{\beta}_j\} - \{\mathbf{S}_j(\boldsymbol{\Psi})\} \quad (3.57)$$

$$\{\mathbf{R}_{M,j}\} = [A_j]\{\mathbf{M}_j\} - \{\tilde{\mathbf{M}}_j(\boldsymbol{\Psi})\} \quad (3.58)$$

where subscript j identifies quantities associated with the j^{th} element. Vector \mathbf{M}_j contains degrees of freedom $\{M_j^l | l = 0, \dots, k\}$ in the j^{th} element. Equation (3.57) corresponds to Eqn. (3.28), in which the flux variable U is approximated using Eqns (3.30) and (3.31), and Eqn. (3.58) corresponds to Eqn. (3.29). In Eqns (3.57) and (3.58), matrix A_j is diagonal with entries $\{\Delta z_j / (2l + 1) | l = 0, \dots, k\}$, $\mathbf{S}_j(\boldsymbol{\Psi})$ is the LDG spatial operator given by the right hand side of Eqn. (3.28), and $\tilde{\mathbf{M}}_j$ is the vector corresponding to the right hand side of Eqn. (3.29).

We combine the local residuals into a global expression and write

$$\{\mathbf{R}_s\} = [A]\{\alpha \mathbf{M} + \boldsymbol{\beta}\} - \{\mathbf{S}\} \quad (3.59)$$

$$\{\mathbf{R}_M\} = [A]\{\mathbf{M}\} - \{\tilde{\mathbf{M}}\} \quad (3.60)$$

While the resulting system currently has $2n_e(k + 1)$ equations, it can be reduced to a system of $n_e(k + 1)$ unknowns through a straightforward linearization process given below.

3.3.4.2 Algebraic solution

The discrete systems given by Eqn. (3.59) and Eqn. (3.60) were solved using Newton's method with a quadratic and cubic line search, formulated as

$$\{\mathbf{J}^{n+1, s_n}\} \{\Delta \mathbf{y}\} = -\{\mathbf{R}^{n+1, s_n}\} \quad (3.61)$$

where $\Delta \mathbf{y} = \mathbf{y}^{n+1, s_{n+1}} - \mathbf{y}^{n+1, s_n}$ and s_n is a nonlinear iteration index. The Jacobian matrix \mathbf{J} was formed by numerically differentiating Eqn. (3.56) with respect to \mathbf{y}

$$[\mathbf{J}^n] = \left[\frac{\partial \mathbf{R}^n}{\partial \mathbf{y}} \right] \quad (3.62)$$

The Newton iteration form for Eqns (3.60) and (3.59) is

$$\begin{bmatrix} \mathbf{A} & -\mathbf{D} \\ \alpha \mathbf{A} & -\mathbf{S}' \end{bmatrix} \begin{Bmatrix} \Delta \mathbf{M} \\ \Delta \Psi \end{Bmatrix} = \begin{Bmatrix} -\mathbf{R}_M \\ -\mathbf{R}_s \end{Bmatrix} \quad (3.63)$$

where $\mathbf{D} = \partial \tilde{\mathbf{M}} / \partial \Psi$, which is a block-diagonal matrix, and $\mathbf{S}' = \partial \mathbf{S} / \partial \Psi$. The Jacobian matrix shown in Eqn. (3.63) has a simple structure, namely, the blocks \mathbf{A} and $\alpha \mathbf{A}$ are diagonal, and $-\mathbf{D}$ is block diagonal. A simple manipulation of the system converts the Jacobian matrix into a block upper-triangular matrix

$$\begin{bmatrix} \mathbf{A} & -\mathbf{D} \\ 0 & -\mathbf{S}' + \alpha \mathbf{D} \end{bmatrix} \begin{Bmatrix} \Delta \mathbf{M} \\ \Delta \Psi \end{Bmatrix} = \begin{Bmatrix} -\mathbf{R}_M \\ \alpha \mathbf{R}_M - \mathbf{R}_s \end{Bmatrix} \quad (3.64)$$

We then solve the system

$$[-\mathbf{S}' + \alpha \mathbf{D}] \{\Delta \Psi\} = \{\alpha \mathbf{R}_M - \mathbf{R}_s\} \quad (3.65)$$

and update $\Delta \mathbf{M}$ with

$$\{\Delta \mathbf{M}\} = \{\mathbf{A}^{-1}\} (\{\mathbf{D}\} \{\Delta \Psi\} - \{\mathbf{R}_M\}) \quad (3.66)$$

To determine convergence of the nonlinear system, we use either the ℓ_2 norm of the relative residual or the weighted root mean square (WRMS) norm of the correction term

$$\|\Delta \mathbf{y}\|_{WRMS}^2 = \frac{1}{n_{eq}} \sum_j \left(\frac{\Delta y_j}{\epsilon_r y_j + \epsilon_a} \right) \quad (3.67)$$

where n_{eq} is the size of the nonlinear system, and ϵ_r and ϵ_a are the relative and absolute tolerance for the DAE integrator. The WRMS convergence test was used unless noted otherwise.

The linear systems resulting from Newton's method were relatively small and banded, so we used a banded lower-upper decomposition solver to solve the linear systems of equations resulting from the LDG-MOL approach.

3.4 Results

3.4.1 Overview

The purposes of the computations performed were to investigate the convergence rates and computational efficiency for LDG and LDG-MOL formulations for a range of models with a special focus on RE. As a number of investigations have indicated [222, 124, 31], there are several aspects of solution algorithms for RE that can affect these measures. Aspects investigated in this work include the following: spatial order, element interface conditions, nonlinear approximations, integration methods, and temporal integration order. We detail the problems and methods considered, efficiency measures, and computational results in the sections that follow.

3.4.2 Test problems

We investigated convergence rates and computational efficiency for LDG methods using Models I–III and set of five test problems. The purpose of considering Models I and II was to evaluate convergence rates independent of the difficult nonlinearities associated with Model III (RE). All models are subsets of a general formulation and Model I and II are special forms of the RE model, which physically correspond to transient and steady-state flow in a homogeneous, water-saturated porous medium, respectively. Given this correspondence, we detail all test problems using notation associated with the RE model, for which the methods used have been detailed.

Table 3.1 lists analytical solutions and simulation details for Problems I and II. Problem I is a smooth, linear, transient application of Model I, which is formally parabolic. Problem II is a smooth, linear, steady-state application described by Model II, which is formally elliptical. Dimensionless forms of these problems were solved using periodic boundary conditions as well as Dirichlet

Table 3.1: Summary of simulation conditions for Problems I and II

Functions	Problem I	Problem II
$\phi(x, t)$	$e^{-4\pi^2 t} \sin(2\pi x)$	$\sin(2\pi x)$
$\phi(x, 0)$	$\sin(2\pi x)$	$\sin(2\pi x)$
D	1.0	1.0
f	-	$4\pi^2 \sin(2\pi x)$
Ω	[0, 1.0]	[0, 1.0]
t	[0, 0.02]	-

boundary conditions. These problems were analyzed because they possess sufficient regularity to support a careful analysis of convergence characteristics of the methods.

Table 3.2 summarizes the simulation details for Problems III–V, which are applications of RE. Problem III is a standard test problem [250, 281, 191, 217] in which the auxiliary conditions lead to a moderately sharp infiltration front propagating through the domain without the development of saturated conditions. Problem IV models vertical infiltration with hydrostatic equilibrium as the initial condition, auxiliary conditions, and constitutive relation parameters that together result in an extremely steep infiltration front in both space and time [217]. Problem V involves the symmetric horizontal redistribution of a high saturation region introduced as an initial condition. Problems III and IV were used to evaluate computational efficiency and Problem V was used to evaluate symmetry properties of the various LDG-MOL methods investigated.

3.4.3 LDG schemes

We investigated many combinations of element interface conditions, nonlinearity approximations, trial solution polynomial orders, and integration methods. Table 3.3 summarizes a representative and illustrative set of these combinations

Table 3.2: Summary of simulation conditions for Problems III–V

Variable	Problem III	Problem IV	Problem V
θ_r (-)	1.020×10^{-1}	9.300×10^{-2}	9.300×10^{-2}
θ_s (-)	3.680×10^{-1}	3.010×10^{-1}	3.010×10^{-1}
α_v (m ⁻¹)	3.350×10^0	5.470×10^0	5.470×10^0
n_v	2.000×10^0	4.264×10^0	4.264×10^0
K_s (m/day)	7.970×10^0	5.040×10^0	5.040×10^0
ρ_0 (kg/m ³)	9.982×10^2	9.982×10^2	9.982×10^2
d (-)	1.0	1.0	0.0
γ (1/m)	4.797×10^{-6}	4.797×10^{-6}	4.797×10^{-6}
Ω (m)	[0, 0.3]	[0, 10]	[0, 10]
t (day)	[0, 0.25]	[0, 0.25]	[0, 3.0]
ψ_0 (m)	-10.0	-z	-10.0 for [0,4)∪(6,10] 0.1 for [4,6]
$\psi^b(0)$ (m)	-10.0	0.0	-10.0
$\psi^b(z_l)$ (m)	-0.75	0.1	-10.0

that will be discussed. These schemes are identified with labels of the form Aa - Fb , with $a = 0, 1, 2, 3$ distinguishing the Gauss-Lobatto quadrature points used for the integrals that appear in Eqns (3.28)–(3.31), and $b = 0, 1$ corresponding to the flux choices Ψ^+ , U^- and $(\Psi^- + \Psi^+)/2$, $(U^- + U^+)/2$, respectively.

A0-F0 and A0-F1 were used to evaluate the convergence rates of the LDG method for smooth problems. To minimize numerical integration error, high-order Gauss-Lobatto quadrature was used. A1, A2, and A3 were studied to evaluate a candidate set of LDG schemes suitable for solving RE. A1 used a trapezoidal quadrature rule for all the spatial integrals involved in the flux approximations. Although the trapezoidal integration is less accurate than a higher order integration, A1 together with one-sided numerical fluxes (A1-F0) bears the

Table 3.3: Spatial schemes

Label	Number of quadrature points	Interface conditions	Order, k
A0-F0	$Q_M: 10; Q_1: 10; Q_2: 10$	Ψ^+, U^-	0–3
A0-F1	$Q_M: 10; Q_1: 10; Q_2: 10$	$\frac{\Psi^- + \Psi^+}{2}, \frac{U^- + U^+}{2}$	0–3
A1-F0	$Q_M: 5; Q_1: 2; Q_2: 2$	Ψ^+, U^-	1
A2-F1	$Q_M: 5; Q_1: 3; Q_2: 2$	$\frac{\Psi^- + \Psi^+}{2}, \frac{U^- + U^+}{2}$	1
A3-F0	$Q_M: 5; Q_1: 3; Q_2: 3$	Ψ^+, U^-	1

most compact stencil, which can be advantageous in terms of computational effort. A2-F1 used Simpson’s rule for Eqn. (3.30), the trapezoidal rule for Eqn. (3.31), and average numerical fluxes. A3, used Simpson’s rule for both Eqns (3.30) and (3.31) and one-sided numerical fluxes. We restricted the spatial integration order to be no higher than third order (Simpson’s rule) and the LDG spatial order to be linear, since we found that increasing either the integration order or the approximation order did not lead to significant improvement of the accuracy. This should be expected as the solution for RE typically lacks sufficient smoothness needed for achieving global improvement by using uniformly higher order approximations.

In addition to the spatial schemes summarized above, we also evaluated the set of nonlinear approximations summarized in §3.3.3.3. The penalty term $C_{11} = 1$ was only applied when needed to enforce Dirichlet boundary conditions. As a further basis for comparison, we solved Problem III and IV using a cell-centered FD-MOL [217] approach based on arithmetic mean conductivity approximations. The temporal integration methods used in FD-MOL were identical to those used in the LDG-MOL method.

To evaluate the effect of higher order temporal integration on numerical efficiency, we compared efficiency of the LDG-MOL approach as a function of the maximum order of temporal integration allowed within the DAE integrator. The low-order time integration method was equivalent to a backward Euler adap-

tive (BEA) strategy, which has been examined for other spatial discretization approaches [191, 124]. We consider BEA to be superior to the fixed time-step method or heuristic adaption strategies that are routinely used to solve RE, because the step-size is automatically adjusted to meet the requested error tolerances without significant computational overhead [123].

3.4.4 Efficiency Measures

In order to evaluate the approaches considered in this work, we used a variety of methods to quantify the error in the numerical approximations and the computational effort required to compute these approximations. We considered three classes of error: spatial, temporal, and total spatial-temporal, and we considered two measures of computational effort.

To compute the error in a numerical solution, one needs a reference solution that is either analytical and exact in nature or a highly resolved numerical solution that has small error, and measures of the differences between the approximate and reference solutions. For Problems I and II, analytical solutions were used as the reference solutions. For Problems III and IV, dense grid solutions were computed using continuous cubic-spline approximations of cell-centered FDMOL solutions [217] computed using a uniform grid spacing consisting of 36,451 nodes and $\epsilon_a = \epsilon_r = 10^{-8}$. To evaluate temporal approximation error, the reference solution was computed using an identical spatial approximation to the case for which the comparison was desired, but highly resolved in time by selecting $\epsilon_a = \epsilon_r \leq 10^{-8}$. Problem V was only used to evaluate symmetrical properties of the solution and was not evaluated for computational efficiency.

The error between approximate numerical solutions and the reference solution was quantified in terms of differences in Ψ using discrete L_m ($m = 1, 2$) norms with high-order (ten-point) numerical quadrature

$$\varepsilon_{L_m} = \frac{(\sum_{j=1}^{n_e} \frac{\Delta z_j}{2} \sum_{q=1}^{10} |\Psi_{j,q}^n - \varphi_{j,q}^n|^m g_q)^{1/m}}{z_l} \quad (3.68)$$

where the superscript n denotes the time level, $\Psi_{j,q}^n$ is the approximate solution evaluated at quadrature integration points on element Ω_j , $\varphi_{j,q}^n$ is the reference solution at the corresponding points, and g_q is the corresponding Gauss-Lobatto quadrature weight. Ten-point quadrature was sufficiently accurate to ensure that the approximate error integrals were insensitive to this selection. To evaluate norms of temporal error alone, ε_{t,L_m} , Eqn. (3.68) was modified by substituting the consistent reference, time-resolved solution $\Phi_{j,q}^n$ in place of the fully resolved reference solution $\varphi_{j,q}^n$.

We also considered L_m error norms computed using midpoint quadrature, since this is commonly used for FD approximations

$$\varepsilon_{L_m}^c = \frac{(\sum_{j=1}^{n_e} \Delta z_j |\Psi_j^n - \varphi_j^n|^m)^{1/m}}{z_l} \quad (3.69)$$

where Ψ_j^n is the approximate solution at the element center at time level n , and φ_j^n is the corresponding reference solution.

We evaluated error in the L_2 norm for Problem I and II in order to compare our results with available theoretical and computational results [26, 87, 83, 88, 78]. While both L_1 and L_2 error measures have been used in the RE literature [261, 281, 222, 292, 217], L_1 errors were used to evaluate Problems III and IV. The relative performance of the methods under consideration was similar for both the L_1 and L_2 error norms.

We used two approaches to evaluate computational effort: the number of degrees of freedom (n_{dofs}) in the solution and the central processing unit (CPU) time. The former approach adjusts for the increased number of degrees of freedom required by LDG methods in comparison to traditional FD and conforming finite element methods. This approach was used to judge the convergence characteristics between methods on an even footing. We also evaluated efficiency using CPU time as a measure of work, which implicitly assumes a similar efficiency of implementation among the methods compared.

3.4.5 Computational results

3.4.5.1 Problems I and II

Problems I and II were examined to evaluate the spatial error as a function of the LDG scheme used. These problems possess the underlying smoothness needed to support a meaningful investigation. Because the focus of these simulations was on spatial error, all simulations for Problem I were performed using highly resolved time integration methods, which were achieved by setting $\epsilon_a = \epsilon_r = 10^{-12}$. Problem II is an elliptical problem, which did not require time integration.

Figure (3.1) illustrates the spatial error in Ψ and the convergence rates observed using LDG-MOL scheme A0-F0 with $C_{11} = 0$ and periodic boundary conditions. Similarly, Table 3.4 summarizes the convergence rates achieved for Problem I using several different schemes for both Ψ and U with Dirichlet boundary conditions. These convergence rates were consistent with the error analysis and numerical results given in the literature, in which the order of convergence for the LDG method varies with definitions of the numerical fluxes [83], element interface conditions, and use of the C_{11} penalty term [83, 88, 78]. For scheme A1-F0, A2-F1, and A3-F0, which use linear approximations, schemes based on average numerical fluxes had convergence rates of order 1 for both Ψ and U , while approximations with one-sided numerical fluxes resulted in convergence rates of 1.5 and 2 for Ψ and U , respectively.

The convergence rates obtained for Problem II matched those obtained for Problem I in general. This was expected, since temporal integration error was minimized in Problem 1. An exception to this general correspondence was cases where $C_{11} = 0$, which were not applicable since the LDG method for elliptic problems requires $C_{11} > 0$ [88, 56]. We further note that the linear system resulting from the LDG method is symmetric for linear problems like Problem I and II [14, 56].

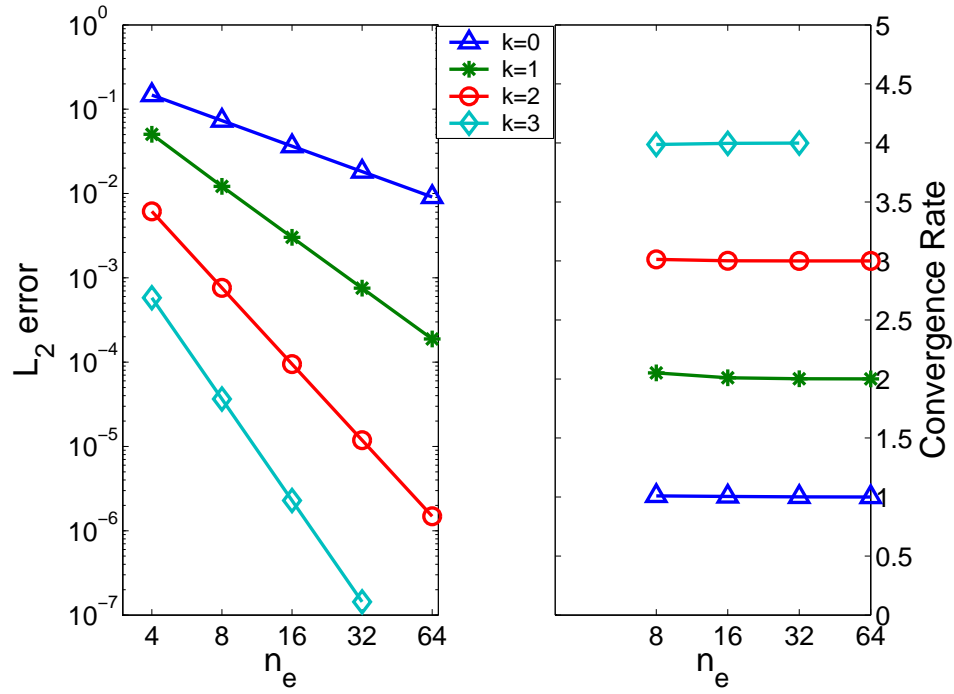


Figure 3.1: LDG convergence rates for scheme A0-F0 applied Problem I.

Table 3.4: Convergence rates for Problem I

Schemes	Convergence rate (for $\Psi; U$)
A0-F0 with $C_{11} = 0$	$k + 1; k + 1$ (even) $k + 1/2; k + 1$ (odd)
A0-F0 with $C_{11} = 1$	$k + 1; k + 1$
A0-F1 with $C_{11} = 0$	$k + 1; k + 1$ (even) $k; k$ (odd)
A0-F1 with $C_{11} = 1$	$k + 1; k + 1$ (even) $k + 1; k$ (odd)
A1-F0 with $C_{11} = 0$	1.5; 2 ($k=1$)
A2-F1 with $C_{11} = 0$	1; 1 ($k=1$)
A3-F0 with $C_{11} = 0$	1.5; 2 ($k=1$)

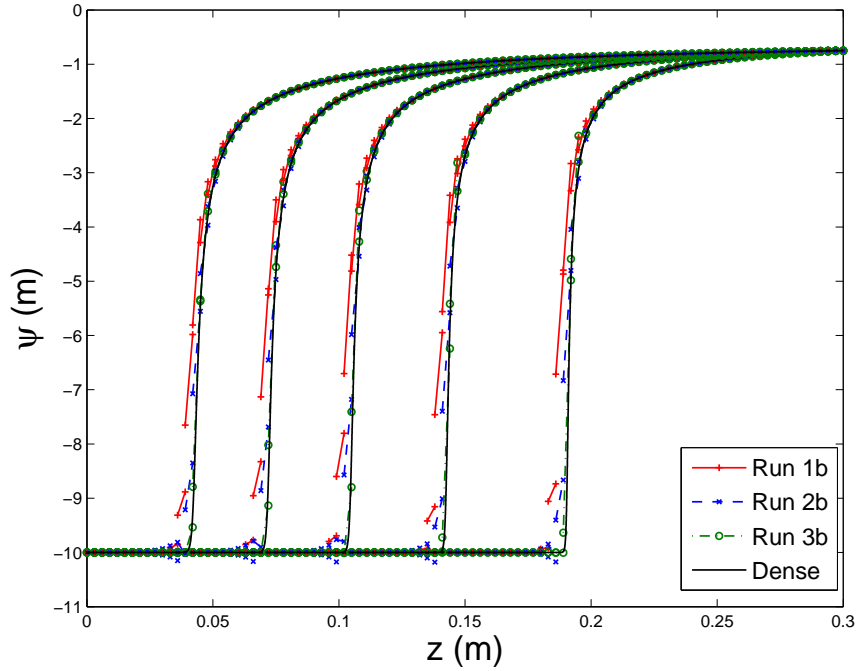


Figure 3.2: Pressure head profiles for Problem III for $t = 0.05, 0.10, 0.15, 0.20$ and 0.25 days.

3.4.5.2 Problem III

Table 3.5 summarizes the numerical experiments we performed to solve RE using the LDG schemes listed in Table 3.3 for Problem III. Runs 1–7 facilitated investigations of the spatial approximation schemes, while Runs 8c–29c allowed us to compare the high-order LDG-MOL approach to the BEA LDG-MOL approach.

Figure (3.2) shows results from Runs 1b–3b and illustrate significant variations of smoothness for this problem, which is typical for many problems modeled by RE. Figure (3.2) also shows that the LDG-MOL method was capable of resolving solutions for RE adequately using a relatively coarse discretization ($n_e=100$). Among the schemes we investigated, A1-F0 generated more diffusive solution than A2-F1, because of the uniform use of low-order trapezoidal rule integration. A2-F1, which used Simpson’s rule for integration in Eqn. (3.31), generated

Table 3.5: Summary of discrete approximation conditions for Problem III

Run [†]	Spatial scheme	Temporal method	n_e	$\epsilon_a = \epsilon_r$
1[a-d]	A1-F0, KINT	MOL	50, 100, 200, 400	10^{-6}
2[a-d]	A2-F1, KINT	MOL	50, 100, 200, 400	10^{-6}
3[a-d]	A3-F0, DIR-KAI	MOL	50, 100, 200, 400	10^{-6}
4b	A3-F0, LIN-KAI	MOL	100	10^{-6}
5b	A3-F0, DIR-KINT	MOL	100	10^{-6}
6b	A3-F0, DIR-KUI	MOL	100	10^{-6}
7b	A3-F0, DIR-KUINT	MOL	100	10^{-6}
[8-12]c	A2-F1, KINT	BEA	200	$10^{-2}, 10^{-3}, 10^{-4},$ $10^{-5}, 10^{-6}$
[13-18]c	A2-F1, KINT	MOL	200	$10^{-2}, 10^{-3}, 10^{-4}$ $10^{-5}, 10^{-6}, 10^{-10}$
[19-23]c	A3-F0, DIR-KAI	BEA	200	$10^{-2}, 10^{-3}, 10^{-4},$ $10^{-5}, 10^{-6}$
[24-29]c	A3-F0, DIR-KAI	MOL	200	$10^{-2}, 10^{-3}, 10^{-4}$ $10^{-5}, 10^{-6}, 10^{-10}$

[†] alphabetical qualifier corresponds to the spatial discretization given by n_e

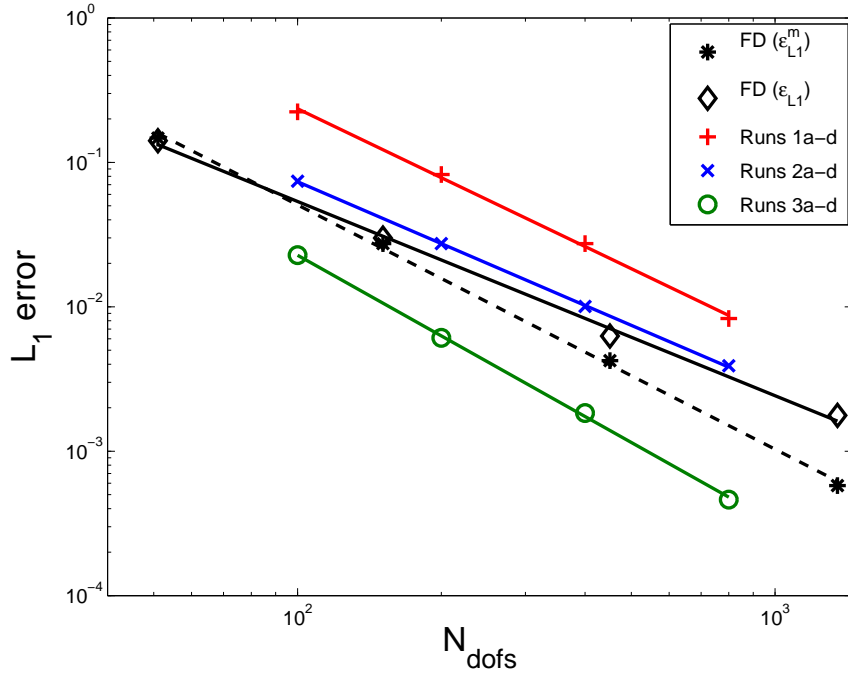


Figure 3.3: Comparison of the LDG and FD methods for Problem III.

solutions with sharper fronts, although some small undershoots appeared ahead of the infiltration front at this discretization level. These small undershoots were caused by the choice of average numerical fluxes and the relatively coarse spatial discretization. As we refined our spatial discretization level (e.g. $n_e = 800$), these undershoots vanished. Moreover, including a moderate penalty term $C_{11} = 0.1$ also suppressed these small oscillations at coarser grids (e.g. $n_e = 200$). A3-F0, which used the more accurate DIR conductivity approximation, generated the most accurate solutions.

The accuracy of these LDG schemes as a function of n_{dofs} is shown in Figure (3.3), along with a comparison to the FD method. While we quantify the accuracy mainly based on the same norm ϵ_{L_1} , we also show error norm $\epsilon_{L_1}^c$ for the FD solution since it is commonly used in the literature. The different LDG schemes generated comparable convergence rates, and increased accuracy was observed following the order: A1-F0, A2-F1, FD, and A3-F0.

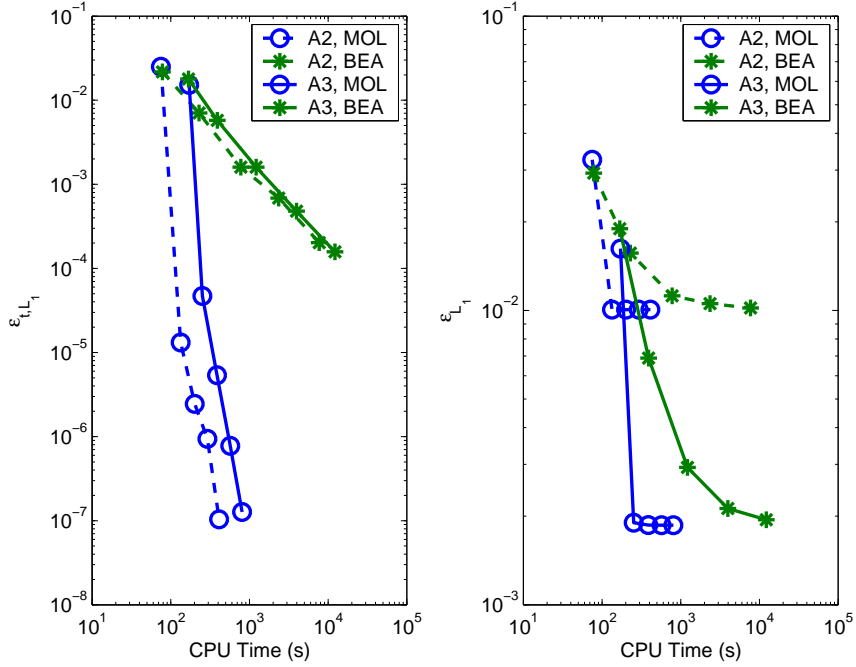


Figure 3.4: Computational efficiency for Problem III using the LDG method: (a) temporal error for Runs 8c–17c and 19c–28c, and (b) total error for Runs 8c–17c and 19c–28c.

We next investigated the performance of different approaches of evaluating K values. Since A3, unlike A1 or A2, included interior points in Eqn. (3.31), either the LIN or DIR approach was used to estimate K values that were not located on element interfaces. A comparison of results from Run 3b and 4b indicates that using the DIR approach reduced the L_1 error by nine times compared with estimating K using the LIN approach.

In order to compare different methods for evaluating interface conductivity values, we solved Problem III using algorithm A3-F0 with DIR for the same discretization ($n_e = 100$) with KAI, KINT, KUI, and KUINT. We found that among these interface conductivity evaluation methods, KUINT produced the most diffusive solutions and hence significantly larger errors; KAI was the most accurate; and KINT and KUI resulted in errors that were two times and three times larger than KAI, respectively.

Figure (3.4) shows the computational efficiency of the high-order LDG-MOL

approach compared to the corresponding BEA approach for results from Runs 8c–29c. The fifth-order LDG-MOL approach was significantly more efficient than the first-order LDG-MOL approach. For example, the CPU time required for scheme A3-F0 to reach $\varepsilon_{t,L1} = 10^{-3}$ was approximately an order of magnitude less for the high-order method compared to the low-order method. Figure (3.4) also shows that the low-order method can require orders of magnitude more CPU time compared to the high-order method to reach the point where the temporal error is insignificant compared to the spatial error; increased temporal accuracy beyond this point is wasteful for any method. Compared to A3-F0, A2-F1 produced higher spatial error, which means that temporal error was less significant for the overall solution and less accurate temporal accuracy was justified for this case.

3.4.5.3 Problem IV

Table 3.6 summarizes the numerical experiments we performed to solve RE using the LDG schemes listed in Table 3.3 for Problem IV. Runs 30–32 facilitated comparisons of different LDG schemes; Runs 32b–36b provided a basis for comparison of K estimation approaches; and Runs 37c–58c allowed us to evaluate temporal integration approaches.

Figure (3.5) compares solutions obtained using three different algorithms for Problem IV, corresponding to Runs 30b–32b, and Figure (3.6) shows the corresponding convergence rates for each of these schemes and the FD method. The infiltration fronts were steep for this problem with only two or three elements spanning the front, providing a rigorous test for any numerical method. The maximum errors produced at the front dominated the overall errors, and all three approaches were able to resolve the solution using a relatively coarse grid ($n_e = 100$). The low-order integration of algorithm A1-F0 produced a solution with flat segments. Algorithms A2-F1 and A3-F0 provided more accurate resolution of the steep front, and A3-F0, together with DIR-KAI K estimation, resulted in a solution that was significantly more accurate than an equivalent FD

Table 3.6: Summary of discrete approximation conditions for Problem IV

Run [†]	Spatial scheme	Temporal method	n_e	$\epsilon_a = \epsilon_r$
30[a-d]	A1-F0 KINT	MOL	50, 100, 200, 400	10^{-4}
31[a-d]	A2-F1 KINT	MOL	50, 100, 200, 400	10^{-4}
32[a-d]	A3-F0 DIR-KAI	MOL	50, 100, 200, 400	10^{-4}
33b	A3-F0, LIN-KAI	MOL	100	10^{-4}
34b	A3-F0, DIR-KINT	MOL	100	10^{-4}
35b	A3-F0, DIR-KUI	MOL	100	10^{-4}
36b	A3-F0, DIR-KUINT	MOL	100	10^{-4}
[37 ^a -41]c	A2-F1, KINT	BEA	200	$10^{-2}, 10^{-3}, 10^{-4},$ $10^{-5}, 10^{-6}$
[42 ^a -47]c	A2-F1, KINT	MOL	200	$10^{-2}, 10^{-3}, 10^{-4},$ $10^{-5}, 10^{-6}, 10^{-10}$
[48 ^a -52]c	A3-F0, DIR-KAI	BEA	200	$10^{-2}, 10^{-3}, 10^{-4},$ $10^{-5}, 10^{-6}$
[53 ^a -58]c	A3-F0, DIR-KAI	MOL	200	$10^{-2}, 10^{-3}, 10^{-4},$ $10^{-5}, 10^{-6}, 10^{-10}$

^a ℓ_2 relative residual convergence test

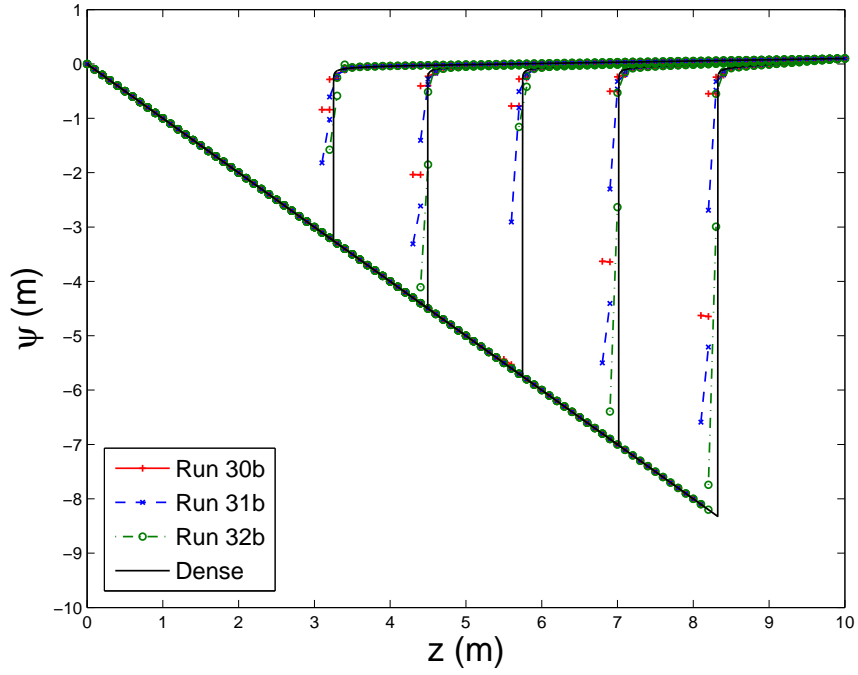


Figure 3.5: Pressure head profiles for Problem IV for $t= 0.05, 0.10, 0.15, 0.20,$ and 0.25 days.

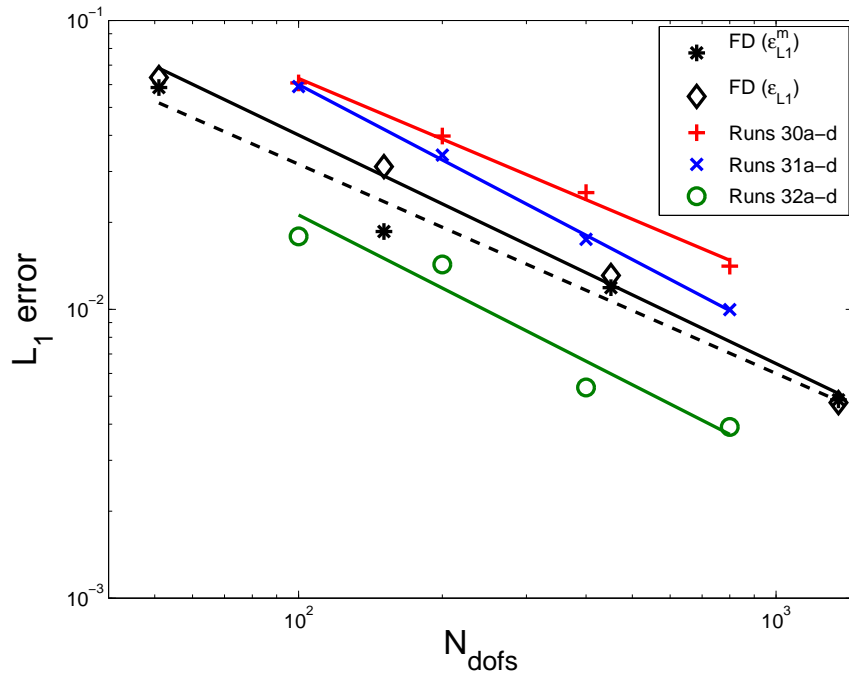


Figure 3.6: Comparison of the LDG method and FD method for Problem IV.

method.

We used A3-F0 with DIR to investigate different conductivity evaluation techniques in Runs 32b and 33b and found that the DIR-KAI approach had 20% less error than the LIN-KAI approach. This trend agreed with results found for Problem III, although a larger difference between the two approaches was observed for Problem III. Runs 32b and 34b–36b were used to investigate the effect of different interface conductivity evaluation methods. We found that KAI and KUI produced results with comparable accuracy; the L_1 error generated by KINT was 1.5 times larger than the error observed using KAI or KUI, while KUINT produced more diffusive results and larger error. This trend was also observed for Problem III. However, when these different interface conductivity evaluation methods were tested with A2-F1, we found that the KAI or KUI approach generated conductivities that were too small to mobilize the infiltration front adequately, while KINT was a universally robust—albeit sometimes less accurate—technique.

In order to analyze the mass-conservation properties of the LDG-MOL method, we modified this test problem with a Neumann boundary condition $u^b(z_l) = -5.0$ (m/day), a condition that allows us to simplify the mass balance calculations. We tested the mass balance errors using approximation conditions identical to Runs 30–32b. The global mass balance errors using A1-F0, A2-F1, and A3-F0 are all less than 3.0×10^{-8} , indicating excellent mass conservation of the LDG-MOL approach.

Figure (3.7) shows temporal error and total error at $t = 0.25$ days obtained from Runs 37c–58c. As with Problem III, the higher order temporal approach led to more rapid convergence rates and a more efficient method than the equivalent low-order LDG-MOL approach. For a temporal error tolerance $\epsilon_a = 10^{-2}$, the WRMS nonlinear solver convergence test performed poorly and was replaced by an ℓ_2 relative residual convergence test. As a result, the CPU time used by both DAE/MOL and BEA were greater for this value of ϵ_a than those observed when

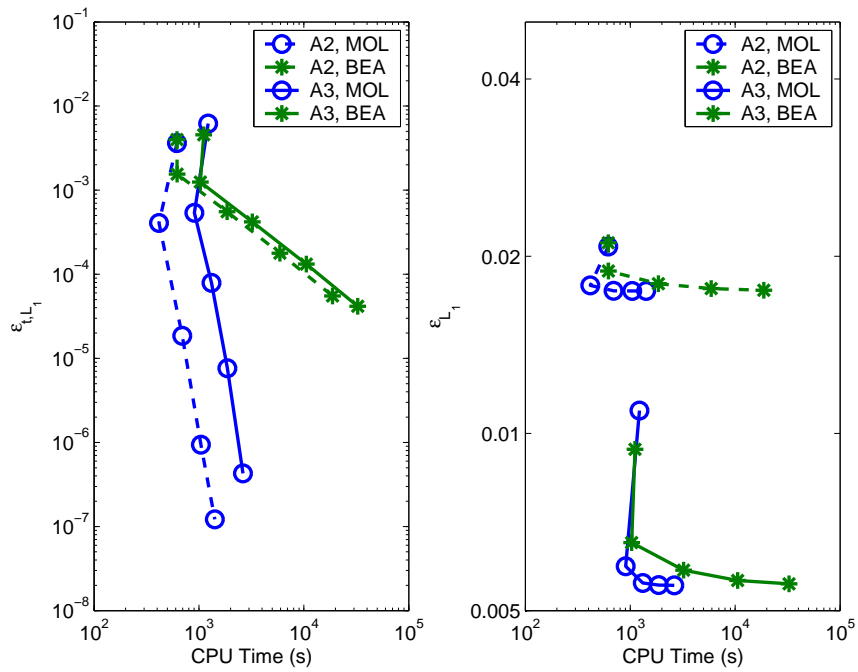


Figure 3.7: Computational efficiency for Problem IV using the LDG method: (a) temporal error for Runs 37c–46c and 48c–57c, and (b) total error for Runs 37c–46c and 48c–57c.

$$\epsilon_a = 10^{-3}.$$

When more accurate solutions were sought, we observed significantly more efficient solutions using high-order methods compared to first-order methods. As with Problem III, these differences became relatively less significant for those cases in which the spatial error was larger, such as was observed using algorithm A2-F1. Because of the steep fronts that characterized Problem IV, spatial error for this case was more significant than for Problem III, hence there were reduced benefits of high accuracy temporal integration for Problem IV compared to Problem III.

3.4.5.4 Problem V

Table 3.7 summarizes the numerical experiments we performed to solve RE for Problem V. This small set of simulations was performed to investigate the effect of the algorithm and the K estimation approach selected on the symmetry of the computed solution. The reference solution for this problem is symmetric, and it is desirable to have methods that preserve such features of a solution when they exist.

Table 3.7: Summary of discrete approximation conditions for Problem V

Run [†]	Method	n_e
59b	A1-F0 KINT	100
60b	A2-F1 KINT	100
61b	A3-F0 LIN-KINT	100
62e	A2-F1 KINT	2000
63b	A2-F1 KUINT	100
64b	A2-F1 KAI	100
65b	A2-F1 KUI	100

Figure (3.8) shows the LDG-MOL solution obtained from Runs 59b–61b, to-

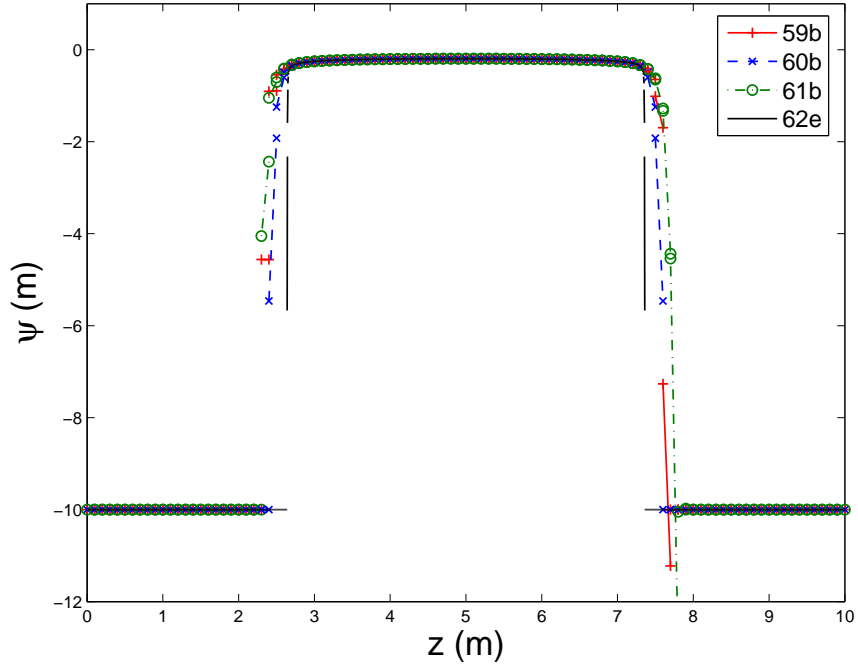


Figure 3.8: Comparison of LDG schemes for Problem V at $t= 3.0$ days.

gether with a reference solution obtained on a denser grid using A2-F1 (Run 62e). One-sided numerical fluxes in A1-F0 and A3-F0 resulted in asymmetric results. Moreover, at the coarsest discretization level ($n_e=100$), they produced overshoots on one side of the wetting front. Compared to full quadrature integration by A3, the trapezoidal rule used in A1 tended to decrease the magnitude of the oscillations. We also found that the magnitude of these oscillations decreased as we discretized our problem using finer grids. However, a large number of elements was needed for the oscillations to vanish due to the extreme sharpness of the solution. The scheme with averaged element interface conditions, A2-F1, was able to resolve this problem with symmetric and oscillation-free solutions at the coarse grid level shown in Figure (3.8).

In terms of the conductivity evaluation techniques, we found from Runs 60b and 63b–65b that KAI and KUI performed poorly for this problem when used together with A2-F1. This agreed with our results from Problem IV, where KINT was the most robust conductivity evaluation technique. We attribute this result

as well to the extremely sharp fronts that characterize this problem and thus the need for very fine spatial discretization to adequately resolve this feature. Averaging K over a larger region extends the range of spatial discretization for which reliable solutions can be obtained, thus enhancing robustness—even though such approaches are inherently less accurate in a fully resolved case.

3.5 Discussion

The above results show that variations of the LDG-MOL method were able to resolve a range of RE test problems efficiently and robustly. For the infiltration problems represented by Problems III and IV, we found that all three LDG schemes—A1-F0, A2-F1, and A3-F0—generally performed well. Among these schemes, A1-F0 used a less accurate integration method but bore the most compact stencil, which is appealing for computationally demanding simulations and multidimensional problems. A3-F0 was the most accurate scheme among the several schemes we tested. It allowed a more accurate conductivity representation and demonstrated the potential advantage of using a higher order spatial method over a standard FD method. On the other hand, the FD method produced oscillation-free solutions for every discretization level. The extremely sharp fronts associated with some of these test problems lack the smoothness needed to capitalize fully on uniformly high-order methods, hence the LDG-MOL approaches evaluated in this work showed only moderate improvements compared to FD methods for such cases.

One potential shortcoming of using the one-sided element interface conditions was that at coarse discretization levels, it relied upon the correct choice of the numerical fluxes to obtain good results for some problems. If numerical fluxes were chosen from the opposite direction (Ψ^- and U^+ in our case), undershoots appeared in some cases. While the magnitude of the oscillation eventually vanished with finer discretizations, the restriction of using highly refined grids is

not practical in many real applications. This drawback was illustrated in Problem V. At a coarse discretization level, A1-F0 and A3-F0 generated oscillations on one side of the wetting front. On the other hand, the scheme with average numerical fluxes resolved the solution without oscillations, which made it more robust than the other two algorithms. We also note that the trapezoidal rule for the flux equation used in A2 was necessary, since the combination of A3 and F1 introduced undershoots in some cases.

For the interface evaluation techniques we investigated in this work, we found that KAI, KUI, KINT, and KUINT performed well with Problem III, which was relatively smooth. However, KINT was superior when applied to problems with very sharp fronts.

Comparison between a high-order LDG-MOL approach and its first-order counterpart demonstrated the advantage of the high-order temporal discretization methods over low-order ones. The relative performance of the high-order LDG-MOL approach also depends on the target accuracy and the balance of spatial and temporal error for a particular problem. For problems that are sufficiently resolved in space, we found that the high-order integration method led to much more efficient solutions than a first-order approach. As the spatial accuracy decreased for less accurate schemes or for more difficult problems, the improvement in terms of total error provided by high-order methods in time decreased, reflecting the increased importance of spatial errors. Overall, the high-order LDG-MOL achieved the same level of error at no more, and usually significantly less, computational expense than its low-order counterpart.

Sharp spatial gradients are a common feature for unsaturated flow problems described using RE. As a result, uniformly high-order approximations or uniformly spaced grids can be wasteful in term of computational work. It has been shown that adaptive finite element methods, which increase the order of approximations where a solution is smooth and refine the mesh size where the solution is not smooth, are more advantageous than non-adaptive approaches in many cases

[171]. On the other hand, LDG approximations are essentially local without continuity restrictions across element boundaries, which makes them well-suited for adaptive strategies. Such topics are deserving of further study.

3.6 Conclusion

In this work, we solved a one-dimensional RE problem using the LDG method combined with a high-order temporal integration method that adapted both step-size and approximation order based upon a formal error estimate. Based upon this work, we draw the following conclusions:

- LDG-MOL methods can provide robust and efficient solutions to RE, even for especially difficult problems. MOL was used as a way to introduce a sophisticated temporal approximation for RE, which is capable of efficiently controlling the temporal error to an insignificant level compared to the spatial error.
- The choice of element interface conditions, numerical quadrature methods, and conductivity evaluation methods had a significant impact on the performance of the LDG solutions to RE. The scheme with higher order quadrature and one-sided numerical fluxes (A3-F0) produced the most accurate solution in some cases, but the scheme with trapezoidal integration for the flux equation and average numerical fluxes (A2-F1) was more robust.
- The tradeoffs between robustness and accuracy are a result of extremely sharp fronts that can develop for certain applications of RE. This feature also affects the relative magnitude of advantages of high-order temporal integration compared to traditional low-order approaches. Therefore, we expect that an hp implementation of the LDG method combined with an MOL approach will deliver improved performance for RE.

Chapter 4

Adaptive Local Discontinuous Galerkin Approximations to Richards' Equation

4.1 Introduction

Groundwater flow in variably saturated porous media is modeled by nonlinear conservation laws, and their accurate and efficient solutions are of great importance. Solutions of the resulting partial differential equations (PDE's) often exhibit a range of localized structures, such as steep infiltration fronts, along with smooth transition regions. A good example is Richards' equation, which has been extensively used in modeling water-air systems in porous media, under the assumption that the air phase remains at constant pressure. RE is a highly nonlinear parabolic equation under unsaturated conditions, but degenerates to a PDE of elliptic type when the soil matrix is fully saturated and water is considered incompressible. As a result, its solution combines dynamically moving sharp fronts and smooth regions, which poses significant challenges to the robustness and efficiency of many numerical methods.

Because of the difficulty associated with obtaining accurate and efficient so-

lutions for RE, there have been ongoing efforts to improve temporal and spatial integration techniques [281, 222, 188, 191, 41, 120, 294, 123, 205], as well as nonlinear and linear solution methods [245, 202, 282, 124]. Among these areas, temporal discretization methods along with nonlinear and linear solver aspects of solving RE, have been considered well-established compared to spatial discretization. The implementation of variable order, adaptive time integration method using a method of lines (MOL) framework to approximate RE, which dynamically changes the time-step size and approximation order with formal error control, is considered a milestone.

Advancing spatial discretizations is a primary focus of current active research. A number of spatial discretization methods, including finite differences, mixed finite elements, and discontinuous Galerkin finite elements have been combined with the advanced time integration methods through the method of lines and have demonstrated advantages of adaptive high-order time integration as opposed to low-order counterparts. However, these spatial methods are largely dominated by non-adaptive, fixed-order approaches. Although a fine, non-adaptive discretization may provide accurate numerical solutions to certain RE problems, the high computational costs associated may be prohibitive for complex multidimensional and large-scale simulations. Because of the time-dependent local structure typical for RE, it is ideal that an ultimate numerical RE solver include adaption in discretization size and order with error control in both space and time. While there has been effort on constructing adaptive spatial discretization methods, joint use of variable discretization size and order in both spatial and temporal domain has received little attention.

Adaptive finite element methods, whereby the discretization size and/or approximation order changes dynamically during a simulation, offer greater flexibility and improved efficiency for approximating solutions with varying local structure. Three adaptive strategies frequently employed are mesh refinement (h -refinement), order variation (p -refinement), and combinations of h and p re-

finement (*hp*-refinement). On the other hand, the LDG method has received increasing attention in computational fluid dynamics because of a number of attractive features including mass conservativity, ease to extend to multiple spatial dimensions, and *hp* well-suitedness, which are common for DG methods. Since no interelement continuity is required, solutions can be defined on non-conforming meshes. In addition, polynomials of arbitrary order can be used for each element, making this method well-suited for *hp* refinement. While the *hp* LDG method seems attractive, the realization of an effective *hp* method for practical computations of RE is a non-trivial task. Compared to a uniform discretization approach, the additional burden includes developing error indicators/estimators to efficiently guide the adaption approach, constructing effective remeshing strategies with data structures capable of managing discretization changes, and projecting solutions from one mesh to another efficiently while maintaining mass conservation.

Here, we extend our previous work on LDG-MOL for RE and present two adaptive LDG-MOL methods to approximate RE. Our objectives are (1) to formulate adaptive LDG-MOL methods, which dynamically adapts the mesh as well as the time steps; (2) to address necessary algorithmic components in the adaptive methods; and (3) to evaluate the accuracy and efficiency of the approximate solutions for a range of test problems.

4.2 Background

4.2.1 Overview

There exist two types of conceptual paradigms for building spatially and temporally adaptive discretizations to solve a PDE system, an MOL approach and Rothe's approach. The MOL is a popular approach, which first discretizes a PDE spatially to formulate a system of semi-discrete ODE's or DAE's. Then,

one can bring the existing mature time integration technology to bear on the semi-discrete ODE/DAE systems [191, 217]. In contrast to the MOL approach, a time discretization approach can be first applied to the PDE system to generate a semi-discrete elliptic problem on which the elliptic solution technology can be applied [31, 278] (Rothe’s method). While coupled space-time discretizations exist [118, 117, 211], they tend to be more difficult to construct and are subject to strong stability requirements for the original and dual problems [117]. While we believe Rothe’s method and coupled space-time approaches have significant merits in advancing PDE solution techniques, we focus on the MOL approach and discuss the relevant background in the subsections that follow.

4.2.2 Temporal adaption

While there continues to be ongoing effort to improve temporal integration methods [174], it is a common belief that temporal integration methods are mature compared to spatial discretization methods. The evidence partially lies in the popularity of robust, efficient, and well-established packages that use variable order, variable step size with formal error control [51, 210, 287, 281, 191, 124, 217, 205]. The mature temporal integration approach is commonly used within the MOL framework, which formally decouples the temporal and spatial approximations such that the temporal integration can be handled by sophisticated algorithms and codes designed to solve systems of ordinary differential algebraic equations. For a more detailed description of this method and review of the method within the MOL context, see [51, 190, 217].

4.2.3 Spatial adaption

A number of water flow and solute transport problems in subsurface systems exhibit localized features, such as penetration of sharp wetting fronts during infiltration and sharp concentration fronts during convection-dominant solute

transport. These localized features impose local spatial resolution requirements that typically change with time and space. While a fixed fine mesh may provide acceptable numerical solutions for such problems, high computational cost may be prohibitive for large-scale multidimensional simulations with realistic auxiliary conditions.

Dynamic mesh adaption provides a powerful means for reducing computational time and memory consumption when solving evolutionary partial differential equations. The approach is especially useful when the solution exhibits localized behavior as in the case of a moving front where the change in solution occurs over a small fraction of the domain. The generation of the adaptive mesh is often guided by an error measure which quantifies the local spatial truncation error, which, together with a mesh adaption strategy, forms a feed-back process leading to economical discretizations for solution approximation. While a dynamically adaptive mesh offers appealing advantages over a pregenerated, fixed mesh, difficulties caused by computational overhead, added storage, and additional error due to mesh manipulation arise in designing dynamic mesh adaptation.

Many types of spatial adaptive approaches exist: (1) h methods, which refine the mesh by subdividing it into finer ones while maintaining the fixed-order approximations [108, 246, 217]; (2) p methods, which change the order of the approximation over elements while maintaining the same mesh pattern [280, 8, 53]; (3) r methods, which relocate a fixed number of grid points over the domain to minimize the error measure [55]; and (4) m methods, which switch spatial approximation methods in different regions to achieve improved performance [99, 97]. Combinations of these methods are also common, such as rh methods [199, 234], mh methods [97, 48], and hp methods [105, 231, 247, 23, 166]. hp methods have received particular attention over the last two decades.

A successful numerical model with mesh adaption contains three major components: (1) a solver to approximate the continuous spatial and temporal operator using discrete algebraic equations; (2) a method for identifying solution

errors or other measures for resolution; and (3) a strategy to dynamically alter the mesh to control/minimize the truncation error. The following subsections provide brief discussions on methodologies relevant to our work from these three aspects.

4.2.3.1 LDG-MOL solver

Discontinuous Galerkin (DG) finite element methods have made their way into the main stream of computational fluid dynamics with a wide variety of applications [88, 7, 26, 29, 75, 79, 172, 207, 297]. As one of the most popular methods in the DG method family, the LDG method has received considerable attention including consistency and stability analysis [87, 14] and application to a wide range of physical problems including compressible and incompressible flow [26, 82, 205], and contaminant transport in porous media [7, 98, 75, 76]. The LDG method originated from a mixed setting as a mixed finite element method and has several attractive properties including local mass conservation, flux continuity, and the ability to handle complex geometries and unstructured, non-conforming meshes. In particular, the discontinuous nature of DG methods enables the LDG method as well as other DG methods to readily accommodate adaption with both h and p type. Vigorous efforts have been ongoing on to develop hp adaptive DG/LDG methods for a number of applications [47, 45, 267]. However, a particular shortcoming of the LDG method as well as other DG methods is that they require more degrees of freedom when computing a solution compared to a continuous Galerkin (CG) finite element method with an equivalent order of approximation. In response to this shortcoming, m methods that couple DG and CG methods have been suggested [99, 97, 100].

The temporal approximations that have been combined with DG spatial discretizations have typically been forward Euler [61], total variation diminishing Runge-Kutta discretization up to the third order [85, 84, 86, 7, 204], backward Euler [254], and diagonally implicit Runge-Kutta discretizations [27]. Recently,

the LDG method has been successfully combined with a fully adaptive FLC-BDF time integrator using MOL [205] to solve RE.

There has been considerable work advancing the h or hp adaptive methods within a DG framework to approximate PDE's of hyperbolic type [167, 170, 169, 227], elliptic type [291, 80, 272], and parabolic type [168]. However, the performance of adaptive DG methods for certain classes of problems, such as nonlinear parabolic problems like RE, has not been fully investigated. While formally a parabolic PDE model, RE can yield solutions with sharp fronts in space and time under certain auxiliary conditions. Based on the characteristic of RE and the good performance of spatially non-adaptive LDG-MOL methods for RE, it is expected that the LDG-MOL solver together with an effective adaptive technique will achieve improved performance for RE.

4.2.3.2 Error indicator/estimator

Insufficient spatial resolution is commonly recognized by error quantification methods of *a posteriori* type. Depending on the characteristics of the problems and available numerical techniques, these error quantification methods can be heuristic error indicators or formal error estimators [179, 217]. *A posteriori* error estimators can be derived by direct calculations using the finite element solution and some data such as source terms, and boundary conditions [57]. This type of error estimator for LDG methods has been developed for linear and nonlinear elliptic problems [57, 54]. On the other hand, an implicit *a posteriori* error estimator requires solution of a local boundary value problem approximating the residual equation. Such *a posteriori* estimators are more computationally demanding and only exist for limited range of problems [153] in a DG context. In other cases, heuristic and inexpensive error indicators are often constructed, usually using the first and second derivatives of domain variables [5, 212]. One popular method used to construct an error indicator in the engineering community is to postprocess the approximated solution to obtain more accurate

representations of the spatial gradient in terms of the solution variable and take the difference of the postprocessed gradient and the gradient directly calculated based on the solution. This method, commonly referred to as “gradient recovery method”, can perform remarkably well for a wide range of applications [5]. Examples of such indicators can be found in Babuska and Rheinboldt [22], Kelly [192], Zienkiewicz and Zhu [306]. Because most of the *a posteriori* error estimators are restricted to model problems [212] error indicators have been exclusively used in the RE literature, leading to meshes capable of capturing the evolution of the variably saturated flow [74, 31, 217].

As solutions to RE involve sharp features evolving in both the spatial and temporal domain, it is desirable that error indicators/estimators are able to account for the space-time behavior, as realized by a number of studies [31, 217]. The coupling of spatial and temporal behavior of the error indicators/estimators occurs naturally in methods that couple space-time discretizations [117]. In other cases, such error indicators/estimators inevitably include heuristics [217].

4.2.3.3 Adaptive strategies

h adaptive methods, originally designed for elliptic problems, have been the most straightforward and widely used adaptive methods for solving problems in sciences and engineering. An h adaptive strategy involves processing the error information represented by error indicators/estimators to determine the refinement/coarsening level on which a new mesh can be constructed. h remeshing strategies are often oriented towards achieving a prescribed level of accuracy using a minimal number of elements with minimal computational cost. For Rothe’s method, which discretizes the PDE of interest in time first to convert the PDE to an elliptic problem, the accuracy control naturally leads to iteratively adapting meshes and resolving until some prescribed error tolerance is met. However, for RE problems with sharp front evolution in both time and space, neglect of the solution evolution information in time may lead to inefficiencies [217]. For the

MOL method with advanced temporal integration techniques, small time steps needed to ensure the temporal accuracy often make spatial adaption at every time step unnecessary and inefficient. To improve efficiency, the spatial adaption can be performed at time steps much larger than the time steps used for integration [217]. In such cases, the accuracy control inevitably requires repeating temporal integration over large time steps used for spatial adaption. Therefore, care has to be taken in designing spatially adaptive strategies for RE to achieve improved efficiency.

Compared to pure h adaptive methods, hp adaptive methods require the choice of h or p type adaption for each element. Conceptually, it is more common to believe that h refinements near singularities or steep fronts is more appropriate. h refinement around the sharp regions succeeds due to a twofold effect. First, the measure of elements where the local regularity is limited by sharp features is reduced. Second, the measure of the elements where the solution is smooth is increased, thereby rendering p refinement more effective, as the sharp features become more localized [6]. In practice, it is a popular approach for elliptic problems to choose the order by selecting between p refinement and competitive h refinement. However, this strategy becomes more expensive as the order of approximations increases [224] and possibly intractable for parabolic or hyperbolic problems requiring many degrees of freedom and frequent spatial adaption. For parabolic or hyperbolic PDE's, decisions regarding h or p adaption for an element often employs a regularity indicator to quantify whether the local solution on the element is sufficiently "smooth." While there are a variety of methods to approximate the solution regularity in the hp literature [170, 6, 104], most of them used *ad hoc* parameters based on the p convergence using different orders of local approximations. On the other hand, the discontinuous feature of an DG solution can be taken advantaged of and simple jump terms at the interelement boundaries used to guide adaptive procedures [107, 224]. Good performance on many applications notwithstanding [46, 30], hp methods have not been applied

to RE to the best of our knowledge.

Adaptive methods requires data structures to store the mesh and manipulate the mesh refinement and coarsening. The complexity of data structures for some adaptive methods can be substantial [229]. A classic data structure that has been widely used in adaptive finite element methods appeared in Demkowicz [104], which employed singly linked lists to keep track of nodes and elements and handle refinement/coarsening.

4.3 Approach

4.3.1 Overview

Our goal is to develop robust and efficient methods that have the flexibility of adapting in both spatial and temporal domains. To achieve this goal, we propose two spatially adaptive methods capable of accommodating both h and p type adaption, combined with variable order, variable step-size time integration for solving RE. By using an MOL approach, the spatial discretization and adaption are easily uncoupled from the adaptive global time integration. We use an LDG spatial approximation because: (1) a non-adaptive LDG approach for RE was shown to perform well [205]; and (2) it allows great flexibility for performing both h and p adaption. The spatial adaption approach relies upon an effective error indicator to identify elements where resolution is poor. Based on the error indicator, elements can be marked with refinement or coarsening flags as appropriate, based on which a new mesh is constructed. A full hp adaption strategy also requires a criterion on whether to apply h or p adaption. In principle, after a region with relatively large error is identified, h refinement is performed where the solution is non-smooth, while p refinement is performed where the solution is smooth.

In this section, we first provide a summary of aspects of the problem formula-

tion and the MOL-LDG approach, which are detailed in Li et al. [205]. We then present our adaptive h and hp adaptive solution algorithms and address aspects of our adaption approaches, including adaption procedures, various operators, and implementation details.

4.3.2 Model formulations

RE is derived based on conservation of mass, Darcy's law, and closure relations expressing the relation among capillary pressure, water saturation, and relative permeability (p - S - κ relations). We use a mass conservative form of RE [32, 191, 124] that is applicable for modern DAE time integration methods. We restrict the problem of concern to one dimension, although extensions of the method being considered to higher dimensions are straightforward. We consider

$$\frac{\partial(\rho\theta)}{\partial t} = -\frac{\partial u}{\partial z}, \quad \text{in } \Omega, t \in [0, T] \quad (4.1)$$

$$u = -\rho K \left(\frac{\partial \psi}{\partial z} + \rho d \right) \quad (4.2)$$

with

$$\psi = \frac{p}{\varrho_0 g} \quad (4.3)$$

$$\varrho = \varrho_0 e^{\gamma(\psi - \psi_0)} \quad (4.4)$$

$$\rho = \frac{\varrho(\psi)}{\varrho_0} \quad (4.5)$$

$$K = k_r(\psi) K_s \quad (4.6)$$

$$K_s = \frac{\varrho_0 g k_s}{\mu} \quad (4.7)$$

where ϱ is the density of water, θ is the volumetric water content in the porous medium, u is the mass flux, ψ is the water pressure head, p is the water pressure, ψ_0 is a reference water pressure head, ϱ_0 is a reference density of water corresponding to ψ_0 , γ is a compressibility coefficient for water, g is the gravitational acceleration constant, $d \in [-1, 1]$ accounts for the orientation of gravity relative to the spatial coordinate z , K is the effective hydraulic conductivity, K_s is the

saturated hydraulic conductivity, k_r is the relative permeability, k_s is the intrinsic permeability of the porous medium, and μ is the dynamic viscosity of water, $\Omega \in [0, z_l] \subset \mathbb{R}^1$ is the spatial domain with boundary Γ ; z_l is the length of the domain, and $t \in [0, T]$.

We chose the common van Genuchten [286] and Mualem [226] relations to express θ (or effective saturation S_e) and k_r , respectively, as a function of ψ :

$$S_e = \frac{\theta - \theta_r}{\theta_s - \theta_r} = \begin{cases} (1 + |\alpha_v \psi|^{n_v})^{-m_v}, & \text{for } \psi < 0 \\ 1, & \text{for } \psi \geq 0 \end{cases} \quad (4.8)$$

and

$$k_r(S_e) = \begin{cases} S_e^{1/2} \left\{ 1 - \left(1 - S_e^{1/m_v} \right)^{m_v} \right\}^2, & \text{for } \psi < 0 \\ 1, & \text{for } \psi \geq 0 \end{cases} \quad (4.9)$$

where θ_r is the residual volumetric water content, θ_s is the saturated volumetric water content, α_v is a parameter related to the mean pore-size, n_v is a parameter related to the uniformity of the pore-size distribution, and $m_v = 1 - 1/n_v$.

The initial and boundary conditions for the RE model are

$$\begin{aligned} \psi &= \psi^0 && \text{in } \Omega, t = 0 \\ \psi &= \psi^b && \text{on } \Gamma_D, t \in [0, T] \\ u &= u^b && \text{on } \Gamma_N, t \in [0, T] \end{aligned}$$

where ψ^0 is the initial condition, $\Gamma = \Gamma_D \cup \Gamma_N$ with $\Gamma_D \cap \Gamma_N = \emptyset$, ψ^b is a Dirichlet boundary condition on the boundary Γ_D , and u^b is the mass flux specified on the Neumann boundary, Γ_N .

4.3.3 LDG-MOL approximations

The core LDG-MOL solution approach involves approximating the continuous problem using a discrete LDG spatial approximation in space and a FLC-BDF temporal approximation. Robust and stable nonlinear and linear solvers can then be used to advance the solution in time. We provide a summary of the spatial discretization, temporal discretization, and solver aspects of our approach

relevant to this work in the subsections that follow. Detailed investigations on various aspects of this approach can be found in Li et al. [205].

4.3.3.1 LDG spatial discretization

We write Eqns (4.1) and (4.2) in an expanded form [10, 7]

$$\frac{\partial m}{\partial t} = -\frac{\partial u}{\partial z} + f, \quad \Omega \times [0, T] \quad (4.10)$$

$$m = \rho\theta \quad (4.11)$$

$$v = \frac{\partial \psi}{\partial z} + \rho d \quad (4.12)$$

$$u = -\rho K v \quad (4.13)$$

where v accounts for the driving force due to pressure gradients and gravitational forces.

We divide Ω into n_e non-overlapping elements $\Omega_j = [z_{j-1/2}, z_{j+1/2}]$, $j = 1, \dots, n_e$, with centers $z_j = (z_{j-1/2} + z_{j+1/2})/2$, and length $\Delta z_j = z_{j+1/2} - z_{j-1/2}$. A union of these elements

$$\mathcal{G} = \bigcup_{j=1}^{n_e} \Omega_j \quad (4.14)$$

is commonly referred to as a grid or mesh, based on which the spatial approximations are performed. The size and structure of the mesh controls the resolution of the numerical method. A spatially adaptive method is to construct effective meshes providing sufficient resolution to various features in the solution and consequently improve efficiency.

We construct a weak formulation on grid \mathcal{G} using trial and test functions from the broken Sobolev space of the form

$$W(\Omega_j) = \{w \in L^2(\Omega) : w|_{\Omega_j} \in P^{k_j}(\Omega_j) \subset H^1(\Omega_j), \forall j\} \quad (4.15)$$

where $P^{k_j}(\Omega_j)$ is the set of polynomials of degree at most k_j on Ω_j . Note that the degree k_j may vary from element to element, allowing great flexibility in performing p adaption.

We approximate the continuous function m, ψ, v , and u by discrete trial solutions M, Ψ, V , and U . We choose our trial and test functions to be Legendre polynomials, which are denoted by N_j^l , where l is a function index and j is an element index.

We formulate a weak form of RE by multiplying Eqns (4.10)–(4.13) by test functions N_j^l and integrating Eqn. (4.10) and Eqn. (4.12) by parts over each element to obtain

$$\begin{aligned} \int_{\Omega_j} N_j^l \frac{\partial M}{\partial t} dz &= \int_{\Omega_j} \frac{\partial N_j^l}{\partial z} U dz - N_j^l|_{j+1/2}^- \hat{U}_{j+1/2} \\ &\quad + N_j^l|_{j-1/2}^+ \hat{U}_{j-1/2} + \int_{\Omega_j} N_j^l f dz \end{aligned} \quad (4.16)$$

$$\int_{\Omega_j} N_j^l M dz = \int_{\Omega_j} N_j^l \rho \theta dz \quad (4.17)$$

$$\begin{aligned} \int_{\Omega_j} N_j^l V dz &= - \int_{\Omega_j} \left(\frac{\partial N_j^l}{\partial z} \Psi + N_j^l \rho d \right) dz \\ &\quad + N_j^l|_{j+1/2}^- \hat{\Psi}_{j+1/2} - N_j^l|_{j-1/2}^+ \hat{\Psi}_{j-1/2} \end{aligned} \quad (4.18)$$

$$\int_{\Omega_j} N_j^l U dz = - \int_{\Omega_j} N_j^l \rho K V dz \quad (4.19)$$

where the superscript $+$ and $-$ denote limit from the right and left side of the element boundary, respectively. \hat{U} and $\hat{\Psi}$ appearing in Eqns (4.16)–(4.19) are singly defined values at element boundaries, which can affect the stability and accuracy of the solution. We here choose one-sided values Ψ^+ and U^- for $\hat{\Psi}$ and \hat{U} , respectively, while other possible options have also been investigated [58, 78, 97, 205].

On physical boundaries, we have

$$\hat{\Psi} = \psi^b, \quad \text{on } \Gamma_D \quad (4.20)$$

$$\hat{\Psi} = \Psi, \quad \text{on } \Gamma_N \quad (4.21)$$

$$\hat{U} = U, \quad \text{on } \Gamma_D, \quad (4.22)$$

$$\hat{U} = u^b, \quad \text{on } \Gamma_N \quad (4.23)$$

where U and Ψ are the values taken from the interior of the domain and evaluated

at the boundary.

Due to the orthogonal nature of Legendre polynomials, the solution V can be readily resolved element by element in terms of Ψ by Eqn. (4.18). Furthermore, U can be expressed in terms of V on each element using Eqn. (4.19) and then eliminated from Eqn. (4.16). In addition, M in Eqn. (4.17) can be eliminated from the system after applying the time integration method [see 191, 124, 205]. As a result, we only need to solve a linear system for the variable Ψ at each time level.

There are three nonlinear functions in this RE formulation: two highly nonlinear functions K and θ , and a weakly nonlinear function ρ . As it has been pointed out [205], conductivity evaluation methods is a critical component of a robust algorithm. While many choices of evaluating conductivities at the element boundaries exist [222, 205], we here only consider the arithmetic mean values of the conductivities to evaluate K at the element interface.

When high-order integration is needed for Eqn. (4.19), K values in the element interior are required. We consider two methods to approximate the interior conductivity value: evaluating K using p - S - κ relations directly (DIR), and linearizing the K values at the element interfaces (LIN). It is also necessary to evaluate the nonlinear terms ρ and θ , which depend upon ψ as well. Because the spatial gradients in ρ are generally small and evaluations of θ are local, we evaluate ρ and θ using the functional dependence of these variables on Ψ directly.

The majority of the integrals in Eqns (4.16)–(4.19) can be computed analytically, while those containing general nonlinear p - S - κ relations are approximated numerically, using the Gauss-Lobatto quadrature. We denote the quadratures used in Eqn. (4.17) and Eqn. (4.19) by Q_M and Q_F , respectively.

4.3.3.2 Temporal discretization

We consider a variable order, fully adaptive time integration method for time discretization. This method has received increasing attention in recent years and

standard and mature packages are now available [210, 190]. This approach has shown to be more robust and efficient than standard, low-order heuristic time integration approaches in a number of studies [281, 191, 123, 124, 205].

We apply the FLC-BDF approach to approximate the temporal derivatives, which adapts in step size and order with a formal error control. A full description of this scheme is given in Brenan et al. [51], while detailed formulation together with LDG spatial discretizations can be found in Li et al. [205].

4.3.4 Adaptive solution approaches

The goals of a successful spatially adaptive approach are twofold: (1) the approach should lead to a discretization that corresponds to a solution with a specified accuracy; and (2) the adaption should be achieved with a minimum number of unknowns at minimal computational cost [232]. If the second criteria is satisfied, a mesh generated by the approach should be an “optimal” mesh. However, the highly nonlinear nature of RE, the lack of rigorous regularity and convergence results for most numerical methods being used, together with the limited computational resources to solve an optimization problem, largely defies the pursuit of a truly optimal mesh.

With these considerations in mind, we propose two adaptive LDG-MOL approaches to approximate RE. They both use a simple but effective error indicator, a remeshing strategy, and an LDG-MOL solution approach to solve RE. The first approach is a straightforward adaptive strategy for finite element methods based on estimation of errors for the already computed LDG approximations [104]. This approach uses a hierarchical mesh which is self-adaptive to arbitrary refinement level. The second approach is a novel and effective adaption approach proposed by Miller et al. [217], which adapts spatially based on a local error indicator reflecting the changes of the solution in both spatial and temporal domain. It involves meshes at two levels: a coarse level with uniform discretization on which a forward solve is applied to facilitate adaptive mesh generation, and a

finer level with variably spaced elements on which a sufficiently accurate solution is obtained. We refer to the first and second approach K-level and two-level spatial adaptive approaches, respectively. To facilitate the discussion on the two methods, we first introduce a general adaptive framework to incorporate both the K-level method and the two-level method.

A general adaptive approximation can be outlined using the following algorithm starting from an initial solution $\Psi^{n=0}$ and an initial mesh $\mathcal{G}^{n=0}$, where n denotes the time level and n_T denotes the time level corresponding to T .

Algorithm 1 General adaptive framework

Require: $\Psi^{n=0}$ to be adequately resolved in space on $\mathcal{G}^{n=0}$, and the operators

\mathcal{R} , \mathcal{P} , and \mathcal{S} to be robust and sufficiently accurate

- 1: **for** $n = 0$ to $n = n_T$ **do**
- 2: $\mathcal{G}^{n+1,0} \leftarrow \mathcal{R}[\Psi^n(\mathcal{G}^n)]$
- 3: $\Psi^n(\mathcal{G}^{n+1,0}) \leftarrow \mathcal{P}[\Psi^n(\mathcal{G}^n)]$
- 4: $\Psi^{n+1}(\mathcal{G}^{n+1}) \leftarrow \mathcal{S}[\Psi^n(\mathcal{G}^{n+1,0})]$
- 5: **end for**

Ensure: At each time level n , Ψ^n to be consistent and adequately resolved in space and time within the bounds provided by the spatial error indicator and temporal error criteria.

Three types of operators are used in Algorithm 1: \mathcal{R} , \mathcal{P} , and \mathcal{S} . \mathcal{R} represents a remeshing operator, which generates a new mesh based upon error indicators obtained from the solution Ψ^n ; \mathcal{P} is a projection operator, which introduces a procedure to transfer a solution from one mesh to another. \mathcal{S} represents the solution process involving the LDG-MOL method with FLC-BDF temporal integration approach outlined in 4.3.3.

Line 1 defines a procedure to advance the approximate solution in time such that the solution is obtained at a set of increasing macroscale time points t^n with time step $\Delta t^n = t^{n+1} - t^n$. These time points t^n are also the points when

spatial adaption is executed. Due to the nature of RE for many sharp front problems, large numbers of time steps varying over several orders of magnitude are required to obtain a solution efficiently. Therefore, it is not computationally practical to perform the spatial adaption strategy every time step. Instead we perform the adaption only at so-called macroscale time points, which can be uniform or non-uniform, depending on the characteristics of the solution and the user's requirement. Appropriately selected macroscale time steps are important to the performance of adaptive methods. In general, it is desirable that these macroscale time steps be chosen in an adaptive fashion so that large time-dependent characteristics of the solution are incorporated into the adaption approach.

Line 2 defines a remeshing procedure to generate a new mesh \mathcal{G} for the next time level $n + 1$ based on the solution at time level n . It implicitly assumes that spatial truncation error dominates the total error so that reducing the spatial truncation error by adaptively choosing the discretization size and order will significantly decrease the spatial error as well as the total error. \mathcal{R} operator defines the central algorithm of the remeshing procedure, which involves two critical components: error indicators/estimators and remeshing strategies. Adaptive algorithms are typically based on an *a posteriori* error indicator/estimator computed from the already computed solution Ψ^n . Based on effective error indicators, the remeshing strategy should lead to a discretization that attempts to reduce the dominant spatial error for solutions between t^n and t^{n+1} . For an *hp* finite element method, the remeshing strategy also involves a procedure to choose *h* or *p* type adaption. This is often done by incorporating a local regularity indicator and a criterion to determine whether *h* or *p* type adaption should be applied.

Line 3 represents a projection procedure, which projects the solution at t^n on mesh \mathcal{G}^n to a solution on mesh $\mathcal{G}^{n+1,0}$, which provides an initial condition for the solution approach from t^n to t^{n+1} . It is desirable for the operator \mathcal{P} to be inexpensive to compute and mass-conserving.

Line 4 represents a solution procedure to solve the problem on a new mesh \mathcal{G}^{n+1} , which includes the spatial discretization approach and temporal integration outlined in 4.3.3. The FLC-BDF temporal integration adaptively controls both the size of the time step and the order of the approximation to meet user-prescribed tolerance and achieve efficiency [51]. It is desirable that the spatial approximation is carried in a similar fashion such that a fully adaptive simulator with formal temporal and spatial error control can be established. Towards this direction, the solution procedure, allowing for refinement as well as coarsening, is carried out iteratively, attempting to meet certain accuracy criteria. When such iterations are needed, $\mathcal{G}^{n+1,0}$ obtained from Line 1 becomes an initial mesh, which is updated through each iteration until a prescribed error tolerance is met. However, because of the decoupling of our spatial and temporal approximations intrinsic for the MOL approach, we allow for a repeat of the macroscale temporal solution. This potentially leads to increased computational overhead and decreased efficiency [31].

While both the K-level and two-level approaches can be incorporated into the general framework presented above, they differ in definition of the operators involved in the framework. We therefore use subscripts K and T to identify the operators specific for K-level and two-level methods, respectively. In addition, subscripts h and hp are used to identify the operators associated with h and hp type adaption, respectively. In the sections that follow, we first present two adaptive approaches with pure h adaption, and then detail the extension of the two-level method to hp adaption.

4.3.5 K-level adaptive approach

4.3.5.1 $\mathcal{R}_{K,h}$ operator

The remeshing operator $\mathcal{R}_{K,h}$ for a general h adaptive method requires an error indicator ($\boldsymbol{\eta}$), and a remeshing strategy. A typical algorithm used in an

adaptive finite element method can be outlined as

Algorithm 2 $\mathcal{R}_{K,h}$ operator

Require: Solution Ψ^n to be sufficiently accurate, spatial error to be dominant, operator \mathcal{E} to be capable of capturing the characteristics of error distribution, and operator $\mathcal{M}_{K,h}$ to be effective.

- 1: $\boldsymbol{\eta}^n(\mathcal{G}^n) \leftarrow \mathcal{E}[\Psi^n(\mathcal{G}^n)]$
- 2: $\mathcal{G}^{n+1,0} \leftarrow \mathcal{M}_{K,h}[\mathcal{G}^n, \boldsymbol{\eta}^n(\mathcal{G}^n)]$

Ensure: Solution approach on $\mathcal{G}^{n+1,0}$ from t^n to t^{n+1} generates solutions with approximately minimized spatial truncation error within the discretization limitations specified.

This algorithm describes the approach to generate a new mesh $\mathcal{G}^{n+1,0}$ based on which the solution process to the next time step proceeds. Operator \mathcal{E} represents the heart of a spatially adaptive algorithm, which quantitatively measures the quality of an approximate solution to the true solution. This takes the form of an error indicator or estimator on the current mesh based on either heuristic estimation or more rigorous finite element analysis. We consider here a popular error estimator proposed by Kelly et al. [193] based on a gradient recovery concept [5], which takes the form

$$\eta_j = \left\{ \frac{z_j^2}{24} \left[\left\| \left(\frac{\partial \Psi}{\partial z} \right)_{j-1/2} \right\| + \left\| \left(\frac{\partial \Psi}{\partial z} \right)_{j+1/2} \right\| \right] \right\}^{0.5} \quad (4.24)$$

where a jump operator at the element interface is defined as

$$\left\| \left(\frac{\partial \Psi}{\partial z} \right)_{j+1/2} \right\| = \left(\frac{\partial \Psi}{\partial z} \right)_{j+1/2}^- - \left(\frac{\partial \Psi}{\partial z} \right)_{j+1/2}^+ \quad (4.25)$$

This indicator is often used in conjunction with standard conforming finite element methods, as it bears out practical experience that the accuracy of the finite element approximation is related to the discontinuity of the finite element approximation to the gradient on the interelement boundaries [5]. Moreover, it

is also inexpensive to compute, which makes it preferable to an implicit error estimation approach.

Operator $\mathcal{M}_{K,h}$ represents a remeshing operator, which generates h -type refinement or coarsening flags (l_j) for each element on \mathcal{G}^n , based on which the data structure is then modified and a new mesh $\mathcal{G}^{n+1,0}$ is constructed. The h remeshing rule is such that an element on \mathcal{G}^n either remains unchanged ($l_j = 0$), or is subdivided into 2^{l_j} ($l_j > 0$) elements, or is coarsened ($l_j = -1$). Similar to the remeshing strategy described in Remacle et al. [253], the algorithm to determine h adaption flags is given by

$$l_j = \begin{cases} -1, & \text{for } \eta_j < \frac{\eta_{max}}{\alpha^{h_c}} \\ 0, & \text{for } \frac{\eta_{max}}{\alpha^{h_r}} > \eta_j \geq \frac{\eta_{max}}{\alpha^{h_c}} \\ l_{max} - i, & \text{elsewhere} \end{cases} \quad (4.26)$$

In this algorithm, α is a parameter to scale the error indicators, which can be related to the scales of the error indicators or the asymptotic behavior of the numerical methods. We here set α to be 10 as in Remacle et al. [253]. l_{max} is the maximum refinement level prescribed by users; the refinement level for an element can be determined by finding i such that $\eta_{max}/\alpha^{i+1} \leq \eta_j < \eta_{max}/\alpha^i$; and h_r , and h_c , are both user-defined parameters to determine refining and coarsening thresholds, respectively. For instance, if $l_{max} = 3$, $h_c = 3$, and $h_r = 2$, all elements where $\eta_j < \eta_{max}/10^3$ are coarsened; all elements where $\eta_{max}/10^3 \leq \eta_j < \eta_{max}/10^2$ are untouched; all elements where $\eta_j \geq \eta_{max}/10$ are refined with $l_j = 3$; and all elements where $\eta_{max}/10^2 \leq \eta_j < \eta_{max}/10$ are refined with $l_j = 2$. After generating a new mesh, we further smooth the mesh by restricting the maximum ratio of sizes of two neighboring elements to be 2.

As we use the MOL to decouple the spatial and temporal approximation and thus the spatial and temporal adaption, we only perform spatial adaption after a completion of time integration at the macroscale time step. In order to sufficiently resolve the solutions in spatial and temporal space, the sharp features in

the solutions should be enclosed in the spatially refined regions during the complete macroscale time step, which often leads to relatively small macroscale time steps, frequent spatial adaption, and consequently decreased efficiency. In order to improve the efficiency of the adaptive approach, a mesh buffering method has proven to be an effective means of increasing the macroscale time step [67, 163]. We consider here a simple buffering method, which extends the refined region by a fixed width that is equal to the size of a coarsest element in the mesh hierarchy. The refinement level for the buffer region is set to be l_{max} . The buffering algorithm increases the macroscale time steps needed by increasing the number of elements for a given mesh. As a result, there is a trade-off between the width of the buffer region and macroscale time step size for optimal computational performance.

The K-level remeshing strategy described above is self-adaptive, and thus requires a rather flexible data structure that supports the recursive and arbitrary refinement and coarsening efficiently. We adopted a classic approach similar to [104], in which a singly linked list algorithm was implemented to manipulate the hierarchical structure of the mesh and support mesh refinement and coarsening.

4.3.5.2 \mathcal{P} operator

Operator \mathcal{P} defines an approach for solution communication between meshes. It is desirable for a reliable operator \mathcal{P} to introduce no oscillations while maintaining comparable accuracy and mass conservation. We consider a straightforward L_2 local projection approach to obtain $\Psi^n(\mathcal{G}^{n+1})$ using a five-point Gaussian quadrature and denote this method by \mathcal{P}_Ψ .

An alternative method, denoted by \mathcal{P}_M , is to locally project variable M from one mesh to another, and then solve a local nonlinear problem given by Eqn. (4.17) to obtain variable Ψ on the new mesh. While this method is more complicated to implement, it strictly conserves the local discrete mass represented by variable M .

4.3.5.3 \mathcal{S}_K operator

\mathcal{S}_K operator represents the solution approach to advance the solution at t^n to the next macroscale time level t^{n+1} . The macroscale time step Δt^n can be user prescribed or automatically adaptive to satisfy certain criterion. We here consider a simple heuristic adaptive approach as in Hundsdorfer and Verwer [176]. After an appropriate macroscale time step is selected, we iterate the solution process and remeshing procedure until an error measure is controlled within a prescribed error criterion. We provide the steps and algorithms involved in this operator below.

The first part of the operator \mathcal{S}_K involves a standard adaptive time stepping approach to determine a macroscale time step Δt^n such that the solution change between the two successive macroscale time levels are controlled within a prescribed tolerance τ_t . The macroscale time step Δt is selected using

$$\Delta t = r_s r_t \Delta t^n \quad (4.27)$$

with

$$r_t = \tau_t / D \quad (4.28)$$

where D is the discrete L_2 norm of the difference in pressure head at t^n and t^{n+1} , which is explicitly $\|\Psi^{n+1} - \Psi^n\|_{L_2}$, and r_s is a safety factor.

The current time step is accepted if $D \leq \tau_t$, and the next time step Δt^{n+1} is set to Δt . Otherwise, the current time step is rejected and then repeated with the new time step $\Delta t^n = \Delta t$. The solution approach from t^n to t^{n+1} is carried using the LDG spatial discretization and the FLC-BDF temporal integration approach outlined in 4.3.3, which can be represented by an \mathcal{I} operator, namely

$$\Psi^{n+1}(\mathcal{G}^{n+1}) \leftarrow \mathcal{I}[\Psi^n(\mathcal{G}^{n+1}), \Delta t^n] \quad (4.29)$$

Note that the integration steps used in operator \mathcal{I} are independent of our macroscale time steps, as the integration steps are of variable order and variable size in

order to meet user-specified relative and absolute error criteria for local truncation error, whereas the macroscale time steps only determine the time points when the spatial adaption is needed. The integration operator proceeds over the macroscale time step adjusting the microscale internal time step as needed until the solution reaches t^{n+1} .

Algorithm 3 \mathcal{S}_K operator (Part II)

```

1:  $\boldsymbol{\eta}^{n+1}(\mathcal{G}^{n+1,0}) \leftarrow \mathcal{E}[\Psi^{n+1}(\mathcal{G}^{n+1,0})]$ 
2: if  $\|\boldsymbol{\eta}^{n+1}\|_{L_1} > \tau_s$  then
3:    $m = 0$ 
4:   repeat
5:      $\mathcal{G}^{n+1,m+1} \leftarrow \mathcal{M}_{K,h}[\mathcal{G}^{n+1,m}, \boldsymbol{\eta}^n(\mathcal{G}^{n+1,m})]$ 
6:      $\Psi^n(\mathcal{G}^{n+1,m+1}) \leftarrow \Psi^n(\mathcal{G}^{n+1,m})$ 
7:      $\Psi^{n+1}(\mathcal{G}^{n+1,m+1}) \leftarrow \mathcal{I}[\Psi^n(\mathcal{G}^{n+1,m+1}), \Delta t^n]$ 
8:      $\boldsymbol{\eta}^{n+1}(\mathcal{G}^{n+1,m+1}) \leftarrow \mathcal{E}[\Psi^{n+1}(\mathcal{G}^{n+1,m+1})]$ 
9:      $m = m + 1$ 
10:  until  $\|\boldsymbol{\eta}^{n+1}\|_{L_1} \leq \tau_s$ 
11: end if

```

This part of the algorithm simply quantifies the magnitude that the solution travels from t^n to t^{n+1} using the changes between the solutions, and reduces the macroscale time step when the solution change is beyond the prescribed tolerance τ_t . Therefore, by choosing an appropriate τ_t , this algorithm ensures that spatial adaption is performed sufficiently often so that the solutions in $[t^n, t^{n+1}]$ are adequately resolved by the spatially adaptive mesh. It also introduces a simple mechanism to enlarge the macroscale time step when changes in the solution are relatively small compared to the prescribed tolerance. While this adaptive approach for choosing the macroscale time step is heuristic and straightforward, it allows flexibility of performing spatial adaption according to the dynamics of the problem. This serves as an advantage when time-dependent features of the

solution profile vary at different time scales.

The second part of the algorithm described in Algorithm 3 involves recomputing solutions on a modified grid iteratively until some measure of the error indicators satisfies a prescribed tolerance. Line 1 obtains error indicators for the solution Ψ^{n+1} . If the discrete L_1 measure of the error indicator is greater than a user-specified spatial error tolerance τ_s , Line 4-10 are executed to iteratively update the mesh, project the solution at t^n to the new mesh, and resolve until the tolerance τ_s is met. The success of this part of the algorithm has two requirements: (1) each iteration should effectively reduce the solution error such that the extra computational expense involved in the iterations can be justified; (2) the change of the error indicators should faithfully represent the change of the true solution error such that true error can be controlled. It is clear that a non-iterative algorithm is a special case incorporated in this algorithm, which can be achieved using a sufficiently high τ_s such that no iteration is needed.

4.3.6 Two-level adaptive approach

Another adaptive strategy we consider follows closely the adaptive approach proposed by Miller et al. [217], who explored an inexpensive coarse mesh solution at t^{n+1} to identify the region where the sharp fronts would propagate and then use the information to guide the adaptive process. Because this method can effectively capture the front movement in both spatial and temporal domain, it has shown significant advantages over a corresponding uniform spatial discretization. We present this two-level adaptive approach by detailing the algorithms for operators in the general framework in Algorithm 1.

4.3.6.1 $\mathcal{R}_{T,h}$ operator

This two-level adaptive strategy involves solution processes at meshes at two levels, a uniformly discretized coarse mesh, and a finer adaptive mesh. The coarse mesh \mathcal{G}^c is a uniform coarse mesh that remains unchanged during the simulation.

Algorithm 4 $\mathcal{R}_{T,h}$ operator

Require: solution Ψ^n is sufficiently accurate and spatial error is dominant

- 1: $\Psi_c^n(\mathcal{G}^c) \leftarrow \mathcal{P}[\Psi^n(\mathcal{G}^n)]$
- 2: $\Psi_c^{n+1}(\mathcal{G}^c) \leftarrow \mathcal{S}_c[\Psi_c^n(\mathcal{G}^c)]$
- 3: $\eta^n(\mathcal{G}^c) \leftarrow \mathcal{E}[\Psi_c^n(\mathcal{G}^c)]$
- 4: $\eta^{n+1}(\mathcal{G}^c) \leftarrow \mathcal{E}[\Psi_c^{n+1}(\mathcal{G}^c)]$
- 5: $\eta^{n,n+1}(\mathcal{G}^c) \leftarrow \mathcal{T}[\eta^n(\mathcal{G}^c), \eta^{n+1}(\mathcal{G}^c), \Psi_c^n(\mathcal{G}^c), \Psi_c^{n+1}(\mathcal{G}^c)]$
- 6: $\mathcal{G}^{n+1,0} \leftarrow \mathcal{M}_{T,h}[\mathcal{G}^c, \eta^{n,n+1}(\mathcal{G}^c)]$

Ensure: solution approach on $\mathcal{G}^{n+1,0}$ from t^n to t^{n+1} generates solutions with approximately minimized spatial truncation error within the discretization limitations specified

An appropriate choice of the coarse mesh should meet two criteria: (1) solutions obtained on the mesh faithfully represent the evolutions of the solution; and (2) the computational work involved in calculating the solution on the coarse mesh is insignificant compared to the computational work on the adaptive fine mesh. Obtaining a solution at t^{n+1} on \mathcal{G}^c provides information regarding the dynamics of the solution with time, which is valuable for generating an effective adaptive mesh.

Line 1 represents projection of the known discrete solutions on a fine mesh \mathcal{G}^n to a coarse mesh \mathcal{G}^c . The projected solution provides the initialization for advancing the solution on the coarse grid from t^n to t^{n+1} .

Line 2 represents integration from t^n to t^{n+1} on the coarse mesh. This step is to obtain an approximate solution on the coarse mesh that is used to guide the spatial mesh generation. Similar to operator \mathcal{S}_K , solution operator \mathcal{S}_c adopts the adaptive macroscale time stepping method to ensure sufficiently frequent spatial adaption to capture the dynamics of solution propagation over time. However, as the purpose of obtaining solutions on the coarse mesh is to guide mesh generation, no error control is needed in \mathcal{S}_c . While the time stepping algorithm involved in

\mathcal{S}_c is identical to \mathcal{S}_K , we note that since this operator only operates on a coarse mesh, repeatedly reducing the macroscale time step to meet τ_t may have small influence in terms of the overall efficiency of the two-level adaptive approach.

Line 3-4 represent the operations of obtaining error indicators at t^n and t^{n+1} using solution Ψ_c^n and Ψ_c^{n+1} , respectively. These indicators are used to guide the mesh generation.

Line 5 represents an operation, denoted by \mathcal{T} , to incorporate solutions and the error indicators at two time points t^n and t^{n+1} into a new error indicator which can be used to guide the remeshing procedure. We first normalize the spatial indicator at t^n and t^{n+1} to a dimensionless quantity $\bar{\eta}_j \in [0, 1]$

$$\bar{\eta}_j = \frac{\eta_j - \eta_{min}}{\eta_{max} - \eta_{min}} \quad (4.30)$$

where η_{max} and η_{min} are the maximum and minimal values of η_j for $j = 1, \dots, n_e$ at the time level considered. We then simply consider the normalized pressure difference in time as an indicator of the temporal change of the pressure profile, which is given by

$$\epsilon_j^t = \frac{\Delta\Psi_{t,j} - \Delta\Psi_{min}}{\Delta\Psi_{max} - \Delta\Psi_{min}} \quad (4.31)$$

where $\Delta\Psi_{t,j} = |\Psi_j^{n+1} - \Psi_j^n|$, $\Delta\Psi_{max}$ and $\Delta\Psi_{min}$ are the maximum and minimum values of $\Delta\Psi_{t,j}$ for $j = 1, \dots, n_e$, respectively. We then take

$$\eta_j^{n,n+1} = \max(\bar{\eta}_j^n, \bar{\eta}_j^{n+1}, \epsilon_j^t) \quad (4.32)$$

as our error indicator to guide the h refinement.

Line 6 involves an operator $\mathcal{R}_{T,h}$, which generates a new mesh based on the integrated error indicator $\boldsymbol{\eta}^{n,n+1}$. The criterion of determining the adaption level for each element is

$$l_j = \begin{cases} 0, & \text{for } \eta_j \leq \frac{\eta_{max}}{\alpha^{h_r}} \\ \max(l_{max} - i, l_{j\pm 1} - 1), & \text{elsewhere} \end{cases} \quad (4.33)$$

where i is obtained such that $\eta_{max}/\alpha^{i+1} \leq \eta_j < \eta_{max}/\alpha^i$. Compare to the K-level method, the remeshing operator $\mathcal{R}_{T,h}$ greatly simplifies the implementation.

As operator $\mathcal{M}_{T,h}$ only operates on the coarse mesh, no coarsening is required. As a result, no hierarchical data structure is needed to maintain the element generations, which simplifies the implementation complexities and significantly reduces memory use.

4.3.6.2 \mathcal{S}_T operator

\mathcal{S}_T is an operator to calculate solution Ψ^{n+1} on the adaptive fine mesh \mathcal{G}^{n+1} at macroscale time step t^{n+1} . Since the macroscale time step Δt^n is determined within operator $\mathcal{R}_{T,h}$, \mathcal{S}_T only involves the approach to integrate solution Ψ^n to Ψ^{n+1} using the LDG-MOL approach presented in 4.3.3, which is simply $\Psi^{n+1} \leftarrow \mathcal{I}[\Psi^n, \Delta t^n]$.

4.3.6.3 Two-level hp adaptive approach

Because the LDG method does not enforce continuity at the element interfaces, both h and p type refinement are strictly local to elements being adapted, offering great flexibility for performing hp adaption. While it is straightforward to extend the adaption strategies to hp for both K-level and two-level adaptive approaches, we only show an hp approach using the two-level adaptive approach based on forward coarse mesh solve. The extra components needed for an hp approach are included in the $\mathcal{R}_{T,hp}$ operator, which is given below.

Compared to Algorithm 4, extra components involved in the hp adaptive algorithm include: (1) estimating local regularity γ for a given solution, (2) coupling the regularity indicators on the coarse mesh \mathcal{G}^c at t^n and t^{n+1} to a single indicator to identify the smooth region common for solutions in $[t^n, t^{n+1}]$, and (3) making decisions on whether to apply h or p adaption for each element. As a result, three new operators are used in the hp adaption algorithm: \mathcal{J} , \mathcal{N} , and $\mathcal{M}_{T,hp}$. Operator \mathcal{J} defines an approach to estimate the local regularity of the solution, which is required for choosing h or p adaption for a given element. Operator \mathcal{N} is an operator to incorporate regularity indicators at two time points

Algorithm 5 $\mathcal{R}_{T,hp}$ operator

Require: Solution Ψ^n is sufficiently accurate and spatial error is dominant

- 1: $\Psi_c^n(\mathcal{G}^c) \leftarrow \mathcal{P}[\Psi^n(\mathcal{G}^n)]$
- 2: $\Psi_c^{n+1}(\mathcal{G}^c) \leftarrow \mathcal{S}[\Psi_c^n(\mathcal{G}^c)]$
- 3: $\eta^n(\mathcal{G}^c) \leftarrow \mathcal{E}[\Psi_c^n]$
- 4: $\gamma^n(\mathcal{G}^c) \leftarrow \mathcal{J}[\Psi_c^n]$
- 5: $\eta^{n+1}(\mathcal{G}^c) \leftarrow \mathcal{E}[\Psi_c^{n+1}]$
- 6: $\gamma^{n+1}(\mathcal{G}^c) \leftarrow \mathcal{J}[\Psi_c^{n+1}]$
- 7: $\eta^{n,n+1}(\mathcal{G}^c) \leftarrow \mathcal{T}[\eta^n, \eta^{n+1}, \Psi_c^n, \Psi_c^{n+1}]$
- 8: $\gamma^{n,n+1}(\mathcal{G}^c) \leftarrow \mathcal{N}[\gamma^n, \gamma^{n+1}]$
- 9: $\mathcal{G}^{n+1,0} \leftarrow \mathcal{M}_{T,hp}[\mathcal{G}^c, \eta^{n,n+1}, \gamma^{n,n+1}]$

Ensure: solution approach on $\mathcal{G}^{n+1,0}$ from t^n to t^{n+1} generates solutions with approximately minimized spatial truncation error within the discretization limitations specified

t^n and t^{n+1} into a new error indicator which can be used to guide the hp adaption procedure. Operator $\mathcal{M}_{T,hp}$ represents a remeshing operator, which generates a new mesh with both h and p refinement.

Line 4 and Line 6 represent the operation of obtaining regularity indicators at t^n and t^{n+1} , respectively. We consider the approach proposed in Dolejsi et al. [107], which employed jump terms at the interelement boundaries from the DG solution to guide the adaptive procedure. This procedure is based on the observation that the interelement jumps in the approximate solution are of order $O(1)$ around discontinuities, but $O[(\Delta z)^2]$ in the areas where the solution is regular, assuming Δz is the size of an element under uniform discretization. While the application of the jump terms as a regularity indicator deserves further theoretical justification, computational results in Dolejsi et al. [107] demonstrated that this indicator works effectively with DG methods. In addition, it is very inexpensive in practice. Therefore, the regularity indicator we use is based on a

similar idea, namely

$$\gamma_j = \left[\frac{\log(\bar{\Psi}_j)}{\log(\Delta z_j)} \right]^{-1} \quad (4.34)$$

where $\bar{\Psi}_j$ is the normalized average jump term for element j , given by

$$\bar{\Psi}_j = \frac{0.5 (|\llbracket \Psi_{j-1/2} \rrbracket| + |\llbracket \Psi_{j+1/2} \rrbracket|)}{\Psi_{max}} \quad (4.35)$$

Ψ_{max} takes the maximum of the absolute values of pressure jumps across all the interfaces.

Line 8 incorporate regularity indicators at two time points t^n and t^{n+1} into a new error indicator which can be used to guide the hp adaption procedure. It is expected that regions marked by p refinement are smooth regions common for solutions in $[t^n, t^{n+1}]$, which is away from the region through which fronts propagate during $[t^n, t^{n+1}]$. We simply consider taking maximum value of γ^n and γ^{n+1}

$$\gamma_j^{n,n+1} = \max(\gamma_j^{n+1}, \gamma_j^n) \quad (4.36)$$

Line 9 represents explicitly the inputs of error and regularity indicators and the production of a new mesh $\mathcal{G}^{n+1,0}$. This operation generates h -type refinement flags (l_j) and p -type refinement flags (r_j) for each element on \mathcal{G}^c , guiding the generation of the new mesh \mathcal{G}^{n+1} . The p adaption rule is such that an element on \mathcal{G}^n either remains unchanged ($r_j = 0$), or changes its approximation order to $k_j + 1$ ($r_j = 1$). The algorithm involved in $\mathcal{M}_{T, hp}$ can be given by the following flow diagram shown in Figure (4.1).

This hp strategy simply relies on the regularity indicators to make the choice between h and p refinement. When the regularity indicator on an element is smaller than a user-defined parameter γ_r , the solution on the element is considered locally “smooth” and is flagged with p type refinement. Clearly, the choice of γ_r depends on the asymptotic behavior of the solution as well as the resolution of the coarse mesh and hence relies on empirical knowledge.

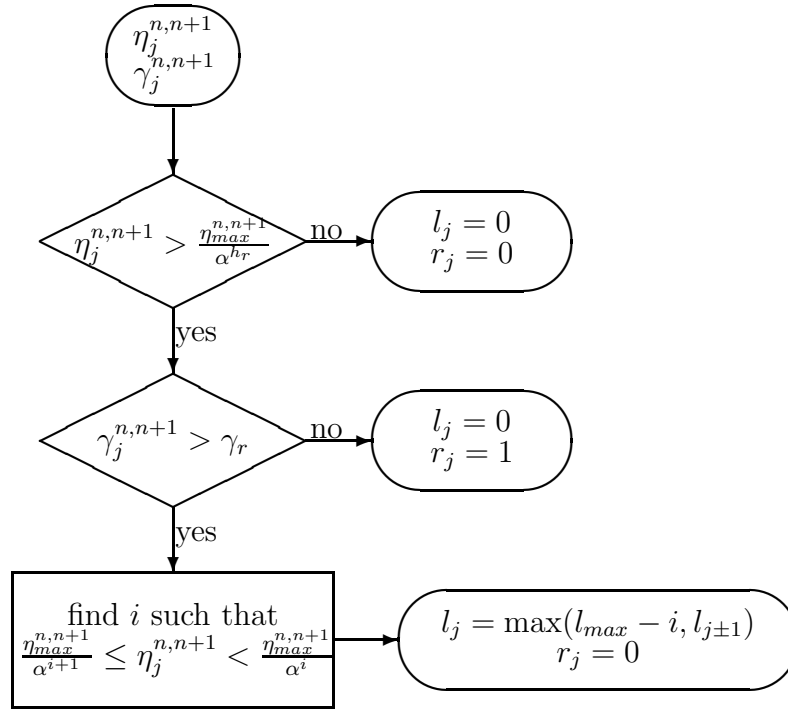


Figure 4.1: Flow diagram for operator $\mathcal{M}_{T,hp}$

4.4 Results

4.4.1 Overview

In order to meet the objectives of this work, we present the numerical results to investigate the various aspects of the adaptive approaches, including both h and hp adaptive LDG-MOL methods. The specific aims of these numerical investigations were (1) to validate the adaptive LDG-MOL approaches and study their convergence characteristics; (2) to compare the performance of the two adaptive strategies considered; and (3) to address various issues regarding the performance of our approach. We detail the test problems and adaptive methods considered, the error and efficiency measures, and the numerical results in the subsections that follow.

4.4.2 Test problems

Table 4.1 summarizes the simulation details for the RE test problems. Problem I is a standard test problem that has been widely used in RE literature [250, 281, 191, 217]. The solid medium properties together with the auxiliary conditions lead to a moderately sharp infiltration front with varying smoothness in solution profiles. Problem II models vertical infiltration with hydrostatic equilibrium as the initial condition. The auxiliary conditions and constitutive relation parameters combine to result in an extremely steep infiltration front in both space and time [217], which poses significant challenges to the robustness and efficiency of many numerical methods. These two test problems are standard benchmark test problem in the RE literature [250, 281, 191, 217].

Table 4.1: Summary of simulation conditions for Problems I–II

Variable	Problem I	Problem II
θ_r (-)	1.020×10^{-1}	9.300×10^{-2}
θ_s (-)	3.680×10^{-1}	3.010×10^{-1}
α_v (m^{-1})	3.350×10^0	5.470×10^0
n_v	2.000×10^0	4.264×10^0
K_s (m/day)	7.970×10^0	5.040×10^0
ρ_0 (kg/m^3)	9.982×10^2	9.982×10^2
d (-)	1.0	1.0
γ ($1/\text{m}$)	4.797×10^{-6}	4.797×10^{-6}
Ω (m)	[0, 0.3]	[0, 10]
t (day)	[0, 0.25]	[0, 0.25]
ψ_0 (m)	-10.0	-z
$\psi^b(0)$ (m)	-10.0	0.0
$\psi^b(z_l)$ (m)	-0.75	0.1
$u^b(z_l)$ (m)	(-)	(-)

4.4.3 Method summary

As a number of investigations have indicated [205, 31, 124, 222], there are several aspects of solution algorithms for RE that can affect the accuracy and efficiency of the numerical method being considered for RE. As a subset of these aspects regarding non-adaptive discretizations for LDG-MOL has been studied in Li et al. [205], we select a fixed set of parameters shown in Table 4.2 regarding these aspects while focusing on investigating the aspects related to the adaptive methods. The application of the adaptive methods is not restricted to these choices.

Table 4.2: Parameters for the LDG-MOL method

Variable	K-level h	Two-level h	Two-level hp
Interior K evaluation	DIR	LIN on \mathcal{G}^c ; DIR on \mathcal{G}	LIN on \mathcal{G}^c ; DIR on \mathcal{G}
k_j	1	1	1-2
Q_M	5	5	$5 + 2(k_j - 1)$
Q_F	3	3	$3 + 2(k_j - 1)$

It has been shown that compared to direct evaluation method for K , K linearization approach leads to more robust, but less accurate solutions [205]. As robustness is the primary concern for the coarse mesh solve in the two-level method, we choose LIN to approximate K in the element interior. For h adaptive methods, we use the linear approximation for elements on the entire mesh. For the hp adaptive method, increases in number of points in quadratures are required for higher order approximations.

We investigated many combinations of the parameters needed for the K-level and two-level adaptive methods. Table 4.3 lists the set of parameters we use for the simulation results we will show. These parameters are user-specified and problem independent.

Table 4.3: Parameters for the adaptive methods

Variable	K-level h	Two-level h	Two-level hp
α	10.0	10.0	10.0
h_c	3.0	(-)	(-)
h_r	2.0	1.0	1.0
r_s	0.8	0.8	0.8
$\gamma_r^{n,n+1}$	(-)	(-)	0.6

For both adaptive methods, we choose an initial mesh containing 25 uniform elements to be the coarsest mesh, based on which spatial adaption is performed. This coarsest mesh also serves as the fixed coarse mesh used by the forward solve for the two-level method. We also restricted our refinement level relative to the coarsest mesh to be 5, which amounts to a minimal mesh size of $z_l/(25 \times 2^5)$.

4.4.4 Efficiency measures

In order to evaluate the approaches considered in this work, three classes of error are often of concern: spatial, temporal, and total spatial-temporal error. As the temporal integration approach we use as well as the temporal error control are well-established, we only focus on spatial error in this study by controlling the temporal error tolerance such that the spatial error dominates the total error.

To compute the error in a numerical solution for RE, one needs a reference solution and measures of the differences between the approximate and reference solutions. In practical applications, analytical solutions to RE are often not possible particularly if one uses realistic p - S - κ relations to simulate various hydrological events with different boundary conditions in heterogeneous field. We use dense grid solutions obtained from continuous cubic-spline approximations of cell-centered FD-MOL solutions [217] computed using a uniform grid spacing consisting of 36,451 nodes and $\epsilon_a = \epsilon_r = 10^{-8}$.

The error between approximate numerical solutions at time t^m with time level m and the corresponding reference solution was quantified in terms of differences in Ψ using discrete L^1 norms with high-order (ten-point) numerical quadrature denoted by $\varepsilon_{L^1}^m$. In order to quantify the spatial error throughout the temporal domain, we integrate the spatial error $\varepsilon_{L^1}^m$ over $[0, T]$ using trapezoidal rule and normalize it with the length of the temporal domain T , which is given by

$$\varepsilon_{T,L^1} = \frac{\sum_{m=1}^{m=m_T} 0.5\Delta t^m (\varepsilon_{L^1}^{m-1} + \varepsilon_{L^1}^m)}{T} \quad (4.37)$$

where m_T is the time level corresponding to T , $\Delta t^m = t^m - t^{m-1}$, $\varepsilon_{L^1}^0$ corresponds to the error in the initial condition so $\varepsilon_{L^1}^0 = 0$. Note that t^m is different from the macroscale time point t^n as t^m is the time point that solution is needed for error calculation so they can be chosen arbitrarily without impact on the performance of the adaptive methods we consider. For convenience, we use uniform time interval $\Delta t^m = 0.025$ day.

In order to investigate the performance of our proposed adaptive methods, we compare our spatially adaptive LDG methods with a fixed uniform LDG discretization method. Our goal is to achieve the same accuracy as the uniform LDG method using a minimal number of degrees of freedom and minimal CPU work time. We therefore consider the mean of number of degrees of freedom at each macroscale time step

$$N_{dofs} = \frac{\sum_{n=1}^{n=n_T} N_{dofs}^n}{n^T} \quad (4.38)$$

where N_{dofs}^n is the number of degrees of freedom used at time t^n . N_{dofs} adjusts the changes in number of degrees of freedom caused by h adaption and hp adaption. We also consider CPU time as it is the ultimate quantity we aim to minimize.

Table 4.4: Summary of adaptive simulation conditions for Problem I

Run [†]	Method	τ_t	τ_s	l_{max}
1[a,b,c,d,e,f]	Uniform	(-)	(-)	0, 1, 2, 3, 4, 5
2[a,b,c,d,e]	K-level, Non-iterative	0.25	(-)	1, 2, 3, 4, 5
3[a,b,c,d,e]	K-level, Iterative	0.25	1.0, 0.5, 0.2, 0.1, 0.05	1
4[a,b,c,d,e]	Two-level, h Adaptive	0.25	(-)	1, 2, 3, 4, 5
5[a,b,c,d,e]	K-level, Iterative	0.15	1.0, 0.5, 0.2, 0.1, 0.05	1
6[a,b,c,d,e]	Two-level, hp Adaptive	0.25	(-)	1, 2, 3, 4, 5

[†] alphabetical qualifier corresponds to the spatial discretization given by l_{max} for the uniform method, the non-iterative K-level method and the two-level method, and τ_s for the iterative K-level method

4.4.5 Numerical results

4.4.5.1 Problem I

Table 4.4 summarizes the simulation parameters in our numerical experiments for solving Problem I using the adaptive methods we propose. Different discretization levels are obtained by varying l_{max} for the non-iterative K-level method and the two-level method. For the iterative K-level method, we varied the spatial tolerance τ_s with $l_{max} = 1$. While the choice of l_{max} for the iterative K-level method is not optimal, the setting demonstrates the performance of our methods and facilitate numerical comparisons.

Figures 4.2 and 4.3 show the pressure head profiles and the corresponding mesh at time points $t^n, n = 1, \dots, t^n$ using the K-level method (Run 5b) and the two-level method (Run 4c) with h adaption, respectively. It is readily seen that the infiltration front for this problem displays varying smoothness across the spatial domain. The infiltration front also travels with time while maintaining similar shape. Both the K-level and two-level adaptive approaches generated adaptive meshes capable of producing better resolution around the fronts. The mesh used in the K-level approach is self-adaptive, leading to highly resolved

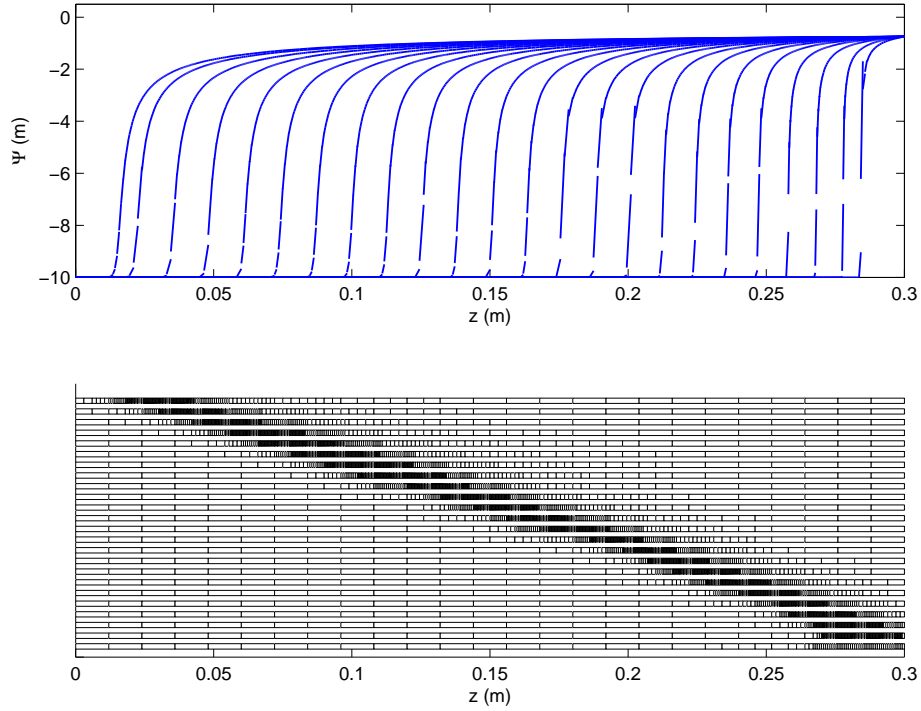


Figure 4.2: Pressure head solutions by h K-level method for Problem I

region around the fronts. The buffering approach extended the refinement region and successfully enclosed sharp features of the solution in refined region. Compared to the K-level approach, the two-level method employs an error indicator formally incorporating the temporal behavior of the solution. As a result, the two-level approach maintains a uniformly distributed finer region between solutions at two consecutive time levels.

Figures 4.4 and 4.5 show the error measure ε_{T,L^1} with respect to N_{dofs} and CPU time, respectively, for the h adaptive approaches listed in Table 4.4. From Figure (4.4), we observe that all adaptive approaches achieved similar levels of accuracy as the uniform discretization approach using many fewer N_{dofs} . For the K-level method, the iterative approach attempted to control the error for Ψ^{n+1} by redistributing the elements based on solutions at t^{n+1} , and thus led to more economical mesh than the non-iterative method. However, the additional computational expense associated with iterative solves significantly increased

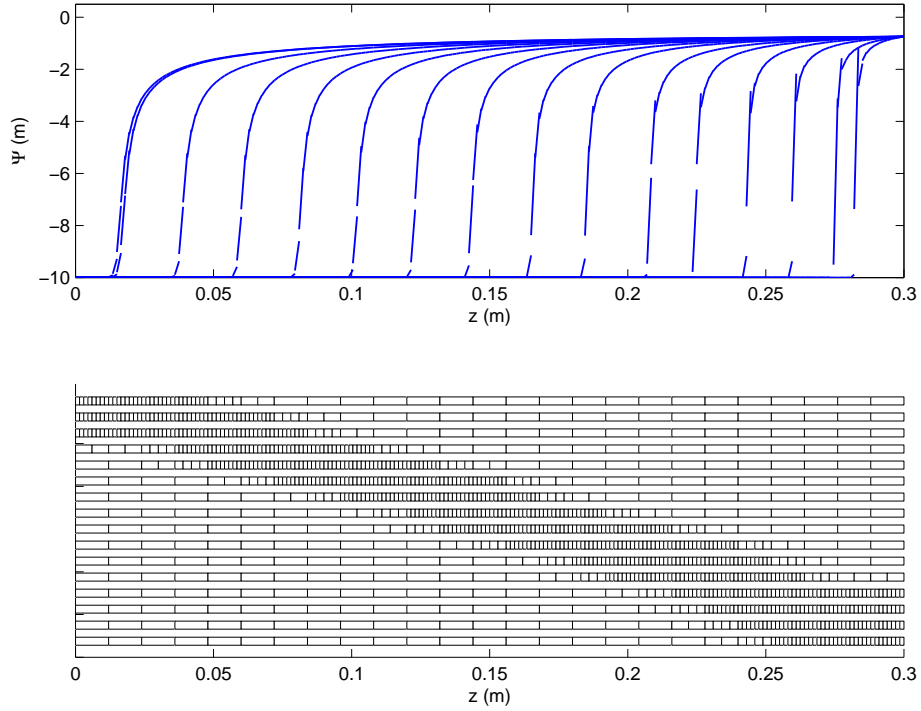


Figure 4.3: Pressure head solutions by h two-level method for Problem I

the total CPU time, as shown in Figure (4.5). On the other hand, the two-level method uses 30-60% fewer N_{dofs} compared to the uniform discretization method to achieve comparable accuracy. Because the computational overhead caused by the extra coarse solve required by the two-level method is more significant for simulations with low resolution, the computational advantages for the two-level method deteriorated at low refinement levels.

We also found that for the iterative K-level method with a macroscale time step tolerance $\tau_t = 0.25$, the buffer region was not able to enclose the front completely at some macroscale time levels. This resulted in poor accuracy and slow convergence at finer discretization level. As expected, this situation was improved by using a tighter tolerance $\tau_t = 0.15$, as shown in Figures 4.4 and 4.5.

Figure (4.6) shows the pressure head solutions at $t^n, n = 1, \dots, n_T$ and the corresponding mesh using the two-level hp adaptive approach. Elements using quadratic approximations are indicated in blue. Figures 4.7 and 4.8 show the con-

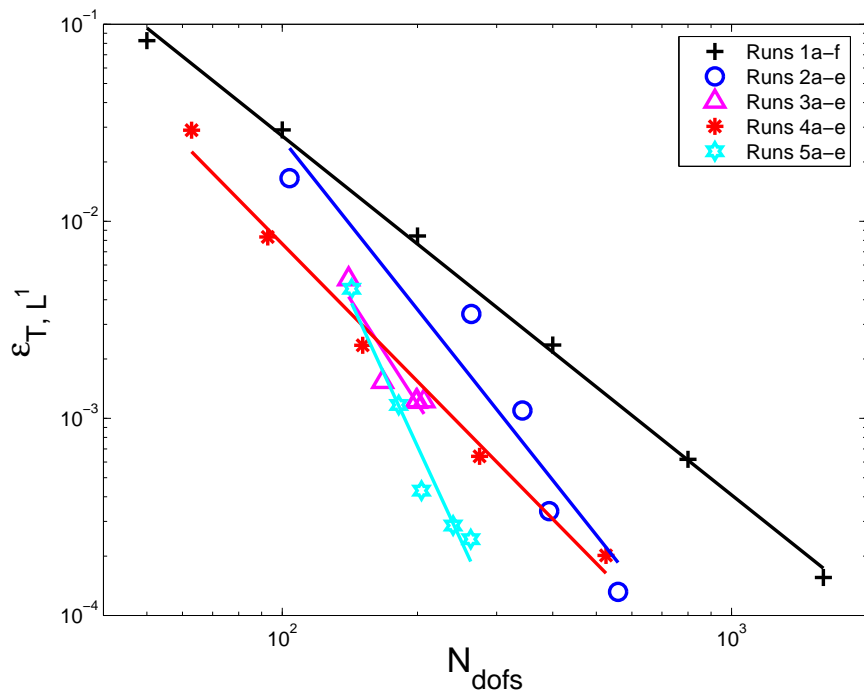


Figure 4.4: Convergence rates of the K-level and two-level methods for Problem I

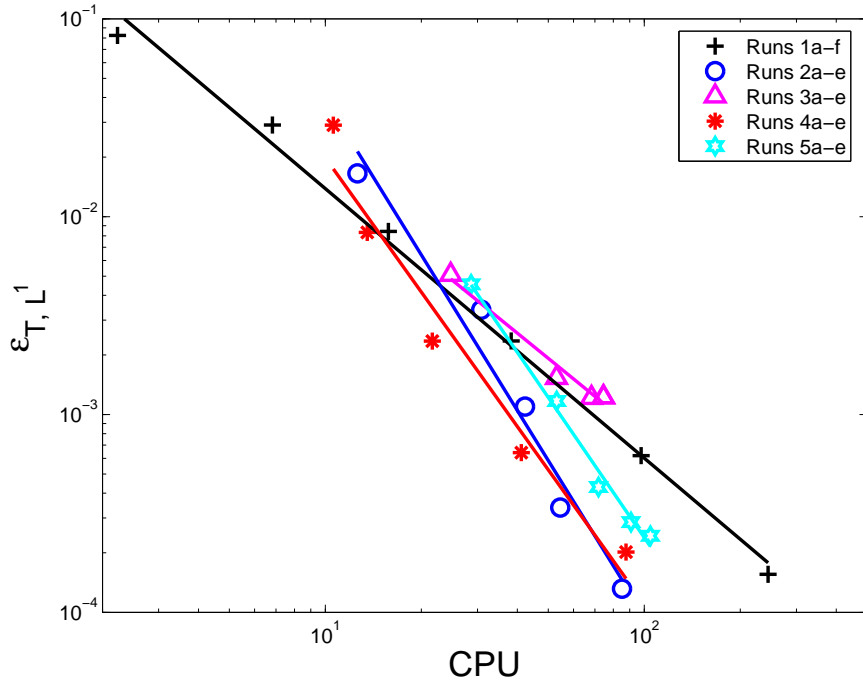


Figure 4.5: Convergence rates of the K-level and two-level methods for Problem I

vergence rates of this approach in comparison with the pure h two-level adaptive approach. We observe that, like the pure h adaptive method, the sharp fronts are resolved by h refinement region; however, instead of having regions with variably refined elements behind the front, higher order elements are used to resolve the smooth feature in the solution. As a result, combination of hp adaptive strategy further reduced the N_{dofs} needed to reach the same accuracy up to 15%. However, the significant reduction in N_{dofs} did not transform to equally significant reduction in CPU time as indicated in Figure (4.8). This is due to the increased number of quadrature points required to evaluate the integrals in Eqns (4.17) and (4.19) and consequently more expensive banded linear solves.

4.4.5.2 Problem II

Table 4.5 summarizes the numerical experiments we performed to solve Problem IV using adaptive methods proposed. Figures 4.9 and 4.10 show the pressure

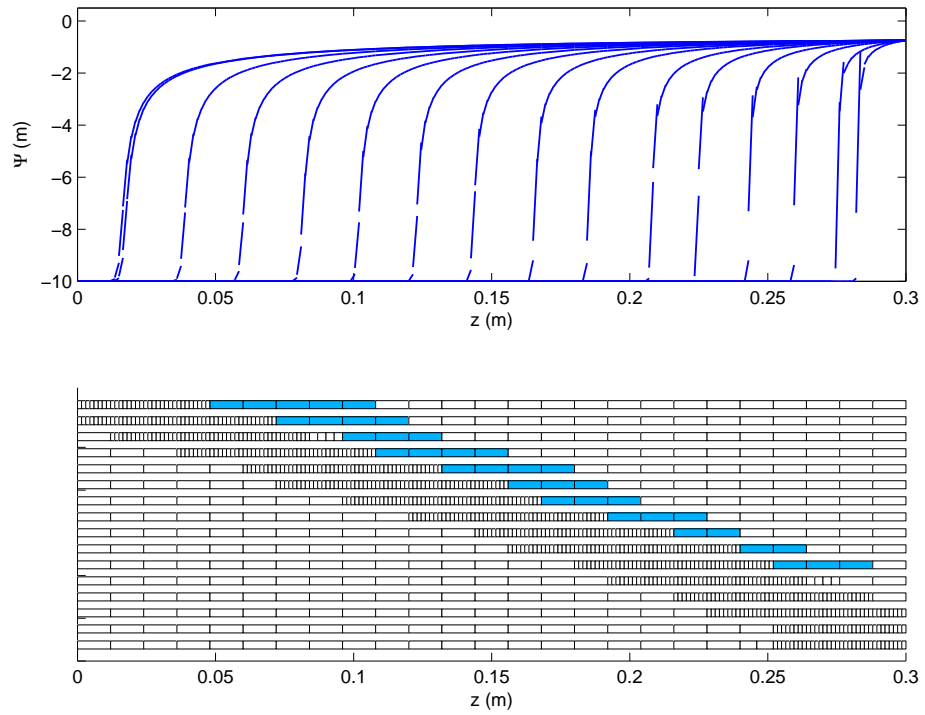


Figure 4.6: Pressure head solutions by hp two-level method for Problem I

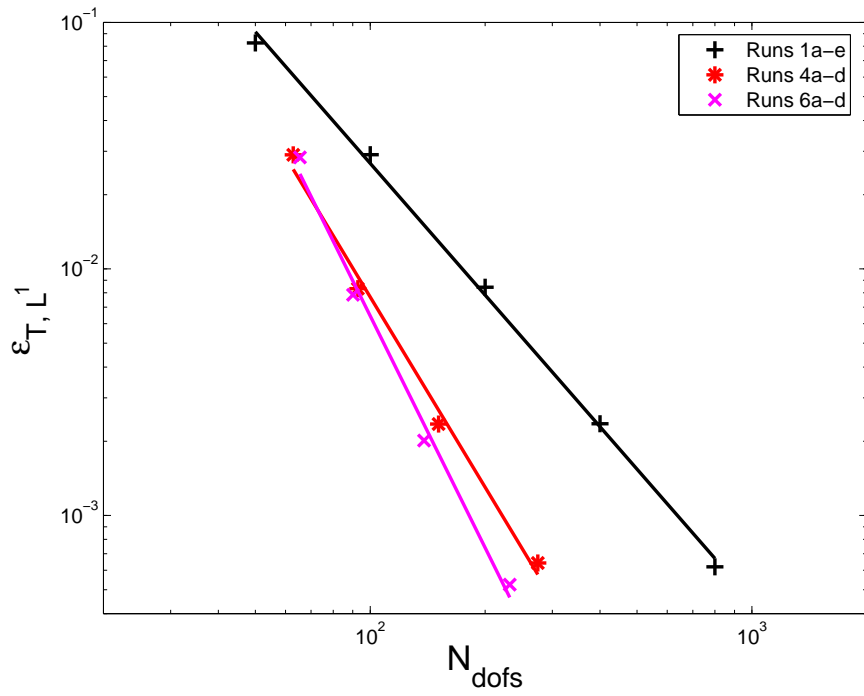


Figure 4.7: Comparison of the h and hp adaptive methods for Problem I

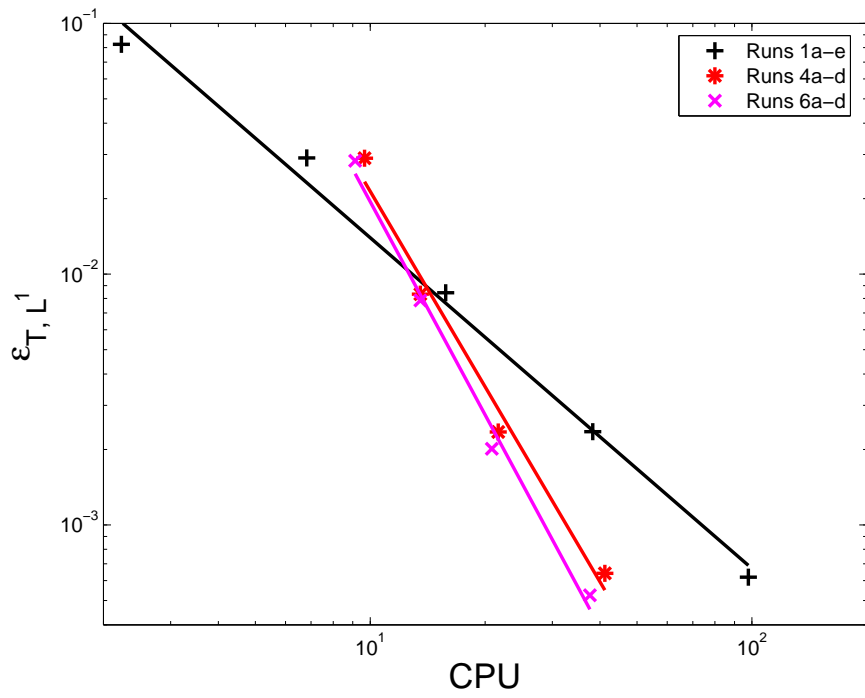


Figure 4.8: Comparison of the h and hp adaptive methods for Problem I

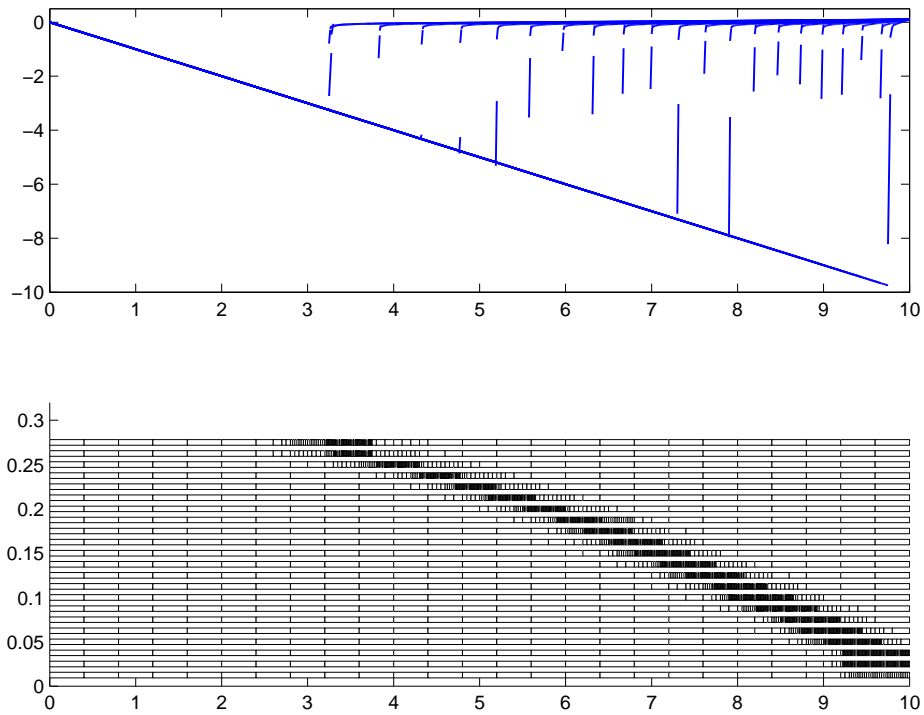


Figure 4.9: Pressure head solutions by h K-level method for Problem II

Table 4.5: Summary of adaptive simulation conditions for Problem II

Run [†]	Method	τ_t	τ_s	l_{max}
7[a,b,c,d,e,f]	Uniform	(-)	(-)	0, 1, 2, 3, 4, 5
8[a,b,c,d,e]	K-level, Non-iterative	3.0	(-)	1, 2, 3, 4, 5
9[a,b,c,d,e]	K-level, Iterative	3.0	0.2, 0.1, 0.05, 0.02, 0.01	1
10[a,b,c,d,e]	Two-level, h Adaptive	4.0	(-)	1, 2, 3, 4, 5

[†] alphabetical qualifier corresponds to the spatial discretization given by l_{max} for the uniform method, the non-iterative K-level method and the two-level method, and τ_s for the iterative K-level method

head solutions at macroscale time points from Run 9e and Run 10c, respectively. It can be observed that the infiltration fronts are so sharp that even with highly refined region around the front, only two or three elements are located on the front. As with Problem I, both the K-level method and two-level method produced meshes that effectively followed the dynamics of the problem and provided highly refined regions around the front. The self-adaptive K-level method led to highly localized finer meshes around the front. On the other hand, the two-level method results in meshes with a relatively uniform refined region between the fronts at t^n and t^{n+1} . The refined region tends to be larger than that from the K-level due to the fact that it relies on a forward coarse mesh solve, which is robust yet diffusive due to the linearization of K [205].

Figures 4.11 and 4.12 compares the accuracy and efficiency of the K-level method, two-level method, and the uniform non-adaptive method for this test problem. We observed that both the K-level and two-level method achieved significantly improved accuracy in terms of both N_{dofs} and CPU time. As can be observed from Figure (4.11), the iterative K-level method, together with a suitably chosen τ_t , produced the most economical mesh among all the methods. Although the iterations added to the computational expense, it clearly achieved an overall computational advantage over the uniform non-adaptive method. For the non-iterative K-level method, we found a convergence artifact appearing with

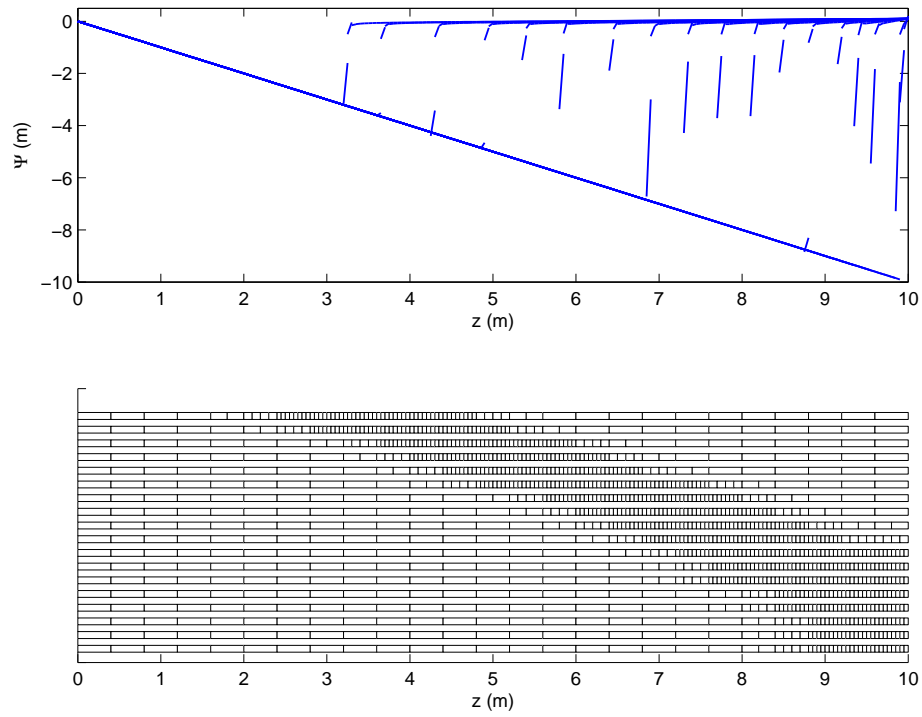


Figure 4.10: Pressure head solutions by h two-level method for Problem II

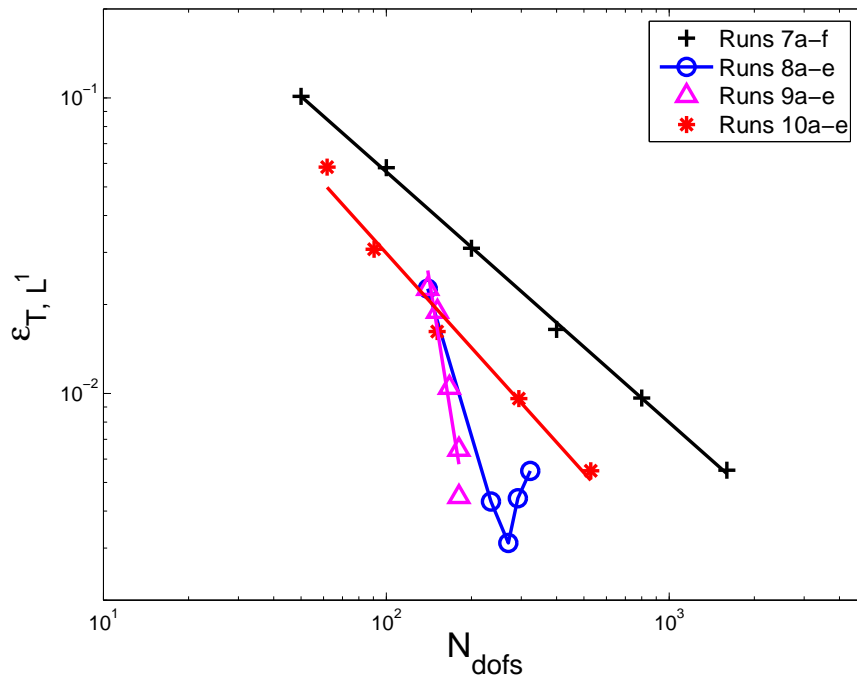


Figure 4.11: Convergence rates of the K-level and two-level methods for Problem II

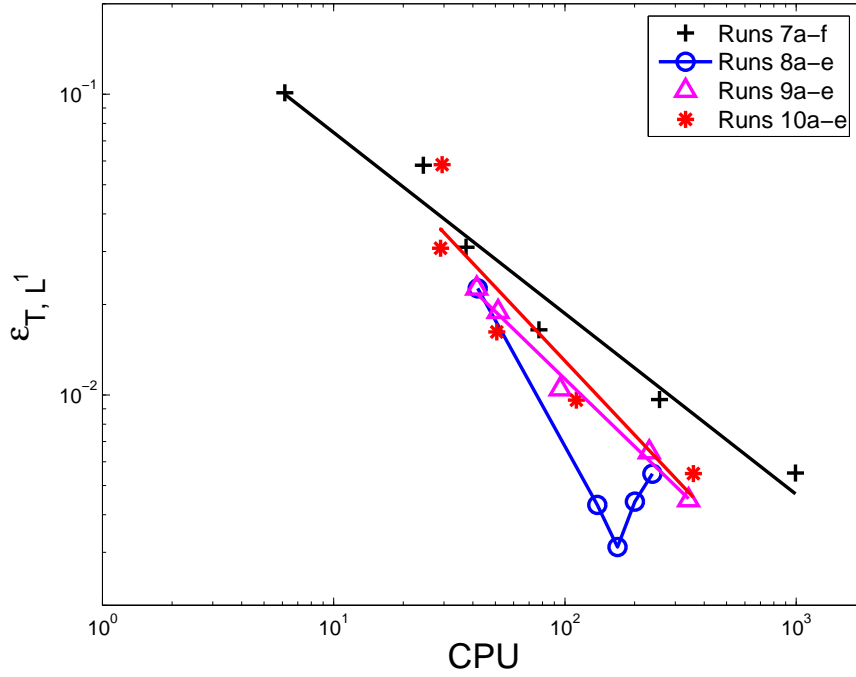


Figure 4.12: Convergence rates of the K-level and two-level methods for Problem II

$l_{max} = 2, 3, 4$ and more obviously with $l_{max} = 3$. After examining the solution profiles at various time points, we found that this is due to cancellation of error during the simulation. For instance, with $l_{max} = 3$ at $t = 0.025$ (day), the front obtained from the non-iterative K-level method was slightly behind the reference solution at the same time point. This effect, coupled with the numerical diffusion in the numerical solution caused error cancellation and therefore generated less error than expected. As we adaptively refined our mesh, e.g. to $l_{max} = 5$, this effect disappeared.

As observed for Problem I, we found that the two-level method generated uniformly refined region around the steep front and achieved the same level of accuracy as the uniform non-adaptive method at comparable levels of discretization. We found that the accuracy of the two-level method was not sensitive to the choice of τ_t because the forward coarse solve was sufficiently robust to locate the front position at the next time level. In contrast, the K-level method relied

on buffer regions with fixed width to extend the refined region. As a result, when the fronts traveled beyond the refined region, the accuracy of the method deteriorated significantly.

We also ran simulations for this problem using the hp two-level method and found that the hp two-level method did not lead to significant computational advantages for this problem. This is not surprising since the spatial error was dominated by the extremely sharp fronts to a larger extent than Problem I. As a result, the smooth region in which p refinement could offer potential advantages is substantially limited.

4.4.6 Discussion

Our computational results show that both the K-level and two-level adaptive approaches produced economical meshes and hence significant savings in computational time compared to a uniform discretization approach. The K-level method is self-adaptive, resulting in highly refined regions around the infiltration fronts. This method, together with a buffering technique and appropriate macroscale time steps is effective in solving challenging RE problems. The two-level method relies on a coupled space-time error indicator based on a formal forward solve to guide the mesh generation. It achieved comparable accuracy to the non-adaptive method at comparable discretization levels with significantly decreased computational expense. Overall, we believe that predicting the front evolution at future time and incorporating the predicted information into the adaptive methods plays a key role in the overall success of the adaptive methods for many classes of variably saturated flow problems.

We found that although the K-level method can be effective with a set of appropriately chosen parameters such as τ_t , it is somewhat sensitive to these choices, which renders this method not as robust as the two-level method. On the other hand, iterative solution approaches with error control can be naturally built into the K-level method, whereas the mechanism is currently lacking for

the two-level method. The iterative K-level method is certainly not optimal in this study and advances should be pursued in these directions: (1) developing more rigorous space-time error estimators with strict bounds for the true error for RE; and (2) designing more efficient mechanisms for coupling spatial and temporal adaption. We believe the advantageous aspects in both the K-level and two-level method can be integrated to lead to more advanced adaptive methods. This topic deserves further study.

Since the spatial error around the sharp fronts dominated the total error, the advantage of an hp adaptive method only led to moderate CPU savings compared to pure h adaption for Problem I. For Problem II where the extremely steep fronts dominated the solution evolution, no computational advantage was observed. Overall, the hp approach was able to reach the same level of accuracy at no more computational expense than the h adaptive method.

Because the focus this paper was not to investigate different LDG-MOL schemes, we only showed results using one-sided numerical fluxes with fixed conductivity evaluation methods. However, our adaptive methods are not restricted to the particular choice of this LDG method. Advantages in terms of computational work can also be achieved using, for instance, average numerical fluxes with other conductivity evaluation methods. The performance of different LDG schemes on the adaptive mesh was consistent with our previous investigations [205].

We implemented and investigated a series of error indicators/estimators along with the Kelly indicator, including pressure gradient indicator, saturation gradient indicator [217], and an *a posteriori* error estimator developed for LDG discretizations of nonlinear elliptic problems [54]. We found that the gradient indicators were able to produce meshes around the fronts for the test problems we considered. However, these gradient indicators were not asymptotic and led in some cases to additional refined regions near the water table where there were static capillary fronts with relatively low error [217]. On the other hand, the *a*

posteriori error estimator and the Kelly indicator were more robust and efficient error measures and both performed well for the problems we considered.

4.4.7 Conclusions

While a fully automatic adaptive method with formal spatial and temporal error control is highly desirable, it is a challenging and certainly a long-range task. Towards this direction, we have the following conclusions based on this work:

- h and hp adaptive LDG methods used within an MOL framework can offer significantly increased efficiency for RE problems in one dimension.
- The K-level and two-level spatial adaptive methods can both achieve substantial savings in computational effort and a large reduction in the mean number of degrees of freedom compared to a uniform spatial discretization.
- The hp two-level adaptive approach offers moderate savings in terms of computational effort because (1) the RE problems under consideration have dominant spatial errors around the steep fronts with limited smooth region needed for p adaption to be superior; and (2) higher order p refinement requires more computational effort due to the intrinsic, high nonlinearity of RE and hence compromises the computational advantages.
- The proposed adaptive methods need further evaluation and development. Additional advances can be made in these areas: (1) implementation and investigation in higher dimension and larger scales; and (2) development of more rigorous spatial and temporal error control mechanisms.

Chapter 5

Summary and Recommendations

This chapter summarizes the dissertation research and recommends potential directions for future research. Our research focuses on improving models of flow and transport in porous medium systems using numerical modeling approaches at the pore scale and continuum scale. Specifically, the issues examined in this work include addressing: (1) deficiencies in using conventional Darcy’s law and the generalized model to describe two-phase flow in porous media; (2) dependence of two-phase flow on a broad range of flow parameters including capillary number, wettability, and viscosity ratio; (3) validity of using interfacial area as an additional variable to improve the multiphase flow models; (4) formulation of the LDG methods to improve numerical solution techniques for the traditional air-water phase model represented by RE; and (5) extension to spatially adaptive LDG-MOL methods to further improve the efficiency of the proposed LDG-MOL method. These issues are investigated through a series of numerical studies, which are summarized below.

5.1 Summary

In Chapter 2, deficiencies of the traditional Darcy’s law in modeling two-phase flow and a resulting phenomenon—viscous coupling, were investigated using a three-dimensional, two-fluid-phase MRT-LB model. Simulation of co-current

flow through a sphere-pack porous medium was performed and correlations of the relative permeabilities as a function of capillary number, wettability, and fluid viscosities were obtained. The results were qualitatively consistent with experimental observations. In addition, a strong correlation between the relative permeability and interfacial area between fluids was found, indicating that both the common extension of Darcy’s law and the generalized formulation accounting for viscous coupling effects do not provide adequate insight into two-phase flow processes in porous media. This work lends additional support for the hypothesis that interfacial area is a key variable for multiphase flow in porous medium systems.

Chapter 3 aimed at developing robust and efficient numerical solution techniques to reduce numerical errors during application of numerical methods for solving models in porous medium systems. An LDG-MOL spatial approximation combined with a robust and established variable order, variable step-size backward difference method was formulated for RE. A variety of approximations at discontinuous element edge boundaries, permeability approximations, and numerical quadrature schemes were examined. The results discussed in Chapter 4 demonstrated that the proposed LDG-MOL approach is robust and efficient for a range of common RE problems.

While the non-adaptive LDG-MOL approach demonstrated good performance for RE in Chapter 4, the subsequent work discussed in Chapter 5 further developed effective spatially adaptive LDG methods to improve the efficiency of the LDG-MOL simulator. Specifically, two adaptive LDG-MOL approaches—a straightforward adaptive strategy for finite element methods and a novel and effective adaptive approach based on a coarse-grid solve—were developed and implemented. Numerical comparisons in Chapter 4 indicated that the spatially adaptive LDG method coupled with advanced and mature time integration through MOL, is a promising numerical technique that can offer significant computational advantages over the non-adaptive counterparts.

5.2 Recommendations

Based on the dissertation research, several avenues for future research appear promising. Specifically, we provide the following recommendations.

- While the LB simulator used in Chapter 2 incorporated high-performance LB implementation including parallelization, computational challenges remain when using LB to simulate porous medium flow and transport processes at larger scales. It is important to continue the development of more efficient algorithms (e. g. adaptive LB) and codes [239, 279].
- As demonstrated in this dissertation, pore-scale studies have significant merits in improving our understanding of various mechanisms and processes in porous media. A challenging aspect involves appropriately incorporating this understanding with more advanced models where numerical models can be applied to develop better answers to many practical problems [147, 221]. This area of research deserves further attention.
- The proposed adaptive LDG-MOL methods need further evaluation and development. Additional advances can be made in the following areas: (1) implementation and investigation in higher dimensions and at larger scales; (2) development of more rigorous spatial and temporal error control mechanisms; and (3) coupling of the m adaptive method, in which different numerical methods, such as DG and CG, are adaptively used to achieve improved performance.

REFERENCES

- [1] L. M. Abriola and J. R. Lang. Self-adaptive hierarchic finite element solution of the one-dimensional unsaturated flow equation. *International Journal for Numerical Methods in Fluids*, 10:227–246, 1990.
- [2] P. M. Adler. *Porous Media: Geometry and Transports*. Butterworth-Heinemann, Boston, 1992.
- [3] P. M. Adler, C. J. Jacquin, and J. A. Quiblier. Flow in simulated porous media. *International Journal of Multiphase Flow*, 16:691–712, 1990.
- [4] U.S. Environmental Protection Agency. Environmental standard for the management and disposal of spent nuclear fuel, high-level and transuranic radioactive wastes. *Federal Register*, 1982.
- [5] M. Ainsworth and J. T. Oden. A posteriori error estimation in finite element analysis. *Computer Methods in Applied Mechanics and Engineering*, 142(1-2):1–88, 1997.
- [6] M. Ainsworth and B. Senior. Aspects of an adaptive hp-finite element method: Adaptive strategy, conforming approximation and efficient solvers. *Computer Methods in Applied Mechanics and Engineering*, 150(1-4):65–87, 1997.
- [7] V. Aizinger, C. N. Dawson, B. Cockburn, and P. Castillo. The local discontinuous Galerkin method for contaminant transport. *Advances in Water Resources*, 24(1):73–87, 2000.
- [8] J. E. Akin and M. Singh. Object-oriented fortran 90 p-adaptive finite element method. *Advances in Engineering Software*, 33:461–468, 2002.
- [9] S. R. Allmaras and M. B. Giles. A coupled Euler/Navier-Stokes algorithm for 2-D unsteady transonic flows. In *Aerospace Sciences Meeting*, volume 17, Reno, NV, 1989.
- [10] T. Arbogast, C. N. Dawson, P. T. Keenan, M. F. Wheeler, and I. Yotov. Enhanced cell-centered finite differences for elliptic equations on general geometry. *SIAM Journal on Scientific Computing*, 19(2):404–425, 1998.
- [11] T. Arbogast, M. F. Wheeler, and N. Y. Zhang. A nonlinear mixed finite element method for a degenerate parabolic equation arising in flow in porous media. *SIAM Journal on Numerical Analysis*, 33(4):1669–1687, 1996.
- [12] J. S. Archer and S. W. Wong. Use of a reservoir simulator to interpret laboratory waterflood data. *Soc. Petrol. Eng. J.*, 12:343–347, 1973.

- [13] D. N. Arnold. Mixed finite element methods for elliptic problems. *Computer Methods in Applied Mechanics and Engineering*, 82:281–300, 1990.
- [14] D. N. Arnold, F. Brezzi, B. Cockburn, and L. D. Marini. Unified analysis of discontinuous Galerkin methods for elliptic problems. *SIAM Journal on Numerical Analysis*, 39(5):1749–1779, 2002.
- [15] J. L. Auriault and J. Lewandowska. On the cross-effects of coupled macroscopic transport equations in porous media. *Transport in Porous Media*, 16(1):31–52, 1994.
- [16] D. G. Avraam, G. B. Kolonis, T. C. Roumeliotis, G. N. Constantinides, and A. C. Payatakes. Steady-state 2-phase flow through planar and nonplanar model porous media. *Transport in Porous Media*, 16(1):75–101, 1994.
- [17] D. G. Avraam and A. C. Payatakes. Flow regimes and relative permeabilities during steady-state two-phase flow in porous media. *Journal of Fluid Mechanics*, 293:207–236, 1995.
- [18] D. G. Avraam and A. C. Payatakes. Generalized relative permeability coefficients during steady-state two-phase flow in porous media, and correlation with the flow mechanisms. *Transport in Porous Media*, 20(1-2):135–168, 1995.
- [19] D. G. Avraam and A. C. Payatakes. Flow mechanisms, relative permeabilities, and coupling effects in steady-state two-phase flow through porous media, the case of strong wettability. *Industrial and Engineering Chemistry Research*, 38(3):778–786, 1999.
- [20] M. Ayub and R. G. Bentsen. Interfacial viscous coupling: A myth or reality? *Journal of Petroleum Science and Engineering*, 23(1):13–26, 1999.
- [21] I. Babuska, C. E. Baumann, and J. T. Oden. A discontinuous hp finite element method for diffusion problems: 1-d analysis. *Computers & Mathematics with Applications*, 37(9):103–122, 1999.
- [22] I. Babuska and W. C. Rheinboldt. A posteriori error analysis of finite element solutions for one-dimensional problems. *SIAM Journal on Numerical Analysis*, 18(3):565–589, 1981.
- [23] I. Babuska and M. Suri. The p and h-p versions of the finite-element method, basic principles and properties. *Siam Review*, 36(4):578–632, 1994.
- [24] Y. Bachmat and J. Bear. Macroscopic modelling of transport phenomena in porous media. 1: The continuum approach. *Transport in Porous Media*, 1(3):213–240, 1986.
- [25] A. Baggag, H. Atkins, and D. Keyes. Parallel implementation of the discontinuous Galerkin method. Technical Report NASA/CR-1999-209546, ICASE Report No. 99-35, 1999.
- [26] F. Bassi and S. Rebay. A high-order accurate discontinuous finite element method for the numerical solution of the compressible Navier-Stokes equations. *Journal of Computational Physics*, 131:267–279, 1997.

- [27] P. Bastian. Higher order discontinuous Galerkin methods for flow and transport in porous media. In E. Bnsch, editor, *Challenges in Scientific Computing*, 2003.
- [28] P. Bastian and V. Reichenberger. Multigrid for higher order discontinuous Galerkin finite elements applied to groundwater flow. Technical Report 2000-37, SFB 359, 2000.
- [29] C. E. Baumann and J. T. Oden. A discontinuous *hp* finite element method for the solution of the Euler equations of gas dynamics. In M. Hafez and H. J. C., editors, *Proceedings of the 10th International Conference on Finite Elements in Fluids*, 1998.
- [30] C. E. Baumann and J. T. Oden. A discontinuous *hp* finite element method for the Euler and Navier-Stokes equations. *International Journal for Numerical Methods in Fluids*, 31(1):79–95, 1999.
- [31] M. Bause and P. Knabner. Computation of variably saturated subsurface flow by adaptive mixed hybrid finite element methods. *Advances in Water Resources*, 27:565–581, 2004.
- [32] J. Bear. *Dynamics of Fluids in Porous Media*. Elsevier, New York, 1972.
- [33] J. Bear and Y. Backmat. Macroscopic modeling of transport phenomena in porous media: 2. application to mass, momentum and energy transport. *Transport in Porous Media*, 1:241–269, 1986.
- [34] J. Bear, M. S. Beljin, and R. R. Ross. Fundamentals of ground-water modeling. Technical Report EPA/540/S-92/005, US EPA Robert S. Kerr Environmental Research Laboratory, Ada, OK, 1992.
- [35] P. B. Bedient, H. S. Rifai, and C. J. Newell. *Ground water contamination*. Prentice Hall, 1999.
- [36] R. G. Bentsen. An investigation into whether the nondiagonal mobility coefficients which arise in coupled, 2 phase flow are equal. *Transport in Porous Media*, 14(1):23–32, 1994.
- [37] R. G. Bentsen. Effect of momentum transfer between fluid phases on effective mobility. *Journal of Petroleum Science and Engineering*, 21:27–42, 1998.
- [38] R. G. Bentsen. Influence of hydrodynamic forces and interfacial momentum transfer on the flow of two immiscible phases. *Journal of Petroleum Science and Engineering*, 19:177–190, 1998.
- [39] R. G. Bentsen and A. A. Manai. On the use of conventional cocurrent and countercurrent effective permeabilities to estimate the four generalied permeability coefficients which arise in coupled, two-phase flow. *Transport in Porous Media*, 11:243–262, 1993.
- [40] R. G. Bentsen and A. A. Manai. On the use of conventional cocurrent and countercurrent effective permeabilities to estimate the four generalized permeability coefficients which arise in coupled, two-phase flow. *Transport in Porous Media*, 11(3):243–262, 1993.

- [41] L. Bergamaschi and M. Putti. Mixed finite elements and Newton-type linearizations for the solution of Richards' equation. *International Journal for Numerical Methods in Engineering*, 45:1025–1046, 1999.
- [42] R. C. Berger and S. E. Howington. Discrete fluxes and mass balance in finite elements. *Journal of Hydraulic Engineering*, 128(1):87–92, 1999.
- [43] J. G. Berryman. Measurement of spatial correlation functions using image processing techniques. *Journal of Applied Physics*, 57(7):2374–2384, 1985.
- [44] J. G. Berryman and S. C. Blair. Use of digital image-analysis to estimate fluid permeability of porous materials - Application of 2-point correlation-functions. *Journal of Applied Physics*, 60(6):1930–1938, 1986.
- [45] K. S. Bey and J. T. Oden. hp-version discontinuous galerkin methods for hyperbolic conservation laws. *Computer Methods in Applied Mechanics and Engineering*, 133(3-4):259–286, 1996.
- [46] K. S. Bey, J. T. Oden, and A. Patra. A parallel hp-adaptive discontinuous galerkin method for hyperbolic conservation laws. *Applied Numerical Mathematics*, 20(4):321–336, 1996.
- [47] K. S. Bey, A. Patra, and J. T. Oden. Hp-version discontinuous galerkin methods for hyperbolic conservation-laws - a parallel adaptive strategy. *International Journal for Numerical Methods in Engineering*, 38(22):3889–3908, 1995.
- [48] C. A. Blain and T. C. Massey. Application of a coupled discontinuous-continuous galerkin finite element shallow water model to coastal ocean dynamics. *Ocean Modelling*, 10(3-4):283–315, 2005.
- [49] A. G. Botset. Flow of gas-liquid mixtures through consolidated sand. *Trans. A.I.M.E.*, 136:91–108, 1940.
- [50] B. J. Bourbiaux and F. Kalayjian. Experimental study of cocurrent and countercurrent flows in natural porous media. *SPE*, 5:361–368, 1990.
- [51] K. E. Brenan, S. L. Campbell, and L. R. Petzold. *The Numerical Solution of Initial Value Problems in Differential-Algebraic Equations*. Society for Industrial and Applied Mathematics, Philadelphia, PA, 1996.
- [52] R. H. Brooks and A. T. Corey. Properties of porous media affecting fluid flow. *Journal of the Irrigation and Drainage Division, Proceedings of the American Society of Civil Engineers*, IR2:61–88, 1966.
- [53] A. Burbeau and P. Sagaut. A dynamic p-adaptive discontinuous galerkin method for viscous flow with shocks. *Computers & Fluids*, 34(4-5):401–417, 2005.
- [54] R. Bustinza, G. N. Gatica, and B. Cockburn. An a posteriori error estimate for the local discontinuous galerkin method applied to linear and nonlinear diffusion problems. *Journal of Scientific Computing*, 22(1):147–185, 2005.

- [55] W. M. Cao, W. Z. Huang, and R. D. Russell. An error indicator monitor function for an r-adaptive finite-element method. *Journal of Computational Physics*, 170(2):871–892, 2001.
- [56] P. Castillo. Performance of discontinuous Galerkin methods for elliptic pdes. *SIAM Journal on Scientific Computing*, 24(2):524–547, 2002.
- [57] P. Castillo. An a posteriori error estimate for the local discontinuous galerkin method. *Journal of Scientific Computing*, 22(1):187–204, 2005.
- [58] P. Castillo, B. Cockburn, I. Perugia, and D. Shotzau. An a priori error analysis of the local discontinuous Galerkin method for elliptic problems. *SIAM Journal on Numerical Analysis*, 38(5):1676–1706, 2000.
- [59] M. A. Celia, E. T. Bouloutas, and R. L. Zarba. A general mass-conservative numerical solution for the unsaturated flow equation. *Water Resources Research*, 26(7):1483–1496, 1990.
- [60] M. A. Celia, H. Rajaram, and L. A. Ferrand. A multi-scale computational model for multiphase flow in porous media. *Advances in Water Resources*, 16(1):81–92, 1993.
- [61] G. Chavent and B. Cockburn. The local projection p^0 - p^1 -discontinuous-Galerkin finite-element method for scalar conservation-laws. *Rairo-Mathematical Modelling and Numerical Analysis-Modelisation Mathematique Et Analyse Numerique*, 23(4):565–592, 1989.
- [62] G. Chavent and J. Jaffré. *Mathematical Models and Finite Elements for Reservoir Simulation*. North-Holland, Amsterdam, 1986.
- [63] G. Chavent and J. E. Roberts. A unified physical presentation of mixed, mixed-hybrid finite elements and standard finite difference approximations for the determination of velocities in waterflow problems. *Advances in Water Resources*, 14(6):329–348, 1991.
- [64] G. Chavent and G. Salzano. A finite-element method for the 1-D water flooding problem with gravity. *Journal of Computational Physics*, 45(3):307–344, 1982.
- [65] Z. Chen and R. E. Ewing. From single-phase to compositional flow: Applicability of mixed finite elements. *Transport in Porous Media*, 27:225–242, 1997.
- [66] Z. Chen and R. E. Ewing. Fully discrete finite element analysis of multiphase flow in groundwater hydrology. *SIAM Journal on Numerical Analysis*, 34(6):2228–2253, 1997.
- [67] Y. L. Chiang, B. van Leer, and K. G. Powell. Simulation of unsteady inviscid flow on an adaptively refined cartesian grid. In *AIAA*, 1992.
- [68] J. Chin, E. S. Boek, and P. V. Coveney. Lattice Boltzmann simulation of the flow of binary immiscible fluids with different viscosities using the Shan-Chen microscopic interaction model. *Philosophical Transactions of the Royal Society of London Series A: Mathematical Physical and Engineering Sciences*, 360(1792):547–558, 2002.

- [69] G. Christakos. Certain results on spatiotemporal random fields and their applications in environmental research. *Probabilistic and Stochastic*, 372: 287–322, 1992.
- [70] G. Christakos and D. T. Hristopulos. Stochastic space transformation techniques in subsurface hydrology—Part 2: Generalized spectral decompositions and plancherel representations. *Stochastic Hydrology and Hydraulics*, 8(2):117–155, 1994.
- [71] G. Christakos, D. T. Hristopulos, and C. T. Miller. Stochastic diagrammatic analysis of groundwater flow in heterogeneous porous media. *Water Resources Research*, 31(7):1687–1703, 1995.
- [72] G. Christakos, C. T. Miller, and D. Oliver. The development of stochastic space transformation and diagrammatic perturbation techniques in subsurface hydrology. *Stochastic Hydrology and Hydraulics*, 7(1):14–32, 1993.
- [73] G. Christakos, C. T. Miller, and D. Oliver. Cleopatra’s nose and the diagrammatic approach to flow modelling in random porous media. In *Geostatistics for the Next Century*, pages 341–358. Kluwer Academic Publishers, Amsterdam, The Netherlands, 1994.
- [74] V. Clausnitzer, J. W. Hopmans, and J. L. Starr. Parameter uncertainty analysis of common infiltration models. *Soil Science Society of America Journal*, 62(6):1477–1487, 1998.
- [75] B. Cockburn and C. N. Dawson. Some extensions of the local discontinuous Galerkin method for convection-diffusion equations in multidimensions. In J. R. Whiteman, editor, *The Proceedings of the Conference on the Mathematics of Finite Elements and Applications: MAFELAP X*, volume 39. Elsevier, 2000.
- [76] B. Cockburn and C. N. Dawson. Approximation of the velocity by coupling discontinuous Galerkin and mixed finite element methods for flow problems. *Computational Geosciences*, 6(3-4):502–522, 2002.
- [77] B. Cockburn, S. Hou, and C. W. Shu. TVB Runge-Kutta local projection discontinuous Galerkin finite element method for conservation laws IV: The multidimensional case. *Mathematical computation*, 54:545–581, 1990.
- [78] B. Cockburn, G. Kanschat, I. Perugia, and D. Schötzau. Superconvergence of the local discontinuous Galerkin method for elliptic problems on Cartesian grids. *SIAM Journal on Numerical Analysis*, 39(1):264–285, 2001.
- [79] B. Cockburn, G. Kanschat, and D. Schötzau. The local discontinuous Galerkin method for the osen equations. *Mathematics of Computation*, 73(246):569–593, 2004.
- [80] B. Cockburn, G. Kanschat, and D. Schötzau. The local discontinuous Galerkin method for linearized incompressible fluid flow: A review. *Computers & Fluids*, 34(4-5):491–506, 2005.

- [81] B. Cockburn, G. Kanschat, D. Schötzau, and C. Schwab. Local discontinuous Galerkin methods for the stokes system. *SIAM Journal on Numerical Analysis*, 40(1):319–343, 2002.
- [82] B. Cockburn, G. Kanschat, and D. Schötzau. The local discontinuous Galerkin method for the Oseen equations. *Mathematics of Computation*, 73:569–593, 2003.
- [83] B. Cockburn, E. Karniadakis, and C. W. Shu. The development of discontinuous Galerkin methods. In B. Cockburn, E. Karniadakis, and C. W. Shu, editors, *Lecture Notes in Computer Science and Engineering*, pages 3–50. Springer-Verlag, New York, 2000.
- [84] B. Cockburn, S. Lin, and C. W. Shu. TVB Runge-Kutta local projection discontinuous Galerkin finite element method for scalar conservation law III: One dimensional systems. *Journal of Computational Physics*, 84:93–113, 1989.
- [85] B. Cockburn and C.-W. Shu. TVB Runge-Kutta local projection discontinuous Galerkin finite element method for scalar conservation laws II: General framework. *Mathematical computation*, 52:411–435, 1989.
- [86] B. Cockburn and C. W. Shu. The Runge-Kutta local projection rho-1-Discontinuous-Galerkin finite-element method for scalar conservation-laws. *Rairo-Mathematical Modelling and Numerical Analysis-Modelisation Mathematique Et Analyse Numerique*, 25(3):337–361, 1991.
- [87] B. Cockburn and C. W. Shu. The local discontinuous Galerkin method for time-dependent convection-diffusion systems. *SIAM Journal on Numerical Analysis*, 35(6):2440–2463, 1998.
- [88] B. Cockburn and C.-W. Shu. Runge-Kutta discontinuous Galerkin methods for convection-dominated problems. *Journal of Scientific Computing*, 16: 173–261, 2001.
- [89] M. E. Coles, R. D. Hazlett, E. L. Muegge, K. W. Jones, B. Andrews, B. Dowd, P. Siddons, A. Peskin, P. Spanne, and W. Soll. Developments in synchrotron X-ray microtomography with applications to flow in porous media. *SPE Reservoir Evaluation and Engineering*, 1(4):288–296, 1998.
- [90] C. Cordes and K. Kinzelbach. Continuous groundwater velocity field and path lines in linear, bilinear, and trilinear finite elements. *Water Resources Research*, 28(11):2903–2911, 1992.
- [91] J. H. Cushman. *Dynamics of Fluids in Hierarchical Porous Media*. Academic Press, New York, 1990.
- [92] J. H. Cushman, B. X. Hu, and F. W. Deng. Nonlocal reactive transport with physical and chemical heterogeneity: Localization errors. *Water Resources Research*, 31(9):2219–2237, 1995.
- [93] G. Dagan. Comment on ‘A note on the recent natural gradient tracer test at the borden site’ by R. L. Naff, T.-C. Jim Yeh, and M. W. Kemblowski. *Water Resources Research*, 25(12):2521–2522, 1989.

- [94] H. K. Dahle and M. A. Celia. A dynamic network model for two-phase immiscible flow. *Computational Geosciences*, 3(1):1–22, 1999.
- [95] E. Dana and F. Skoczylas. Experimental study of two-phase flow in three sandstones. i. measuring relative permeabilities during two-phase steady-state experiments. *International Journal of Multiphase Flow*, 28(11):1719–1736, 2002.
- [96] C. N. Dawson. The $p^{k+1} s^k$ local discontinuous Galerkin method for elliptic equations. *SIAM Journal on Numerical Analysis*, 40(6):2151–2170, 2003.
- [97] C. N. Dawson. Coupling local discontinuous and continuous Galerkin methods for flow problems. *Advances in Water Resources*, 28(7):729–744, 2005.
- [98] C. N. Dawson, V. Aizinger, and B. Cockburn. Local discontinuous Galerkin methods for convection-dominated problems. In B. Cockburn, G. Karniadakis, and C. W. Shu, editors, *Discontinuous Galerkin Methods. Theory, Computation and Applications*, pages 309–314. Springer Verlag, 2000.
- [99] C. N. Dawson and J. Proft. Coupling of continuous and discontinuous Galerkin methods for transport problems. *Computer Methods in Applied Mechanics and Engineering*, 191(29-30):3213–3231, 2002.
- [100] C. N. Dawson, J. J. Westerink, J. C. Feyen, and D. Pothina. Continuous, discontinuous and coupled discontinuous-continuous galerkin finite element methods for the shallow water equations. *International Journal for Numerical Methods in Fluids*, 2006.
- [101] C. N. Dawson, M. F. Wheeler, and C. S. Woodward. A two-grid finite difference scheme for nonlinear parabolic equations. *SIAM Journal on Numerical Analysis*, 35(2):435–452, 1998.
- [102] V. de la Cruz and T. J. T. Spanos. Mobilization of oil ganglia. *American Institute of Chemical Engineers Journal*, 29(5):854–858, 1983.
- [103] K. S. Delibasis, G. K. Matsopoulos, N. A. Mouravliansky, and K. S. Nikita. A novel and efficient implementation of the marching cubes algorithm. *Computerized Medical Imaging and Graphics*, 25:343–352, 2001.
- [104] L. Demkowicz. Computing with hp -adaptive finite elements: I. one- and two-dimensional elliptic and maxwell problems. 2003.
- [105] L. Demkowicz, J. T. Oden, W. Rachowicz, and O. Hardy. Toward a universal h - p adaptive finite element strategy. part 1. Constrained approximation and data structure. *Computer Methods in Applied Mechanics and Engineering*, 77:79–112, 1989.
- [106] D. d’Humières, I. Ginzburg, M. Krafczyk, P. Lallemand, and L.-S. Luo. Multiple-relaxation-time lattice Boltzmann models in three dimensions. *Philosophical Transactions of the Royal Society of London Series A-Mathematical Physical and Engineering Sciences*, 360:437–451, 2002.

- [107] V. Dolejsi, M. Feistauer, and C. Schwab. On some aspects of the discontinuous Galerkin finite element method for conservation laws. *Mathematics and Computers in Simulation*, 61(3-6):333–346, 2003.
- [108] J. J. Douglas, B. L. Darlow, M. F. Wheeler, and R. P. Kendall. Self-adaptive finite element and finite difference methods for one-dimensional two-phase immiscible flow. *Computer Methods in Applied Mechanics and Engineering*, 47:119–130, 1984.
- [109] jr. Douglas, Jim and Todd F. Dupont. *Interior penalty procedures for elliptic and parabolic Galerkin methods*, volume 58 of *Lecture Notes in Physics*. Springer, Berli, 1976.
- [110] F. A. L. Dullien. *Porous Media: Fluid Transport and Pore Structure*. Academic Press, San Diego, CA, 1992.
- [111] F. A. L. Dullien and M. Dong. Experimental determination of the flow transport coefficients in the coupled equations of two-phase flow in porous media. *Transport in Porous Media*, 25(1):97–120, 1996.
- [112] L. J. Durlofsky. Accuracy of mixed and control volume finite element approximations to Darcy velocity and related quantities. *Water Resources Research*, 30(4):965–973, 1994.
- [113] R. Ehrlich. Viscous coupling in two-phase flow in porous media and its effect on relative permeabilities. *Transport in Porous Media*, 9:18–35, 1992.
- [114] R. Ehrlich. Viscous coupling in two-phase flow in porous media and its effect on relative permeabilities. *Transport in Porous Media*, 11(3):201–218, 1993.
- [115] K. Eriksson and C. Johnson. Error estimates and automatic time step control for nonlinear parabolic problems .1. *SIAM Journal on Numerical Analysis*, 24(1):12–23, 1987.
- [116] K. Eriksson and C. Johnson. Adaptive finite element methods for parabolic problems, 1. A linear model problem. *SIAM Journal on Numerical Analysis*, 28(1):43–77, 1991.
- [117] K. Eriksson and C. Johnson. Adaptive finite-element methods for parabolic problems .2. Optimal error-estimates in L^∞ - L^2 and L^∞ - L^∞ . *SIAM Journal on Numerical Analysis*, 32(3):706–740, 1995.
- [118] K. Eriksson and C. Johnson. Adaptive finite-element methods for parabolic problems .5. Long-time integration. *SIAM Journal on Numerical Analysis*, 32(6):1750–1763, 1995.
- [119] K. Eriksson and C. Johnson. Adaptive finite element methods for parabolic problems II: Optimal error estimates in l infinity l_2 and l infinity l infinity. *SIAM Journal on Numerical Analysis*, 32(3):706–740, 1995.
- [120] R. Eymard, M. Gutnic, and D. Hilhorst. The finite volume method for Richards equation. *Computational Geosciences*, 3:259–294, 1999.

- [121] S. Fagherazzi, D. J. Furbish, P. Rasetarinera, and M. Y. Hussaini. Application of the discontinuous spectral Galerkin method to groundwater flow. *Advances in Water Resources*, 27(2):129–140, 2004.
- [122] M. W. Farthing. *Accurate, Efficient Numerical Methods for Flow and Transport Phenomena in Porous Media*. PhD thesis, University of North Carolina at Chapel Hill, 2002.
- [123] M. W. Farthing, C. E. Kees, T. S. Coffey, C. T. Kelley, and C. T. Miller. Efficient steady-state solution techniques for variably saturated groundwater flow. In *EOS Transactions, American Geophysical Union Fall Meeting*, volume 83, pages H62B–0841, San Francisco, CA, 2002.
- [124] M. W. Farthing, C. E. Kees, T. S. Coffey, C. T. Kelley, and C. T. Miller. Efficient steady-state solution techniques for variably saturated groundwater flow. *Advances in Water Resources*, 26(8):833–849, 2003.
- [125] I. Fatt. The network model of porous media: I. Capillary pressure characteristics. *Transactions of the AIME*, 207:144–159, 1956.
- [126] G. Fennemore and J. X. Xin. Wetting fronts in one-dimensional periodically layered soils. *SIAM Journal on Applied Mathematics*, 58(2):387–427, 1998.
- [127] B. P. Flannery, H. W. Deckman, W. G. Roberg, and K. L. D’Amico. Three-dimensional X-ray microtomography. *Science*, 237:1464–1469, 1987.
- [128] P. A. Forsyth, Y. S. Wu, and K. Pruess. Robust numerical methods for saturated-unsaturated flow with dry initial conditions in heterogeneous media. *Advances in Water Resources*, 18:25–38, 1995.
- [129] U. Frisch, D. d’Humières, B. Hasslacher, P. Lallemand, Y. Pomeau, and J.-P. Rivet. Lattice gas hydrodynamics in two and three dimensions. *Complex Syst.*, 1:649–707, 1987.
- [130] U. Frisch, B. Hasslacher, and Y. Pomeau. Lattice-gas automata for the Navier-Stokes equation. *Physics Review Letters*, 56:1505–1507, 1986.
- [131] J. M. Gasto, J. Grifoll, and Y. Cohen. Estimation of internodal permeabilities for numerical simulation of unsaturated flows. *Water Resources Research*, 38(12), 2002.
- [132] L. W. Gelhar. Stochastic subsurface hydrology from theory to applications. *Water Resources Research*, 22(9):135S–145S, 1986.
- [133] L. W. Gelhar. *Stochastic Subsurface Hydrology*. Prentice Hall, Englewood Cliffs, NJ, 1993.
- [134] I. Ginzburg and D. d’Humières. Multireflection boundary conditions for lattice Boltzmann models. *Physical Review E*, 68:066614:1–30, 2003.
- [135] V. Girault, B. Rivière, and M. F. Wheeler. A discontinuous Galerkin method with non-overlapping domain decomposition for the Stokes and Navier-Stokes problems. Report 02-08, TICAM, Austin, 2002.

- [136] P. A. Goode. *Momentum transfer across fluid-fluid interfaces in porous media: A network model*. PhD thesis, Heriot-Watt University, UK, 1991.
- [137] P. A. Goode and T. S. Ramakrishnan. Momentum transfer across fluid-fluid interfaces in porous media: A network model. *AIChE Journal*, 39(7): 1124–1134, 1993.
- [138] G. Gottardi and M. Venutelli. One-dimensional moving-finite-element program for modeling solute transport in porous media. *Computers & Geosciences*, 21(5):663–685, 1995.
- [139] W. G. Gray. General conservation equations for multi-phase systems: 4. Constitutive theory including phase change. *Advances in Water Resources*, 6:130–140, 1983.
- [140] W. G. Gray. Thermodynamics and constitutive theory for multiphase porous-media flow considering internal geometric constraints. *Advances in Water Resources*, 22(5):521–547, 1999.
- [141] W. G. Gray. On the definition of derivatives of macroscale energy for the description of multiphase systems. *Advances in Water Resources*, 25(8–12): 1091–1104, 2002.
- [142] W. G. Gray. Elements of a systematic procedure for the derivation of macroscale conservation equations for multiphase flow in porous media. Lecture Note for "Multiphase Transport Phenomena" at University of North Carolina at Chapel Hill, 2003.
- [143] W. G. Gray and S. M. Hassanizadeh. Averaging theorems and averaged equations for transport of interface properties in multiphase systems. *International Journal of Multiphase Flow*, 15(1):81–95, 1989.
- [144] W. G. Gray and S. M. Hassanizadeh. Paradoxes and realities in unsaturated flow theory. *Water Resources Research*, 27(8):1847–1854, 1991.
- [145] W. G. Gray and S. M. Hassanizadeh. Macroscale continuum mechanics for multiphase porous-media flow including phases, interfaces, common lines and common points. *Advances in Water Resources*, 21(4):261–281, 1998.
- [146] W. G. Gray and P. C. Y. Lee. On the theorems for local volume averaging of multiphase systems. *International Journal of Multiphase Flow*, 3:333–340, 1977.
- [147] W. G. Gray and C. T. Miller. Thermodynamically constrained averaging theory approach for modeling flow and transport phenomena in porous medium systems: 1. Motivation and overview. *Advances in Water Resources*, 28(2):161–180, 2005.
- [148] D. W. Grunau, W. T. Lookman, S. Y. Chen, and A. S. Lapedes. Domain growth, wetting, and scaling in porous media. *Physical Review Letters*, 71(25):4198–4201, 1993.
- [149] A. K. Gunstensen and D. H. Rothman. Lattice-Boltzmann studies of immiscible two-phase flow through porous media. *Journal of Geophysical Research*, 98(B4):6431–6441, 1993.

- [150] D. W. Halt. *A compact higher order Euler solver for unstructured grids*. PhD thesis, Washington Univeristy, 1992.
- [151] P. A. Hamilton, T. L. Miller, and D. N. Myers. Water quality in the nation's streams and aquifers - overview of selected findings, 1991–2001. Technical report, USGS, 2004.
- [152] X. M. Hao, R. D. Zhang, and A. Kravchenko. A mass-conservative switching method for simulating saturated-unsaturated flow. *Journal of Hydrology*, 311(1-4):254–265, 2005.
- [153] R. Hartmann and P. Houston. Adaptive discontinuous Galerkin finite element methods for the compressible Euler equations. *Journal of Computational Physics*, 183(2):508–532, 2002.
- [154] S. M. Hassanizadeh and W. G. Gray. General conservation equations for multi-phase systems: 1. Averaging procedure. *Advances in Water Resources*, 2(3):131–144, 1979.
- [155] S. M. Hassanizadeh and W. G. Gray. General conservation equations for multi-phase systems: 2. Mass, momenta, energy, and entropy equations. *Advances in Water Resources*, 2(4):191–203, 1979.
- [156] S. M. Hassanizadeh and W. G. Gray. General conservation equations for multi-phase systems: 3. Constitutive theory for porous media flow. *Advances in Water Resources*, 3(1):25–40, 1980.
- [157] R. D. Hazlett. Simulation of capillary-dominated displacements in microtomographic images of reservoir rocks. *Transport in Porous Media*, 20(1-2): 21–35, 1995.
- [158] R. D. Hazlett, S. Y. Chen, and W. E. Soll. Wettability and rate effects on immiscible displacement: Lattice Boltzmann simulation in microtomographic images of reservoir. *Journal of Petroleum Science and Engineering*, 20(3–4):167–175, 1998.
- [159] R. J. Held and M. A. Celia. Modeling support of functional relationships between capillary pressure, saturation, interfacial areas and common lines. *Advances in Water Resources*, 24:325–343, 2001.
- [160] R. Helmig. *Multiphase Flow and Transport Processes in the Subsurface: A Contribution to the Modeling of Hydrosystems*. Springer-Verlag, Berlin, 1997.
- [161] F. J. Higuera and J. Jiménez. Boltzmann approach to lattice gas simulations. *Europhys. Lett.*, 9:663–668, 1989.
- [162] M. Hilpert, J. F. McBride, and C. T. Miller. Pore-scale modeling of hysteretic flow in porous media. In *Sixth SIAM Conference on Mathematical and Computational Issues in the Geosciences*, Boulder, CO, 2001.
- [163] J. R. Hooker, J. T. Batina, and M. H. Williams. Spatial and temporal adaptive procedure for the unsteady aerodynamic analysis of airfoils using unstructured meshes. Technical Memorandum 107635, Naational Aeronautics and Space Administration, Hampton, 1992.

- [164] J. Host-Madsen and K. H. Jensen. Laboratory and numerical investigations of immiscible multiphase flow in soil. *Journal of Hydrology*, 135(1-4):13–52, 1992.
- [165] S. L. Hou, X. W. Shan, Q. S. Zuo, G. D. Doolen, and W. E. Soll. Evaluation of two lattice Boltzmann models for multiphase flows. *Journal of Computational Physics*, 138(2):695–713, 1997.
- [166] P. Houston, D. Schotzau, and T. P. Wihler. An hp-adaptive mixed discontinuous galerkin fem for nearly incompressible linear elasticity. *Computer Methods in Applied Mechanics and Engineering*, 195(25-28):3224–3246, 2006.
- [167] P. Houston, C. Schwab, and E. Suli. Stabilized hp-finite element methods for first-order hyperbolic problems. *Siam Journal on Numerical Analysis*, 37(5):1618–1643, 2000.
- [168] P. Houston, C. Schwab, and E. Suli. Discontinuous hp-finite element methods for advection-diffusion-reaction problems. *Siam Journal on Numerical Analysis*, 39(6):2133–2163, 2002.
- [169] P. Houston, B. Senior, and E. Suli. Hp-discontinuous Galerkin finite element methods for hyperbolic problems: Error analysis and adaptivity. *International Journal for Numerical Methods in Fluids*, 40(1-2):153–169, 2002.
- [170] P. Houston and E. Suli. Hp-adaptive discontinuous Galerkin finite element methods for first-order hyperbolic problems. *SIAM Journal on Scientific Computing*, 23(4):1225–1251, 2001.
- [171] P. Houston and E. Suli. A note on the design of hp-adaptive finite element methods for elliptic partial differential equations. *Computational Methods in Applied Mechanical Engineering*, 194:229–243, 2005.
- [172] C. Q. Hu and C. W. Shu. A discontinuous galerkin finite element method for hamilton-jacobi equations. *Siam Journal on Scientific Computing*, 21(2):666–690, 1999.
- [173] X. Hu and J. H. Cushman. Non-equilibrium statistical mechanical derivation of a nonlocal Darcy’s law for unsaturated/saturated flow. *Stochastic Hydrology and Hydraulics*, 8(2):109, 1994.
- [174] J. F. Huang, J. Jia, and M. Minion. Accelerating the convergence of spectral deferred correction methods. *Journal of Computational Physics*, 214(2):633–656, 2006.
- [175] R. Huber and R. Helmig. Multiphase flow in heterogeneous porous media: A classical finite element method versus an implicit pressure-explicit saturation-based mixed finite element-finite volume approach. *International Journal for Numerical Methods in Fluids*, 29:899–920, 1999.
- [176] W. Hundsdorfer and J. G. Verwer. *Numerical solution of time-dependent advection-diffusion-reaction equations*. Springer, 2003.

- [177] S. S. Hutson, N. L. Barber, J. F. Kenny, K. S. Linsey, D. S. Lumia, and M. A. Maupin. Estimated use of water in the united states in 2002. *United States Geological Survey Circular*, 1(1268):46, 2004.
- [178] P. Indelman and B. Abramovich. Nonlocal properties of nonuniform averaged flows in heterogeneous media. *Water Resources Research*, 30(12):3385–3393, 1994.
- [179] Jacquotte. Grid optimization methods for quality improvement and adaptation. In J. F. Thompson, editor, *Handbook of Grid Generation*, pages 1–33. CRC, Boca Raton, 1998.
- [180] P. Jamet. Galerkin-type approximations which are discontinuous in time for parabolic equations in a variable domain. *SIAM Journal of Numerical Analysis*, 15(5):1–17, 1978.
- [181] S. H. Ju and K. J. S. Kung. Mass types, element orders and solution schemes for the Richards equation. *Computers & Geosciences*, 23(2):175–187, 1997.
- [182] M. Junk, A. Klar, and L.-S. Luo. Asymptotic analysis of the lattice Boltzmann equation. *in review, Journal of Computational Physics*, 2004.
- [183] F. Kalaydjian. A macroscopic description of multiphase flow in porous media involving spacetime evolution of fluid/fluid interface. *Transport in Porous Media*, 2:537–552, 1987.
- [184] F. Kalaydjian. Origin and quantification of coupling between relative permeabilities for two-phase flows in porous media. *Transport in Porous Media*, 5(3):215–229, 1990.
- [185] F. J. M. Kalaydjian. Dynamic capillary pressure curve for water/oil displacement in porous media: Theory vs. experiment. In *67th Annual Technical Conference and Exhibition of the Society of Petroleum Engineers*, pages 491–506, Washington, DC, 1992. Society of Petroleum Engineers.
- [186] D. Kandhai, A. Koponen, A. G. Hoekstra, M. Katajam, J. Timonen, and P. M. A. Slood. Lattice-Boltzmann hydrodynamics on parallel systems. *Computer Physics Communications*, 111:14–26, 1998.
- [187] Q. Kang, Zhang D., and S. Chen. Immiscible displacement in a channel: simulations of fingering in two dimensions. *Advances in Water Resources*, 27:13 – 22, 2004.
- [188] D. Kavetski, P. Binning, and S. W. Sloan. Adaptive time stepping and error control in a mass conservative numerical solution of the mixed form of Richards’ equation. *Advances in Water Resources*, 24(6):595–605, 2001.
- [189] D. Kavetski, P. Binning, and S. W. Sloan. Noniterative time stepping schemes with adaptive truncation error control for the solution of Richards’ equation. *Water Resources Research*, 38(10), 2002.

- [190] C. E. Kees and C. T. Miller. C++ implementations of numerical methods for solving differential-algebraic equations: Design and optimization considerations. *Association for Computing Machinery, Transactions on Mathematical Software*, 25(4):377–403, 1999.
- [191] C. E. Kees and C. T. Miller. Higher order time integration methods for two-phase flow. *Advances in Water Resources*, 25(2):159–177, 2002.
- [192] D. W. Kelly. The self-equilibration of residuals and complementary a posteriori error estimates in the finite element method. *International Journal for Numerical Methods in Engineering*, 20:1491–1506, 1984.
- [193] D. W. Kelly, J. Gago, O. C. Zienkiewicz, and I. Babuska. A-posteriori error analysis and adaptive processes in the finite-element method .1. error analysis. *International Journal for Numerical Methods in Engineering*, 19(11):1593–1619, 1983.
- [194] C. R. Killins, C. R. Nielson, and J. C. Calhoun. *Producers Mon.*, 18(2):30, 1953.
- [195] J. H. Kinney, T. M. Breunig, T. L. Starr, D. Haupt, M. C. Nichols, S. R. Stock, M. D. Butts, and R. A. Saroyan. X-ray tomographic study of chemical vapor infiltration processing of ceramic composites. *Science*, 260:789–792, 1993.
- [196] S. Kruyer. The penetration of mercury and capillary condensation in packed spheres. *Transactions of the Faraday Society*, 54:1758–1767, 1958.
- [197] P. Lallemand and L. S. Luo. Theory of the lattice Boltzmann method: Dispersion, dissipation, isotropy, Galilean invariance, and stability. *Physical Review E*, 61(6):6546–6562, 2000.
- [198] P. Lallemand and L. S. Luo. Lattice Boltzmann method for moving boundaries. *Journal of Computational Physics*, 184:406–421, 2003.
- [199] J. Lang, W. M. Cao, W. Z. Huang, and R. D. Russell. A two-dimensional moving finite element method with local refinement based on a posteriori error estimates. *Applied Numerical Mathematics*, 46(1):75–94, 2003.
- [200] K. Langaas and P. Papatzacos. Numerical investigations of the steady state relative permeability of a simplified porous medium. *Transport in Porous Media*, 45:241–266, 2001.
- [201] S. Larson and V. Thomee. *Partial differential equations with numerical methods*. Springer, 2003.
- [202] F. Lehmann and P. H. Ackerer. Comparison of iterative methods for improved solutions of the fluid flow equation in partially saturated porous media. *Transport in Porous Media*, 31(3):275–292, 1998.
- [203] M. C. Leverett. Steady flow of gas-oil-water mixtures through unconsolidated sands. *Trans. AIME*, pages 132 – 149, 1938.

- [204] D. Levy, C.-W. Shu, and J. Yan. Local discontinuous Galerkin methods for nonlinear dispersive equation. *Journal of Computational Physics*, 196(2):751–772, 2004.
- [205] H. Li, M. W. Farthing, C. N. Dawson, and C. T. Miller. Local discontinuous Galerkin approximations to Richards’ equation. *Advances in Water Resources*, In review, 2006.
- [206] Q. J. Liang and J. Lohrenz. Dynamic method of measuring coupling coefficients of transport equations of 2-phase flow in porous media. *Transport in Porous Media*, 15(1):71–79, 1994.
- [207] I. Lomtev and G. E. Karniadakis. A discontinuous galerkin method for the navier-stokes equations. *International Journal for Numerical Methods in Fluids*, 29(5):587–603, 1999.
- [208] W. E. Lorensen and H. E. Cline. Marching cubes: A high resolution 3D surface construction algorithm. *Computer Graphics*, 21(4):163–169, 1987.
- [209] M. I. Lowry and C. T. Miller. Pore-scale modeling of nonwetting-phase residual in porous media. *Water Resources Research*, 31(3):455–473, 1995.
- [210] R. S. Maier and L. R. Petzold. User’s guide to DASKMP and DASPKF90. Technical Report AHPCRC Preprint 93-034, Army High Performance Computing Research Center, Minneapolis, MN, 1993.
- [211] M. Majidi and G. Starke. Least-squares galerkin methods for parabolic problems ii: The fully discrete case and adaptive algorithms. *Siam Journal on Numerical Analysis*, 39(5):1648–1666, 2002.
- [212] R. S. Mansell, L. Ma, A. L. R., and S. A. Bloom. Adaptive grid refinement in numerical models for water flow and chemical transport in soils: a review. *Vadose Zone Journal*, 1:222–238, 2002.
- [213] N. Martys and H. Chen. Simulation of multicomponent fluids in complex three-dimensional geometries by the lattice Boltzmann method. *Physical Review E*, 53(1b):743–750, 1996.
- [214] R. P. Mayer and R. A. Stowe. Mercury porosimetry—Breakthrough pressure for penetration between packed spheres. *Journal of Colloid Science*, 20:893–911, 1965.
- [215] J. E. McClure, D. Adalsteinsson, C. Pan, W. G. Gray, and C. T. Miller. Approximation of interfacial properties in multiphase porous medium systems. *Advances in Water Resources*, In review, 2006.
- [216] G. McNamara and C. Zanetti. Use of the Boltzmann equation to simulate lattice-gas automata. *Physical Review Letters*, 61:2332–2335, 1988.
- [217] C. T. Miller, C. Abhishek, and M. W. Farthing. A spatially and temporally adaptive solution of Richards’ equation. *in press: Advances in Water Resources*, 2005.

- [218] C. T. Miller, C. Abhishek, A. B. Sallerson, J. F. Prins, and M. W. Farthing. A comparison of computational and algorithmic advances for solving Richards' equation. In C. T. Miller, M. W. Farthing, W. G. Gray, and G. F. Pinder, editors, *Proceedings of the XVth International Conference on Computational Methods in Water Resources*, pages 1131–1145, Chapel Hill, North Carolina, 2004. Elsevier.
- [219] C. T. Miller, G. Christakos, P. T. Imhoff, J. F. McBride, J. A. Pedit, and J. A. Trangenstein. Multiphase flow and transport modeling in heterogeneous porous media: Challenges and approaches. *Advances in Water Resources*, 21(2):77–120, 1998.
- [220] C. T. Miller, M. W. Farthing, C. E. Kees, and C. T. Kelley. Higher order locally conservative temporal integration methods for modeling multiphase flow in porous media. In S. M. Hassanizadeh, R. J. Schotting, W. G. Gray, and G. F. Pinder, editors, *XIV International Conference on Computational Methods in Water Resources*, volume Developments in Water Science, 47, Computational Methods in Water Resources, Volume 1, pages 249–256, Delft, The Netherlands, 2002. Elsevier.
- [221] C. T. Miller and W. G. Gray. Thermodynamically constrained averaging theory approach for modeling flow and transport phenomena in porous medium systems: 2. Foundation. *Advances in Water Resources*, 28(2):181–202, 2005.
- [222] C. T. Miller, G. A. Williams, and C. T. Kelley. Efficient and robust numerical modeling of variably saturated flow in layered and porous media. In *XII International Conference on Computational Methods in Water Resources*, Crete, Greece, 1998.
- [223] C. D. Montemagno and W. G. Gray. Photoluminescent volumetric imaging—A technique for the exploration of multiphase flow and transport in porous media. *Geophysical Research Letters*, 22(4):425–428, 1995.
- [224] P. K. Moore. Interpolation error-based a posteriori error estimation for hp-refinement using first and second derivative jumps. *Applied Numerical Mathematics*, 48(1):63–82, 2004.
- [225] R. Mosé, P. Siegel, and P. Ackerer. Application of the mixed hybrid finite element approximation in a groundwater flow model: Luxury or necessity? *Water Resources Research*, 30(11):3001–3012, 1994.
- [226] Y. Mualem. A new model for predicting the hydraulic conductivity of unsaturated porous media. *Water Resources Research*, 12(3):513–522, 1976.
- [227] C. R. Nastase and D. J. Mavriplis. High-order discontinuous galerkin methods using an hp-multigrid approach. *Journal of Computational Physics*, 213(1):330–357, 2006.
- [228] R. R. Nourgaliev, T. N. Dinh, T. G. Theofanous, and D. Joseph. The lattice Boltzmann equation method: Theoretical interpretation, numerics and implications. *International Journal of Multiphase Flow*, 29:119–169, 2003.

- [229] J. T. Oden. Progress in adaptive methods in computational fluid dynamics. In J. E. Flaherty, P. J. Paslow, M. S. Shephard, and J. D. Vasilakis, editors, *Adaptive Methods for Partial Differential Equations*, pages 206–252. Society for Industrial and Applied Mathematics, Philadelphia, 1989.
- [230] J. T. Oden, I. Babuska, and C. E. Baumann. A discontinuous hp finite element method for diffusion problems. *Journal of Computational Physics*, 146(2):491–519, 1998.
- [231] J. T. Oden, L. Demkowicz, W. Rachowicz, and O. Hardy. Toward a universal h - p adaptive finite element strategy. part 2. A posteriori error estimation. *Computer Methods in Applied Mechanics and Engineering*, 77: 113–180, 1989.
- [232] J. T. Oden and A. Patra. A parallel adaptive strategy for hp finite-element computations. *Computer Methods in Applied Mechanics and Engineering*, 121(1-4):449–470, 1995.
- [233] T. J. Oden and C. Baumann. A conservative DGM for convection-diffusion and Navier-Stokes problems. In B. Cockburn, G. E. Karniadakis, and C. Shu, editors, *Discontinuous Galerkin Methods*, 2000.
- [234] H. S. Oh, J. K. Lim, and S. Y. Han. An rh-method for efficient adaptive finite element analysis. *Communications in Numerical Methods in Engineering*, 14(6):549–558, 1998.
- [235] J. F. Olson and D. H. Rothman. Two-fluid flow in sedimentary rock: Simulation, transport and complexity. *Journal of Fluid Mechanics*, 341: 341–370, 1997.
- [236] L. Onsager. Reciprocal relations in irreversible processes: I. *Physical Review*, 37:405–426, 1931.
- [237] L. Onsager. Reciprocal relations in irreversible processes: II. *Physical Review*, 38:2265–2279, 1931.
- [238] P. E. Oren and W. V. Pinczewski. Fluid distribution and pore-scale displacement mechanisms in drainage dominated three-phase flow. *Transport in Porous Media*, 20(1-2):105–133, 1995.
- [239] C. Pan. *Use of Pore-scale Modeling to Understand Flow and Transport in Porous Media*. PhD thesis, University of North Carolina at Chapel Hill, 2003.
- [240] C. Pan, M. Hilpert, and C. T. Miller. Pore-scale modeling of saturated permeabilities in random sphere packings. *Physical Review E*, 64(6):article number 066702, 2001.
- [241] C. Pan, M. Hilpert, and C. T. Miller. Lattice-Boltzmann simulation of two-phase flow in porous media. *Water Resources Research*, 40(1), 2004.
- [242] C. Pan, L.-S. Luo, and C. T. Miller. An evaluation of lattice Boltzmann schemes for porous medium flow simulation. *Computers & Fluids*, In Press, Corrected Proof available on line, 2006.

- [243] C. Pan, J. F. Prins, and C. T. Miller. A high-performance lattice Boltzmann implementation to model flow in porous media. *Computer Physics Communication*, 158(2):89–105, 2004.
- [244] L. Pan, A. W. Warrick, and P. J. Wierenga. Finite element methods for modeling water flow in variably saturated porous media: Numerical oscillation and mass-distributed schemes. *Water Resources Research*, 32(6):1883–1889, 1996.
- [245] C. Paniconi and M. Putti. A comparison of Picard and Newton iteration in the numerical solution of multidimensional variably saturated flow problems. *Water Resources Research*, 30(12):3357–3374, 1994.
- [246] D. W. Pepper and D. B. Carrington. Application of h-adaptation for environmental fluid flow and species transport. *International Journal for Numerical Methods in Fluids*, 31(1):275–283, 1999.
- [247] W. Rachowicz, J. T. Oden, and L. Demkowicz. Toward a universal h - p adaptive finite element strategy. part 3. Design of h - p meshes. *Computer Methods in Applied Mechanics and Engineering*, 77:181–212, 1989.
- [248] C. D. Rail. *Groundwater contamination*, volume 1. Lancaster, Pa. : Technomic Pub, 2000.
- [249] M. Rashidi, L. Peurrung, A. F. B. Tompson, and T. J. Kulp. Experimental analysis of pore-scale flow and transport in porous media. *Advances in Water Resources*, 19(3):163–180, 1996.
- [250] K. Rathfelder and L. M. Abriola. Mass conservative numerical solutions of the head-based Richards equation. *Water Resources Research*, 30(9):2579–2586, 1994.
- [251] W. H. Reed and T. R. Hill. Triangle meshes methods for the neutron transport equations. Technical report, Los Alamos Scientific Laboratory, 1973.
- [252] P. C. Reeves and M. A. Celia. A functional relationship between capillary pressure, saturation, and interfacial area as revealed by a pore-scale network model. *Water Resources Research*, 32(8):2345–2358, 1996.
- [253] J. F. Remacle, J. E. Flaherty, and M. S. Shephard. An adaptive discontinuous galerkin technique with an orthogonal basis applied to compressible flow problems. *Siam Review*, 45(1):53–72, 2003.
- [254] B. Rivière, M. F. Wheeler, and K. Banas. Part II. discontinuous Galerkin method applied to a single phase flow in porous media. *Computational Geosciences*, 4(4):337–349, 2000.
- [255] B. Rivière, M. F. Wheeler, and V. Girault. Improved energy estimates for interior penalty, constrained and discontinuous Galerkin methods for elliptic problems. part I. *Computational Geosciences*, 3(3-4):337–360, 1999.
- [256] S. Rose. Analysis of temporal environmental isotopic variation in ground water of the georgia piedmont. *Ground Water*, 33(4):644–652, 1995.

- [257] W. Rose. Measuring transport coefficients necessary for the description of coupled two-phase flow of immiscible fluids in porous media. *Transport in Porous Media*, 3(2):163–171, 1988.
- [258] W. Rose. Coupling coefficients for two-phase flow in pore spaces of simple geometry. *Transport in Porous Media*, 5(1):97–102, 1990.
- [259] W. Rose. Myths about later-day extensions of Darcy’s law. *Journal of Petroleum Science and Engineering*, 26:187–198, 2000.
- [260] C. Ross. Gold mining affects ground water. *Ground Water Monitoring Review*, 12(4):100–102, 1992.
- [261] P. J. Ross. Efficient numerical methods for infiltration using Richards’ equation. *Water Resources Research*, 26(2):279–290, 1990.
- [262] T. Rosswall, R. G. Woodmansee, and P. G. Risser. *Scales and Global Change : Spatial and Temporal Variability in Biospheric and Geospheric Processes*. Chichester, 1988.
- [263] D. H. Rothman and J. M. Keller. Immiscible cellular-automaton fluids. *Journal of Statistical Physics*, 52(3/4):1119–1127, 1988.
- [264] T. F. Russell, D. W. Dean, T. H. Illangasekare, R. Mapa, and J. Garcia. Upscaling of dispersivity in modeling of solute transport: Mathematical theory and laboratory experiments. *Mathematical Modelling of Flow Through Porous Media*, pages 301 – 317, 1995.
- [265] K. P. Saripalli, H. Kim, P. S. C. Rao, and M. D. Annable. Measurement of specific fluid-fluid interfacial areas of immiscible fluids in porous media. *Environmental Science & Technology*, 31(3):932–936, 1997.
- [266] C. E. Schaefer, D. A. Dicarolo, and M. J. Blunt. Determination of water-oil interfacial area during 3-phase gravity drainage in porous media. *Journal of Colloid and Interface Science*, 221(2):308–312, 2000.
- [267] D. Schötzau and C. Schwab. Time discretization of parabolic problems by the Hp-version of the discontinuous Galerkin finite element method. *SIAM Journal on Numerical Analysis*, 38(3):837–875, 2000.
- [268] X. Shan and H. Chen. Lattice Boltzmann model for simulating flows with multiple phases and components. *Physical Review E*, 47:1815–1819, 1993.
- [269] X. Shan and H. Chen. Simulation of nonideal gases and liquid-gas phase transitions by the lattice Boltzmann equation. *Physical Review E*, 49(4): 2941–2948, 1994.
- [270] X. Shan and G. Doolen. Multicomponent lattice-Boltzmann model with interparticle interaction. *Journal of Statistical Physics*, 81(1/2):379–393, 1995.
- [271] X. Shan and G. Doolen. Diffusion in a multi-component lattice Boltzmann equation model. *Physical Review E*, 54(4):3614–3620, 1996.

- [272] S. J. Sherwin, R. M. Kirby, J. Peiro, R. L. Taylor, and O. C. Zienkiewicz. On 2d elliptic discontinuous galerkin methods. *International Journal for Numerical Methods in Engineering*, 65(5):752–784, 2006.
- [273] C. W. Shu. High-order finite difference and finite volume WENO schemes and discontinuous Galerkin methods for CFD. *International Journal of Computational Fluid Dynamics*, 17(2):107–118, 2003.
- [274] C. W. Shu and J. Yan. Local discontinuous Galerkin for partial differential equations with higher order derivatives. *Journal of Scientific Computation*, 17:27–47, 2002.
- [275] J. Simunek, T. Vogel, and M. T. Genuchten. The SWMS_2D code for simulating water flow and solute transport in two-dimensional variably saturated media. Technical report, U. S. Salinity Laboratory, Agricultural Research Service, U. S. Department of Agriculture, 1994.
- [276] M. Slodicka. A robust and efficient linearization scheme for doubly non-linear and degenerate parabolic problems arising in flow in porous media. *SIAM Journal on Scientific Computing*, 23(5):1593–1614, 2002.
- [277] P. Spanne, J. F. Thovert, C. J. Jacquin, W. B. Lindquist, K. W. Jones, and P. M. Adler. Synchrotron computed microtomography of porous-media - Topology and transports. *Physical Review Letters*, 73(14):2001–2004, 1994.
- [278] G. Starke. Gauss-Newton multilevel methods for least-squares finite element computations of variably saturated subsurface flow. *Computing*, 64(4):323–338, 2000.
- [279] S. Succi. Lattice boltzmann equation: Failure or success? *Physica A*, 240(1-2):221–228, 1997.
- [280] L. Tang and J. D. Baeder. Uniformly accurate finite difference schemes for p-refinement. *Siam Journal on Scientific Computing*, 20(3):1115–1131, 1999.
- [281] M. D. Tocci, C. T. Kelley, and C. T. Miller. Accurate and economical solution of the pressure-head form of Richards’ equation by the method of lines. *Advances in Water Resources*, 20(1):1–14, 1997.
- [282] M. D. Tocci, C. T. Kelley, C. T. Miller, and C. E. Kees. Inexact Newton methods and the method of lines for solving Richards’ equation in two space dimensions. *Computational Geosciences*, 2(4):291–309, 1999.
- [283] M. S. Valavanides, G. N. Constantinides, and A. C. Payatakes. Mechanistic model of steady-state two-phase flow in porous media based on ganglion dynamics. *Transport in Porous Media*, 30:267–299, 1998.
- [284] M. S. Valavanides and A. C. Payatakes. True-to-mechanism model of steady-state two-phase flow in porous media, using decomposition into prototype flows. *Advances in Water Resources*, 24(3–4):385–407, 2001.

- [285] J. C. van Dam and R. A. Feddes. Numerical simulation of infiltration, evaporation and shallow groundwater levels with the Richards equation. *Journal of hydrology*, 233:72–85, 2000.
- [286] M. T. van Genuchten. A closed-form equation for predicting the hydraulic conductivity of unsaturated soils. *Soil Science Society of America Journal*, 44:892–898, 1980.
- [287] P. E. van Keken, D. A. Yuen, and L. R. Petzold. Time-integration techniques for the combined Stokes and heat equations using an implicit high order solver for differential-algebraic equations (DASL) with applications to mantle convection. Technical Report AHPARC Preprint 94-019, Army High Performance Computing Research Center, Minneapolis, MN, 1994.
- [288] G. G. Venutelli. A control-volume finite-element model for two-dimensional overland flow. *Advances in Water Resources*, 16:277–284, 1993.
- [289] Mary Fanett Wheeler. An elliptic collocation-finite element method with interior penalties. *SIAM J. Numer. Anal.*, 15(1):152–161, 1978.
- [290] S. Whitaker. Flow in porous media I: A theoretical derivation of Darcy’s law. *Transport in Porous Media*, 1:3–25, 1986.
- [291] T. P. Wihler, P. Frauenfelder, and C. Schwab. Exponential convergence of the hp-dgfm for diffusion problems. *Computers & Mathematics with Applications*, 46(1):183–205, 2003.
- [292] G. A. Williams and C. T. Miller. An evaluation of temporally adaptive transformation approaches for solving Richards’ equation. *Advances in Water Resources*, 22(8):831–840, 1999.
- [293] G. A. Williams, C. T. Miller, and C. T. Kelley. Transformation approaches for simulating flow in variably saturated porous media. *Water Resources Research*, 36(4):923–934, 2000.
- [294] C. S. Woodward and C. N. Dawson. Analysis of expanded mixed finite element methods for a nonlinear parabolic equation modeling flow into variably saturated porous media. *SIAM Journal on Numerical Analysis*, 37(3):701–724, 2000.
- [295] Y. S. Wu and P. A. Forsyth. On the selection of primary variables in numerical formulation for modeling multiphase flow in porous media. *Journal of Contaminant Hydrology*, 48(3-4):277–304, 2001.
- [296] R. D. Wyckoff and H. G. Botset. The flow of gas-liquid mixtures through unconsolidated sands. *Physics*, 7:325–345, 1936.
- [297] J. Yan and C. W. Shu. A local discontinuous Galerkin method for KdV type equations. *SIAM Journal of Numerical Analysis*, 40(2):769–791, 2002.
- [298] V. M. Yevjevich. *Stochastic processes in hydrology*. Fort Collins, Colo., Water Resources Publications, 1972.

- [299] A. Younes, R. Mos, P. Ackerer, and G. Chavent. A new formulation of the mixed finite element method for solving elliptic and parabolic PDEs with triangular elements. *Journal of Computational Physics*, 148–167, 1999.
- [300] A. Younes, R. Mose, P. Ackerer, and G. Chavent. A new formulation of the mixed finite element method for solving elliptic and parabolic pde with triangular elements. *Journal of Computational Physics*, 149(1):148–167, 1999.
- [301] J. Zaidel and D. Russo. Estimation of finite difference interblock conductivities for simulation of infiltration into initially dry soils. *Water Resources Research*, 28(9):2285–2295, 1992.
- [302] C. Zarcone and R. Lenormand. Experimental determination of viscous coupling during 2-phase flow in porous media. *Comptes Rendus de L Academie des Sciences serie II*, 318(11):1429–1435, 1994.
- [303] D. Zhang. *Stochastic Methods for Flow in Porous Media: Coping with Uncertainties*. Academic Press, San Diego, CA, 2002.
- [304] D. Zhang, R. Zhang, S. Chen, and W. E. Soll. Pore scale study of flow in porous media: Scale dependency, REV, and statistical REV. *Geophysical Research Letters*, 27(8):1195–1198, 2000.
- [305] C. Zhou, R. Shu, and M. S. Kankanhalli. Selectively meshed surface representation. *Computer Graphics*, 19(6):793–804, 1995.
- [306] O. C. Zienkiewicz and J. Z. Zhu. The superconvergent patch recovery and *A Posteriori* error estimates. part 1: The recovery technique. *International Journal for Numerical Methods in Engineering*, 33:1331–1364, 1992.